1998

Solid-State Sensors, Actuators, and Microsystems Workshop

Late News Poster Session Supplemental Digest

Table of Contents

Author Index

Copyright

www.hh1998.org

Sponsored by the
Transducer Research Foundation, Inc.
Additional support provided:
Defense Advanced Research Projects Agency

Hilton Head Workshop
June 8 - 11, 1998 • Hilton Head, South Carolina
Editors: Luc Bousse & Antonio J. Ricco

TRF Catalog Number: 98TRF-0001
Library of Congress Control Number: 98-60214
ISBN Number: 0-9640024-2-6
ISSN 1539-2058 (Print) • ISSN: 1539-204X (Electronic)
DOI 10.31438/trf.hh1998A.0

1998

Solid-State Sensors, Actuators, and Microsystems Workshop

Hilton Head Island, South Carolina • June 8 - 11, 1998

All opinions expressed in this digest are those of the authors and are not binding on Transducer Research Foundation, Inc.
Copies of available volumes of this digest may be obtained from the Transducer Research Foundation, Inc., c/o 307 Laurel Street, San Diego, California 92101-1630 USA (+1-619-232-9499)

Copyright and Reprint Permission: Abstracting is permitted with credit to the source. Libraries are permitted to photocopy beyond the limit of U.S. copyright law for private use of patrons those articles in this volume that carry a code at the bottom of the first page, provided the per-copy fee indicated in the code is paid through Copyright Clearance Center, 222 Rosewood Drive, Danvers, MA 01923. For other copying, reprint or republication permission, contact Transducer Research Foundation, Inc., c/o 307 Laurel Street, San Diego, California 92101-1630 USA, info@transducer-research-foundation.org. All rights reserved. Copyright ©1998 by the Transducer Research Foundation, Inc. Personal use of this material is permitted. However, permission to reprint/republish this material for advertising or promotional purposes of for creating new collective works for resale or redistribution to servers or lists, or to reuse any copyrighted component of this work in other works must be obtained from the Transducer Research Foundation, Inc.

TRF Catalog Number: 98TRF-0001
Library of Congress Control Number: 98-60214
ISBN Number: 0-9640024-2-6
ISSN 1539-2058 (Print) • ISSN: 1539-204X (Electronic)
DOI 10.31438/trf.hh1998A.0

This product contains Adobe Acrobat software. Copying this product's instructions and/or designs for use on future CD-ROMs or digital products is prohibited without written permission from The Printing House and Adobe Systems Incorporated. The Printing House or its suppliers are not liable for any direct, indirect, special, incidental, or consequential damages to your hardware or other software arising out of the use—or the inability to use—the material on this CD-ROM. This includes, but is not limited to, the loss of data or loss of profit. Adobe, Acrobat and the Acrobat logo are trademarks of Adobe Systems Incorporated or its subsidiaries and may be registered in certain jurisdictions.

If you have questions regarding the installation, please contact:

The Printing House
Phone: +1-608-873-4500
Hours: Monday through Friday, 8 am - 5 pm CST
E-mail: graphics@printinghouseinc.com

Solid-State Sensor and Actuator Workshop
June 8 – 11, 1998
Crowne Plaza Resort
Hilton Head Island, South Carolina

Late News Poster Session

Table of Contents

The Cobble Algorithm: Macromodels for MEMS via Stepwise, Sequential, Design of Experiments for Patched Functional Approximation 1
S.B. Crary[†‡] and K.N. Phan[‡]; [‡]University of Michigan, [†]Technical University of Denmark

A Meshless Technique for Analysis of Microelectromechanical Switches 3
N.R. Aluru; University of Illinois at Urbana-Champaign

Design, Finite Element Analysis, and Experimental Performance Evaluation of a Thermally-Actuated Beam Used to Achieve Large In-Plane Mechanical Deflections 5
P.B. Allen, J.T. Howard, E.S. Kolesar, and J.M. Wilken; Texas Christian University

Electrostatic Domino Actuators 7
G.D. Su, L. Fan, and M.C. Wu; UCLA

Scanning Blazed-Gratings for High-Resolution Spectroscopy 9
J.T. Nee, K.Y. Lau, and R.S. Muller; UC Berkeley

Data Transmission Through a 16 Channel Micro-Opto-Mechanical Wavelength Add/Drop Switch 11
J.E. Ford, C. Chung, J.A. Walker, V. Aksyuk, D.J. Bishop, and C. Doerr; Lucent Technologies

Demonstration of a Gain Flattened Optical Amplifier with a Micromechanical Equalizer Element 13
J.A. Walker, J.E. Ford, and K.W. Goossen; Lucent Technologies

Thick Single Crystal Si Lateral Resonant Devices Integrated with a Conventional Circuit Process 15
J.A. Weigold, A.-C. Wong, C.T.-C. Nguyen, S.W. Pang; University of Michigan

Measurements of the Effect of Specimen Size on Young's Modulus and Tensile Strength of Polysilicon 17
W.N. Sharpe, K. Turner, and R.L. Edwards; Johns Hopkins University

A Robust Capacitive Pressure Sensor Array 19
J.-B. Lee, S.-P. Chang, and M.G. Allen; Georgia Tech

Self-Aligned Polysilicon MEMS - Reduced Mask Count Surface Micromachining 21
J.M. Noworolski and S.R. Sanders; UC Berkeley

Table of Contents (continued)

Sled Carriers and Molded Three-Surface Tips for Atomic Force Microscope Cantilevers 23
R.P. Ried, H.J. Mamin, and D. Rugar; IBM

Fabrication of a Micro Turbine/Bearing Rig 25
C.-C. Lin, R. Ghodssi, A.A. Ayon, D.-Z. Chen, and M.A. Schmidt; MIT

A Silicon Micromachined Gate Valve 27
M. Walters, V. Dhuler, R. Mahadevan, A. Cowen, R. Wood, E. Hill and I. Kao[†];
MCNC, [†]SUNY Stoneybrook

Velocimetry for MEMS 29
J.G. Santiago, C.D. Meinhart[†], S.T. Wereley[†], D.J. Beebe, and R.J. Adrian;
University of Illinois at Urbana-Champaign; [†]UC Santa Barbara

Numerical Investigation of Pumping Effects in FPW-Devices 31
N.T. Nguyen, R.W. Doering, and R.M. White; UC Berkeley

Electrochemical Pressure Generation 33
T. Stanczyk, B. Ilic, P.J. Hesketh, and J. Boyd; University of Illinois at Chicago

Excess Analyte Dispersion Generated by Turns on Microchips 35
C.T. Culbertson, S.C. Jacobson, and J.M. Ramsey; Oak Ridge National Laboratory

A Microfluidic Device Combining Dielectrophoresis and Field Flow Fractionation for Particle and Cell Discrimination 37
P. Gascoyne, X. Wang, J. Vykoukal, H. Ackler[†], S. Swierkowski[†], and P. Krulevitch[†];
University of Texas, [†]Lawrence Livermore National Laboratory

A Forest Without Trees: Development of High-Surface-Area Materials for Enhanced-Sensitivity SAW Array 39
W.G. Yelton, A.J. Ricco, and A.W. Staton; Sandia National Laboratories

Molecular Recognition in Gas Sensing: Results from Acoustic Wave and In-Situ FTIR Measurements 41
A. Hierleman, A.J. Ricco, K. Bodenhöfer[†], and W. Göpel[†];
Sandia National Laboratories, [†]Universität Tübingen

Solvent Sensor Arrays for Binary Mixtures Using Polymer-Based Chemiresistors 43
S.V. Patel, M.W. Jenkins, R.C. Hughes, W.G. Yelton, A.J. Ricco,
and S.A. Casalnuovo; Sandia National Laboratories

Author Index 45

TECHNICAL PAPERS

Solid-State Sensors, Actuators, and Microsystems
Workshop

1998
Hilton Head Island, South Carolina
June 8 - 11

THE COBBLE™ ALGORITHM: MACROMODELS FOR MEMS VIA STEPWISE, SEQUENTIAL, DESIGN OF EXPERIMENTS FOR PATCHED FUNCTIONAL APPROXIMATION

Selden B. Crary[1,2] and Khanhtran N. Phan[1]

[1]Center for Integrated Sensors and Circuits
The University of Michigan
Ann Arbor, Michigan 48109-2122, USA

[2]Center for Microinstruments
Technical University of Denmark
DK-2800, Lyngby/Copenhagen

ABSTRACT

We outline a new algorithm, COBBLE, for the generation of macromodels based on computer simulations. The algorithm uses a stepwise, sequential, design-of-experiments approach to functional approximation and is applied to a MEMS example.

INTRODUCTION

Modeling and simulation of microsensor devices and systems is essential for the understanding of device and system behavior. In previous work we have focused on applying established techniques from the branches of mathematics known as design of experiments and functional approximation. We have also extended these techniques by the development of new algorithms and software implementations, such as the I-OPT™ program that finds optimal designs for functional prediction under the I-optimality criterion, a method that is the design-of-experiments counterpart to least-squares curve fitting [1]. These methods have been successfully demonstrated on problems arising in the development of MEMS, namely the efficient calibration of sensors and the efficient functional approximation of sensor responses via finite-element analysis [2].

Recently, we have been extending these capabilities by developing a new algorithm that provides a highly efficient, sequential, design-of-computer-experiments approach to the construction of a patched functional approximation to device or system performance, as expressed by the results of simulations.

In this paper we demonstrate the application of this algorithm (named COBBLE for Computer-Based Blind Empiricism), for finding parsimonious functional approximations of a pressure-sensor device performance over a wide range of parameter values. The objective is to obviate the need for additional FEA runs by using the parsimonious models as surrogates for the FEA runs, thus dramatically reducing computational time and expense for additional runs that may be used for optimization, confirmation, or design of new devices. The challenge is to find a means to significantly reduce the number of FEA runs required for a given level of accuracy of the functional approximation, i.e., to avoid as much as possible the "curse of dimensionality" that arises in multi-parameter settings.

COBBLE

Here is how COBBLE works. As initial inputs to COBBLE, the user provides the following:

- A list of parameters and parameter ranges. The parameters may be discrete or continuous geometrical values (e.g., boss diameter, diaphragm diameter, thicknesses, etc.), material properties (anisotropic moduli of elasticity, Poisson's ratios, etc.), or constraints as may be required by the simulator (e.g., whether or not the bending degrees of freedom of the boss are to be constrained in order to reduce computational complexity).
- A nominal run of the device or system (e.g., the output of an FEA run of the pressure sensor at nominal values of the parameters).
- A (possibly null) set of inequality constraints for the parameters (e.g., that the diameter of the boss of the diaphragm pressure sensor be less than the diameter of the diaphragm itself).
- (Optional) An educated guess as to the extent of the parameter space near the nominal starting point, over which a given degree of approximation can be expected to be valid, called a "trust region" (e.g., a second-degree approximation can be expected to be valid over a ±10% range of diaphragm diameters.)
- The required accuracy for the functional approximation (e.g., ±3% of the maximum absolute value of an output variable, such as the displacement normal to the undeflected diaphragm).

We use the Buckingham Π Theorem [3] to minimize the number of dimensionless independent variables. Then a form of optimal factor screening [4] is used to identify irrelevant variables using a small number of simulations. Also, the COBBLE algorithm extends advanced design-of-experiments methods used in physical experiments to the realm of computer experiments, with its different distributional assumptions about error, by drawing upon the work of Sacks, Schiller, and Welch [5]. In addition, the new COBBLE algorithm includes a supervisory sub-routine that uses Bayesian methods to manage the tradeoffs among accuracy, time, computational cost, and choice of method of model generation.

A key ingredient of COBBLE is its use of many fewer simulations than are required in factorial designed experiments. In k dimensions, factorial methods use $(m+1)^k$ points in an mth-degree functional approximation over a patch. Even if shared points among adjacent patches are considered, there are 2^k points per patch for full second-degree models. This exponential dependence on dimension can be mitigated somewhat by the use of fractional-factorial methods, but the computational explosion remains severe. By contrast, the optimal-design approach recognizes that there are only $(k+m)!/k!m!$ required points for a full m^{th}-degree approximation in each patch. With shared points this can be reduced to $(k+1)^2/2^k$ points per patch for models of second degree. For example, in three dimensions the factorial method requires eight simulations per second-degree patch, whereas the optimal-design approach requires only two. The factor of reduction of required runs grows with dimension, as shown in Figure 1. For example, with k=10 dimensions, the full-factorial approach requires 1024 simulations per second-degree patch, whereas the optimal-design approach requires only ~0.12 simulations per patch, a reduction of nearly 10^4 in the required number of simulations.

After the algorithm suggests a new set of simulation runs, the user then makes additional runs, which may include none, some, or all of those proposed by the algorithm, as well as any additional runs that the user chooses that were not suggested by

0-9640024-2-6/hh1998/$20©1998TRF
DOI 10.31438/trf.hh1998A.1

COBBLE. When these runs are completed, the user reports the parameter values and respective simulation results back to COBBLE, and the iteration cycles until COBBLE has found a patched functional approximation over the entire parameter space of interest, within the required accuracy.

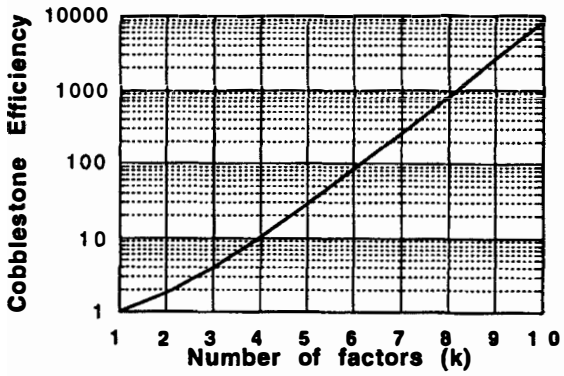

Figure 1. The cobblestone efficiency grows exponentially with the number of factors.

EXAMPLE

The pressure sensor provides an example of the operation of COBBLE. First we created a parameterized FEA input file for ANSYS, our FEA software. We then sought a parsimonious model of the displacement of the diaphragm normal to the plane of the undeflected diaphragm, using the boss diameter (nominal value R=300μm) and the diaphragm diameter (nominal value r=500μm) as independent variables. The ranges of these two variables and the constraints are shown in Fig. 2, below.

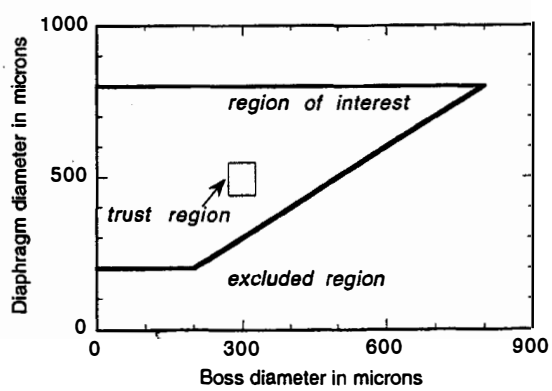

Figure 2. The space of constrained independent variables, showing the initial "trust region."

After a few iterations through COBBLE and the FEA code, 16 additional runs had been made using the FEA code, and we found that a third-degree bivariate polynomial model met the accuracy requirement of ±3% over a rectangular region somewhat larger than, and oriented by 30% ccw with respect to the original trust region. Figure 2 shows the original trust region and the locations of the 17 FEA runs, in a plot where the independent variables have been reduced to the range $[-1,1]^2$. The curved lines denote statistically determined estimates of the boundaries of the region where the accuracy requirement is met. The rectangle oriented at approximately 30% with respect to the original trust region is the rectangle with the maximal area that bounds a region meeting the accuracy requirements.

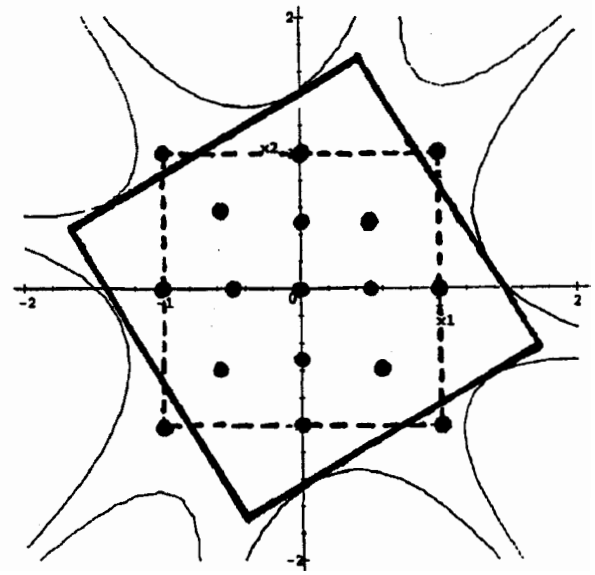

Figure 3. Initial trust region (dashed square) is shown again, this time in reduced variables, along with the (asymmetrical) locations of the inputs for the first 17 FEA runs. Also shown are curved boundaries for the region over which the ±3% accuracy requirement is estimated to hold, and the oriented rectangle with maximal area inscribed in that region.

After the nominal plus 16 additional FEA runs used for the functional approximation in the initial region, we have a statistical basis for the best local rectangular tiling, including orientation. COBBLE can then proceed to suggest input values for additional FEA runs. With sharing of points between rectangular regions, only 5 additional FEA runs per new region are necessary.

REFERENCES

1. S. B. Crary and J. R. Clark, "I-OPT User's Manual," URL: http://www-personal.engin.umich.edu/~crary/iopt, (rev. 1996); this site also contains the I-OPT software.

2. Y. B. Gianchandani and S. B. Crary, "Parametric Modeling of a Microaccelerometer Using I-Optimal Design of Experiments for Finite-Element Analysis," *to be published in IEEE J. of MEMS* (1998). An earlier version of this paper appeared in the *Proceedings of the Symposium on Mechanics in Micro-Electro-Mechanical Systems (MEMS),* held as part of the International Mechanical Engineering Congress and Exposition (Winter Annual Meeting of the ASME), Atlanta, GA, 11/17-22/96, ASME (1996).

3. P. W. Bridgman, Dimensional Analysis, 2nd Ed., Yale Univ. Press, New Haven, (1931).

4. M. Sobel, "Optimal Group Testing," *Tech. Report No. 72,* Dept. of Statistics, Stanford Univ., (1964).

5. J. Sacks, S. B. Schiller, and W. J.Welch, "Design of Computer Experiments," *Technometrics, 31,* 41 (1989).

ACKNOWLEDGMENTS

This work was funded, in part, by a contract from Tanner Research. We thank A. V. Chavan for assistance with the FEA and Joseph I. Seeger for bringing Ref. 4 to our attention.

A MESHLESS TECHNIQUE FOR ANALYSIS OF MICROELECTROMECHANICAL SWITCHES

N. R. Aluru
3221 Beckman Institute, MC-251, 405 N. Mathews Avenue
University of Illinois at Urbana-Champaign, Urbana, IL 61801
e-mail: aluru@uiuc.edu, http://www-ceg.ceg.uiuc.edu/~aluru/

ABSTRACT

Many existing computer-aided design systems for MEMS require the generation of a three-dimensional mesh for computational analysis of the microdevice. Mesh generation requirements for microdevices are very complicated because of the presence of mixed-energy domains and the different numerical techniques implemented for each energy domain. For example, volume meshes are employed for finite-element analysis of structural deformation and surface meshes are employed for boundary-element analysis of electrostatic forces on the structure. This paper describes a meshless technique, using which the analysis of a complicated microdevice can be performed by sprinkling points instead of generating a mesh.

INTRODUCTION

The present approach to modeling and design of microelectromechanical systems involves the generation of a geometric model for the complicated three-dimensional microdevice, the generation of a mesh for the geometric model, a self-consistent mesh-based numerical analysis of the mixed-energy domains present in the microdevice, and postprocessing steps such as visualization. An example of a CAD system based on such an approach was presented by Senturia et. al. in [1]. The time consuming steps in such an approach are the generation of a mesh for a microdevice and the self-consistent analysis of the mixed-energy domains. Fast techniques for self-consistent analysis of mixed-energy domains is currently being pursued as a research area (see e.g. [2]).

In this paper we describe a new technique to develop computer-aided design systems for MEMS based on meshless techniques. In meshless techniques, the generation of a mesh for the complicated three-dimensional microdevice is eliminated, and instead points are sprinkled for the geometrical representation of the microdevice. Self-consistent analysis of the mixed-energy domains is then performed by new point-based techniques instead of the usual mesh-based techniques. The implementation of a meshless technique for analysis of microelectromechanical switches is described in this paper.

MESHLESS TECHNIQUE

The meshless technique presented in this work is based on the smooth particle hydrodynamics (SPH) technique presented by Monaghan in [3]. In SPH, an approximation $u^a(x)$ to $u(x)$ in a domain Ω is generated by a kernel approximation i.e.

$$u^a(x) = \int_\Omega w(x-s)u(s)ds \tag{1}$$

where $w(x-s)$ is the kernel or a weighting function. The kernel function is non-zero ($w(x-s) > 0$) in a subdomain Ω_I of Ω and zero outside the subdomain Ω_I. For a method to be convergent, it has to be stable and consistent. The numerical solutions with a non-convergent method can exhibit amplitude and phase errors and a deterioration in the accuracy of the solution. It can be shown that the discrete form of SPH is not consistent. The consistency of SPH can be established by correcting the approximation introduced in equation (1). The concept of a correction function was introduced by Liu in [4] and a corrected kernel approximation of equation (1) is written as

$$u^a(x) = \int_\Omega \overline{w}_a(x; x-s)u(s)ds \tag{2}$$

where $\overline{w}_a(x; x-s)$ is the corrected kernel function which is given by

$$\overline{w}_a(x; x-s) = C(x, x-s)w_a(x-s) \tag{3}$$

$$w_a(x-s) = \frac{1}{a}w(\frac{x-s}{a}) \tag{4}$$

where $C(x, x-s)$ is called the correction function and a is the dilation parameter of the kernel function $w_a(x-s)$. The discrete approximation to equation (2) can be written as

$$u^a(x) = \sum_{I=1}^{N_p} \overline{w}_a(x; x-x_I)u(x_I)\Delta V_I \tag{5}$$

where the domain Ω is now represented by N_p points instead of a usual mesh and ΔV_I is a measure of the domain surrounding node I. Eventhough the summation in equation (5) is written over all the points in the domain, it is effectively over the points x_I where $\overline{w}_a(x; x-x_I) > 0$. Equation (5) can be rewritten as

$$u^a(x) = \sum_{I=1}^{N_p} N_I(x)u_I \tag{6}$$

$$N_I(x) = C(x; x-x_I)w_a(x-x_I)\Delta V_I \tag{7}$$

where $u_I = u(x_I)$ is the value of the function u at node x_I, and N_I is defined as the shape function for node I, and it is not the usual shape function referred to in the context of finite-element methods.

MESHLESS ANALYSIS OF SWITCHES

The static and dynamic behavior of many microelectromechanical switches can be characterized by studying the deformation of fixed-fixed and cantilever beams subjected to electrostatic voltages. The governing equation of a beam subjected to electrostatic forces is given by

$$\rho\frac{\partial^2 u}{\partial t^2} + EI\frac{\partial^4 u}{\partial x^4} = -\frac{w\epsilon_0 V^2}{2g^2}(1 + 0.65\frac{g}{w}) \tag{8}$$

where ρ is the mass density per unit length of the beam, u is the displacement of the beam, E is the Young's modulus of the material, I is the moment of inertia, w is the width of the beam, ϵ_0 is the permittivity of free space, V is the applied voltage and g is the gap between the beam and ground electrode. Equation (8) is nonlinear because the gap, g, depends on the displacement of the beam i.e. $g = g(u)$.

A meshless approach to the solution of equation (8) comprises of the following steps:

1. A weak form to the strong form given in equation (8) is constructed by multiplying equation (8) by an arbitrary test function (say v) and integrating by parts.

0-9640024-2-6/hh1998/$20©1998TRF
DOI 10.31438/trf.hh1998A.2

2. The unknowns u and v are approximated by the shape functions constructed through a corrected kernel approach described above. From equation (6), it follows that

$$u = \sum_{I=1}^{N_p} N_I(x) u_I \qquad v = \sum_{I=1}^{N_p} N_I(x) v_I \tag{9}$$

3. When the approximations to u and v are substituted in the weak form, a nonlinear system of equations is obtained, which is solved by a Newton-Raphson method.

In the current implementation, cubic splines are employed as the kernel functions and the correction function is obtained by writing consistency conditions to exactly represent second-degree polynomials.

RESULTS

The static and dynamic behavior of a fixed-fixed beam is modeled using the meshless technique. The beam considered here is $80\mu m$ long, $10\mu m$ wide, and $0.5\mu m$ thick. The initial gap between the beam and the bottom electrode is $0.7\mu m$. A Young's modulus of 169 GPa and a mass density of 2231 kg/m^3 are employed in the simulations shown here. The same device has been simulated in the work presented in [5] and the static and dynamic pull-in values obtained through experiments and simulations were reported.

Figure 1 shows the deflection of the beam as a function of a series of applied voltages. As the potential difference between the beam and the ground electrode increases, the gap between the beam and the bottom electrode decreases. At a certain voltage, the beam becomes unstable and collapses onto the ground electrode. For the beam under consideration, this voltage is computed to be 15.08 volts. The pull-in value reported in [5] is 15.17 volts and the error is less than 1%.

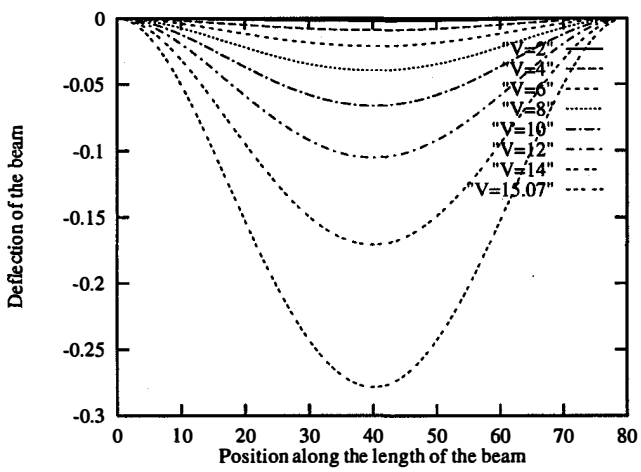

Figure 1. Deflection of a fixed-fixed beam for applied voltages

We have also done dynamic studies using the meshless technique. In particular, energy conserving dynamic algorithms have been implemented to study the fixed-fixed beam. The peak deflection of the beam, which is at the center of the beam, for an applied bias of 10 V is shown in Figure 2. The response in Figure 2 is obtained using a time step of 5×10^{-4} μs and the simulation is performed for a total of 5μs. The dynamic pull-in voltage is measured to be 13.7 volts and it matches with the value reported in [5]. The pull-in behavior of the beam for a bias of 13.7 volts is shown in Figure 3. Note that the dynamic pull-in voltage is smaller than the quasi-static pull-in voltage by about 9%.

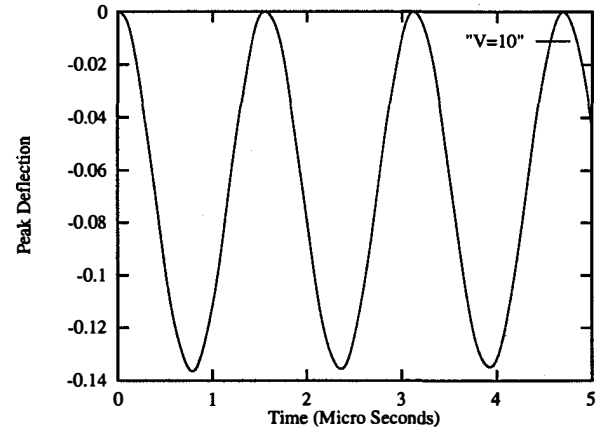

Figure 2. Peak deflection (deflection at the center) of a fixed-fixed beam as a function of time

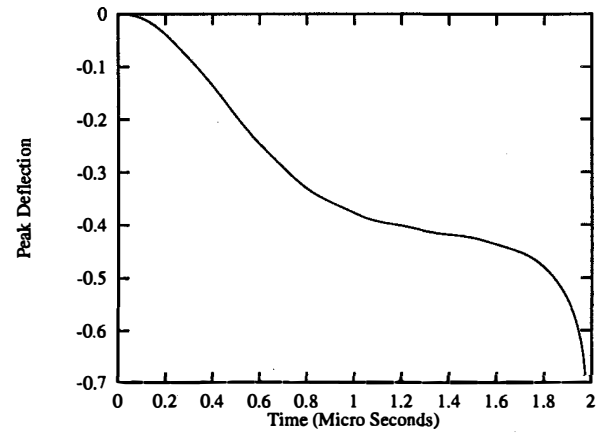

Figure 3. Pullin behavior of the beam for a voltage of 13.7 volts

CONCLUSIONS

A meshless technique for analysis of microelectromechanical devices is presented here for the first time. The approach is shown to be accurate by comparing pull-in voltages with previously reported data. Finally, it is anticipated that with meshless techniques in place, radically simpler and easy to use computer-aided design tools will be available for MEMS designers.

REFERENCES

[1] S. D. Senturia, R. M. Harris, B. P. Johnson, S. Kim, K. Nabors, M. A. Shulman, and J. K. White, "A computer-aided design system for Microelectromechanical Systems," *J. Microelectromechanical Systems*, Vol. 1, pp. 3-13, 1992.

[2] S. D. Senturia, N. R. Aluru and J. K. White, "Simulating the behavior of MEMS devices: Computational methods and needs," *IEEE Computational Science and Engineering*, Vol. 4, No. 1, pp. 30-43, Jan-Mar, 1997.

[3] J. J. Monaghan, "Why particle methods work," *SIAM J. Sci. Stat. Comput.*, Vol. 3, No. 4, pp. 422-433, 1982.

[4] W. K. Liu, Y. Chen, C. T. Chang and T. Belytschko, "Advances in multiple scale kernel particle methods," *Computational Mechanics*, Vol. 18, pp. 73-111, 1996.

[5] G. K. Ananthasuresh, R. K. Gupta and S. D. Senturia, "An approach to macromodeling of MEMS for nonlinear dynamic simulation," *Microelectromechanical Systems (MEMS), ASME Dynamic Systems and Control (DSC) series*, New York, vol. 59, pp. 401-407, 1996.

DESIGN, FINITE ELEMENT ANALYSIS, AND EXPERIMENTAL PERFORMANCE EVALUATION OF A THERMALLY-ACTUATED BEAM USED TO ACHIEVE LARGE IN-PLANE MECHANICAL DEFLECTIONS

Peter B. Allen, Jeffery T. Howard, Edward S. Kolesar and Josh M. Wilken
Texas Christian University, Department of Engineering, TCU Box 298640, Fort Worth, TX 76129

ABSTRACT

Numerous electrically-driven microactuators have been investigated for positioning individual elements in microelectromechanical systems (MEMS). The most common modes of actuation are electrostatic, magnetostatic, piezoelectric and thermal expansion [1]. Unfortunately, the forces produced by electrostatic and magnetostatic actuators tend to be small, and to achieve large displacements, it is necessary to either apply a large voltage or operate the devices in a resonant mode. On the other hand, piezoelectric and thermal expansion actuators can be configured to produce large forces and large displacements. Unfortunately, piezoelectric materials are not routinely supported in the fabrication processes offered by commercial MEMS foundries. Consequently, these limitations have focused attention on thermally-actuated devices for generating the large forces and displacements frequently required to position and assemble complex MEMS [2].

INTRODUCTION

This research focuses on the design, finite element analysis and experimental performance evaluation of a MEMS thermally-actuated beam [3,4]. The motivation is to present a unified description of the behavior of the thermal beam so that it can be adapted to a variety of applications in the microsensor and microactuator arenas. As depicted in Figure 1, a MEMS polysilicon thermally-actuated beam uses resistive (Joule) heating to generate thermal expansion and movement. When current is passed through the actuator from anchor-to-anchor, the larger current density in the "hot" arm causes it to heat and expand more than the "cold" arm. Since both arms are joined at their free (released) ends, the actuator tip is forced to move in an arc-like pattern. Removing the current from the device allows it to return to its equilibrium state. To be a useful MEMS device, a thermally-actuated beam will need to produce incremental in-plane mechanical beam tip deflections that span 0-10 μm while generating force magnitudes greater than 10 μN.

EXPERIMENTAL

The thermally-actuated beam design (Figure 1) was accomplished with the L-Edit® software program, and they were fabricated using the Multi-User Microelectromechanical Systems (MEMS) Process® (MUMPs) foundry at the Microelectronics Center of North Carolina (MCNC) [5].

The finite element analysis was accomplished with the IntelliCAD® computer program. As depicted in Figure 2, this CAD software incorporates an MCNC fabrication process description file that verifies and generates a 3-D solid model of a given MEMS design. As illustrated in Figures 3 and 4, the thermal and electromechanical finite element analyses yielded beam tip deflections and forces consistent with experimental observations. When the "hot" arm's temperature is 600°C (Joule heating), the resulting beam tip deflection is 4.55 μm.For a beam tip force of 14μN, the displacement was calculated to be 12.9 μm. The resonant frequency, without damping, was calculated to be 74.7 kHz.

The MEMS thermally-actuated beam performance was also experimentally characterized. As depicted in Figure 5, when the drive voltage was varied between 0 and 8 VDC, tip deflections spanning 0-8 μm were observed. The corresponding tip forces spanned 0-12 μN. The resonant frequency in ambient air was 68.7 kHz. A measure of the reliability of the thermal beam was established to be greater than 2 million cycles, when continuously operated with a 60 Hz, 4-volt amplitude square wave.

REFERENCES

[1] L. Ristic (ed.), Sensor Technology and Devices, Artech House, Norwood, MA, 1994.

[2] C.S. Pan and W. Hsu, "An electro-thermally and laterally driven polysilicon microactuator," J. Micromech. Microeng., Vol. 7, pp. 7-13, 1997.

[3] H. Guckel, et al., "Thermo-magnetic metal flexure actuators," Solid-State Sen. Act. Workshop, Hilton Head Island, SC, June 22-25, 1992, pp. 73-5.

[4] J.H. Comtois and V.M. Bright, "Surface micromachined polysilicon thermal actuator arrays and applications," Solid-State Sen. Act. Workshop, Hilton Head Island, SC, June 2-6, 1996, pp. 174-6.

[5] P.B. Allen, J.M. Wilken and E.S. Kolesar, "Design, Fabrication and Performance Evaluation of Several Electrical and Mechanical Silicon Microstructures Realized using the Emerging Technology of Microelectromechanical Systems (MEMS)," Proc. 1997 Conf. ASEE, Houston, TX, March 23-25, 1997, pp. 43-8.

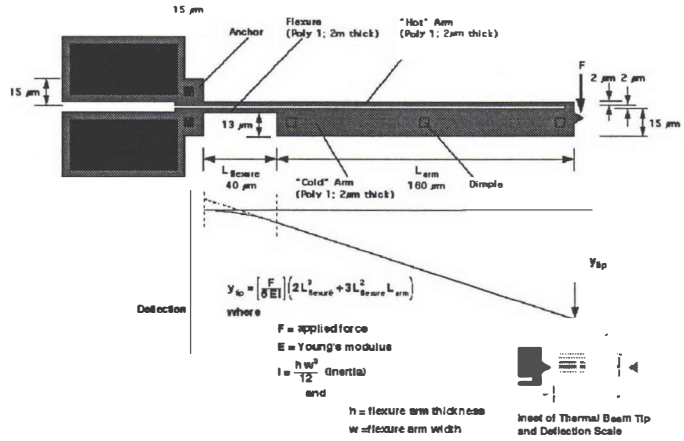

Figure 1. Polysilicon thermal beam design and analytical relationship relating tip deflection and tip force. The 2.0 μm thick polysilicon thermally-deflectable beam is suspended above a silicon nitride dielectric layer via the sacrificial glass etch process. The three dimples (square-shaped features) positioned along the length of the wide segment of the beam act as near-frictionless bearings. The inset depicts a

magnified view of the thermal beam's tip ("pointer" feature) and scale used to measure deflection.

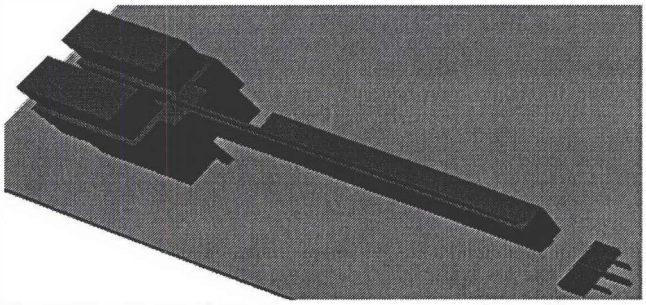

Figure 2. Three-dimensional solid model of the thermal beam generated by the IntelliCAD program.

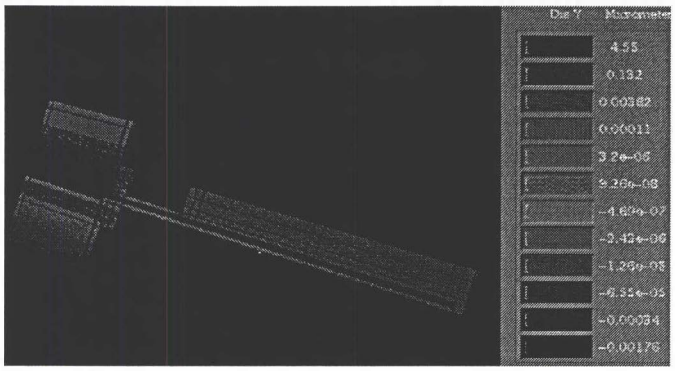

Figure 3. Thermomechanical performance of the thermal beam. With a 6 VDC drive signal, the characteristic temperature of the narrow thermal beam was 600°C. The average tip temperature of the wide arm was 150°C. The resulting in-plane deflection of the beam's tip is 4.55 μm.

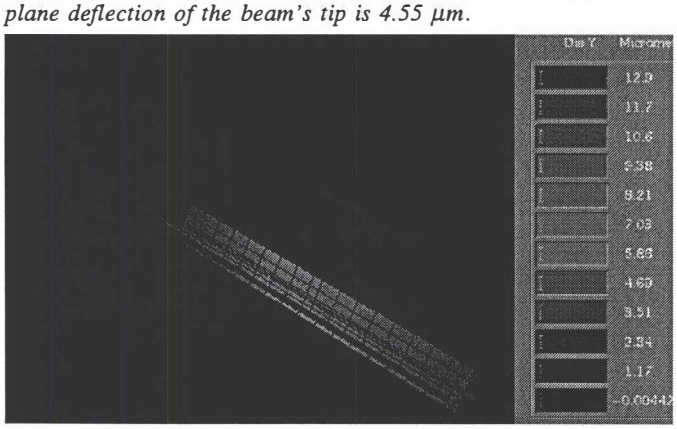

(a)

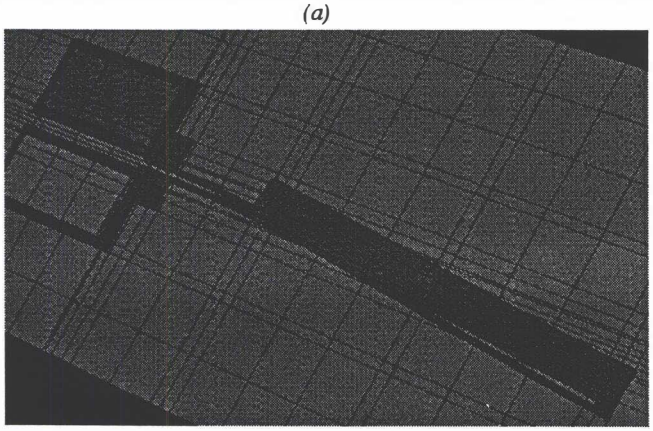

(b)

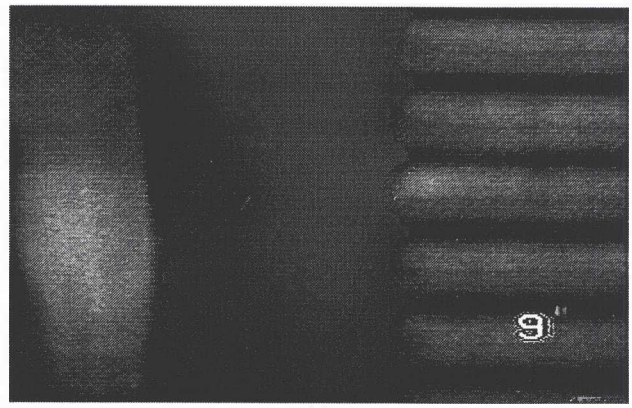

(c)

Figure 4. Electromechanical performance of the thermal beam. (a) Upon the application of a 14 μN force to the tip of the beam (Figure 1), the resulting in-plane tip deflection was predicted to be 12.9 μm (the analytical model in Figure 1 predicts a deflection of nearly 10 μm.. (b) The resonant frequency of the thermal beam was calculated to be 74.7 kHz (note that the beam now deflects about its equilibrium in-plane position). (c) The experimentally observed resonant frequency was 68.7 kHz.

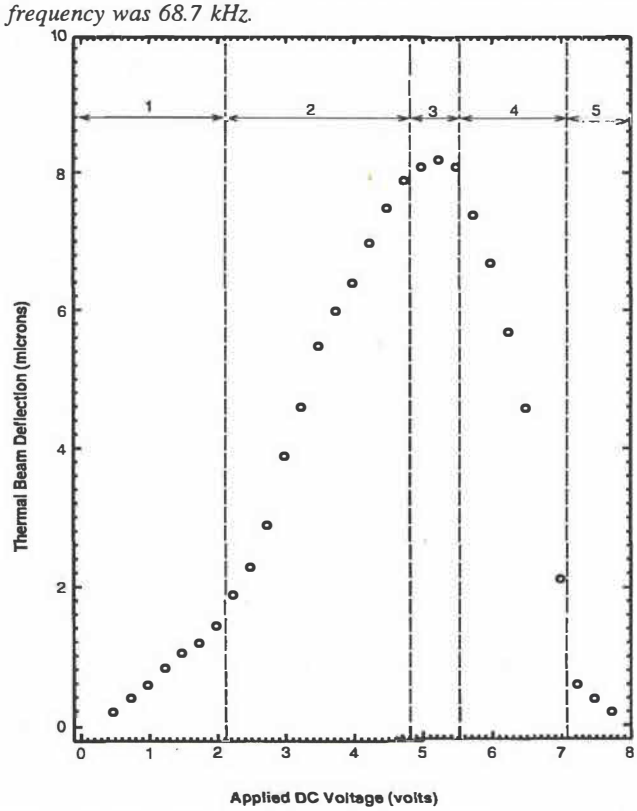

Figure 5. Plot of the thermal beam's applied direct current (DC) voltage versus tip deflection experimental data segmented into 5 behavioral regions. (Each data symbol represents the arithmetic average of three values). Key: Region 1: Elastic mode (buckling of the narrow width beam element not observed). Region 2: Elastic and reversible buckling mode. Region 3: Transition from the elastic to plastic mode (irreversible buckling). Region 4: Plastic mode (pronounced buckling; return to the zero-deflection position no longer occurs). Region 5: Transition to thermal beam failure.

ELECTROSTATIC DOMINO ACTUATORS

Guo D. Su, Li Fan, and Ming C.Wu
Electrical Engineering Department, UCLA
66-147D Engineering IV, 405 Hilgard Avenue, Los Angeles, CA 90095-1594
TEL: 310-825-6859, EMAIL: wu@icsl.ucla.edu

ABSTRACT

A surface-micromachined electrostatic domino actuator (EDA) has been proposed and successfully demonstrated. The EDA consists of N stages of gap-closing actuators with linearly increasing gap spacing. Large displacement and large force are achieved by the domino effect created by successive pull-in of the gap-closing actuator array. Experimentally, a displacement of 24 μm (bi-directional) at 35 V bias has been successfully achieved by a four-stage EDA.

INTRODUCTION

Electrostatic force is very attractive for micro-electro-mechanical systems (MEMS) because of good scaling properties to small dimensions, high energy densities, and ease of fabrication [1]. Gap-closing and comb drive actuators are two most popular electrostatic actuators [2,3]. The gap-closing actuators have large force, however, their displacement is limited because the electrostatic force is inversely proportional to the square of the gap separation. Recently, several approaches have been proposed to increase the displacement of gap-closing actuators [4-6]. 28 μm displacement (at 160V) and 6.3 μN (at 200V) force has been achieved in [4], however, it is difficult to realize the structure by surface-micromachining technology. The curved electrode actuator can achieve large displacement at low voltage (30 μm at 40V) [6], however, the force is small at zero displacement and the flexible beam could deform when driving a load.

In this paper, we propose a new large-force, large-displacement actuator, called electrostatic domino actuator (EDA). The domino actuator consists of an array of serially connected gap-closing actuators with linearly increasing gap sizes. The first gap-closing actuator with small gap separation determines the force of the EDA, while the last gap-closing actuator with large gap spacing determines the displacement of EDA. Experimentally, a four-stage EDA has been successfully demonstrated using the polysilicon surface-micromachining technology. Bi-directional displacement of 24 μm has been achieved at a bias voltage of 35 V. The force at zero displacement is 8.5 μN. The experimental results agree very well with theory. The EDA can be easily integrated with other microstructures using the well-established surface micromachining fabrication technology.

PRINCIPLE

The EDA comprises an array of gap-closing actuators with linearly increasing gap separation. In contrast to the distributed electrostatic microactuators in Ref. [4], the stators (fixed electrode) of all gap-closing actuators are anchored to the substrate. The movers (movable electrode) are suspended from the substrate by springs and connected to each other by "pull-only" joints. The gap spacing increases linearly from the first to the final stages: it is Δ for the first stage, 2Δ for the second stage, and nΔ for the n-th stage. The scanning electron micrographs (SEM) of the EDA and the "pull-only" joints are shown in Fig. 1(a) and (b), respectively.

The EDA has two electrodes, one connects to all stators, and the other connects to all movers. The working principle of EDA is illustrated in Fig. 2. Initially, when a voltage applied, the first stage is most effective because of the small gap separation. When the first stage mover is pulled in, all the following stages are moved by the same displacement, Δ, as illustrated in Fig. 2(b). Then the resulting gap spacing of second stage becomes 2Δ − Δ = Δ, which is the same as that of the original spacing of the first stage. As the second gap-closing actuator pulls in, the remaining stages are moved by another Δ, as shown in Fig. 2(c). The same process is repeated at every stage until the last stage was pulled in. The displacement of the last stage is N×Δ, where N is the number of stages.

The EDA has the following unique features:

1) Large displacement (determined by the last gap-closing actuator),
2) Large force at zero displacement (determined by the first gap-closing actuator),
3) Low voltage operation,
4) The EDA can be easily integrated with other surface-micromachined structures.

FABRICATION

The domino actuator is fabricated by the surface micromachining technology at MEMS Technology Application Center at North Carolina (MCNC). The two polysilicon layers are stacked to increase aspect ratio for larger force. The current design has four stages in both directions, as shown in Fig. 1(a). The electrodes are 3.5 μm high and 1 mm long. The gap spacing is 3, 6, 9, and 12 μm, respectively. The force of the domino actuators can be further increased by employing high-aspect-ratio electrodes such as deep reactive ion etched (DRIE) structures.

RESULTS AND DISCUSSION

The domino actuator has been successfully demonstrated. The displacement of EDA as a function of applied voltage has been measured. To determine pull-in voltage, the driving voltage was slowly increased until the mover at each stage hit the polysilicon stopper. The results are shown in Fig. 3. A maximum displacement of 24 μm (12μm in each direction) has been achieved at a bias voltage of 35V. The experimental results agree very well with theoretical calculations, as shown in Fig. 3.

Compared with conventional gap closing actuators, the EDA offers larger displacement, larger force, and lower operating voltage. This can be understood by examining the expression for electrostatic force for parallel plates:

$$F = -\frac{1}{2}\frac{\varepsilon_0 t l V^2}{d^2}.$$

where ε_0 is the dielectric constant, t and l are the thickness and length of the electrodes, respectively, d is the gap spacing, and V is the driving voltage. The electrostatic force is inversely proportional to the square of the gap spacing. The EDA effectively reduces the gap spacing by a factor of N, where N is the number of stages. The resulting electrostatic force is N^2 larger than that of the conventional gap closing actuator with the same total displacement. The displacement-vs-voltage characteristics of the conventional gap-closing actuator with the same displacement is

0-9640024-2-6/hh1998/$20©1998TRF
DOI 10.31438/trf.hh1998A.4

also shown in Fig. 3. The pull-in voltage has been reduced from 46 V to 35 V. Figure 4 shows the calculated forces of the EDA and the gap-closing actuators at 100 V bias. The electrostatic force at zero displacement has been increased from 2.3 to 8.5 μN.

The performance of the EDA can be further optimized. The current design employs the same springs for all stages. By properly choosing the individual spring constants, the EDA performance can be further optimized. Our theoretical calculation shows that a bi-directional displacement of 50 μm can be achieved at 32 V bias with an optimized a 5-stage EDA.

CONCLUSION

A novel electrostatic domino actuator (EDA) has been proposed and successfully demonstrated to increase the displacement of gap-closing actuators. The domino effect in the EDA increases its total displacement while maintaining the force. Experimentally, a displacement of 24μm has been achieved at a applied voltage of 35V. The force at zero displacement is calculated to be 8.5 μN. The actuator performance can be further optimized.

REFERENCES

1. W. Trimmer and R. Jebens, " Actuators for Micro Robots ", Proceedings. 1989 IEEE International Conference on Robotics and Automation (Cat. No.89CH2750-8), 1989, pp. 1547-1552
2. W. Trimmer and R. Jebens, " Design Consideration for a Practical Electrostatic Micro-motor ", Sensors and Actuators, vol. 11, 1987, pp. 189-206
3. W. C. Tang, C. H. Nguyen, and R. T. Howe, " Laterally Driven Polysilicon Resonant Microstructures ", Sensors and Actuators, vol. 20, 1990, pp. 25-32
4. K. Minami, S. Kawamura, and M. Esashi, " Fabrication of Distributed Electrostatic Micro Actuator ", Journal of Microelectromechanical Systems, vol. 2, no. 3, September 1993, pp. 121-127
5. S. Bobbio, M. Kellam, B. Dudley, S. Johnson, S. Jones, J. Jacobson, F. Tranjan, and T Dubois, " Integrated Force Arrays ", in Proc. IEEEE Micro Electro Mechanical Syst. Workshop, 1993, pp. 149-154
6. R. Legtenberg, E. Berenschot, M. Elwenspoek, and J. Fluitman, " Electrostatic Curved Electrode Actuators ", Proceedings. IEEE Micro Electro Mechanical Systems 1995, pp. 37-42

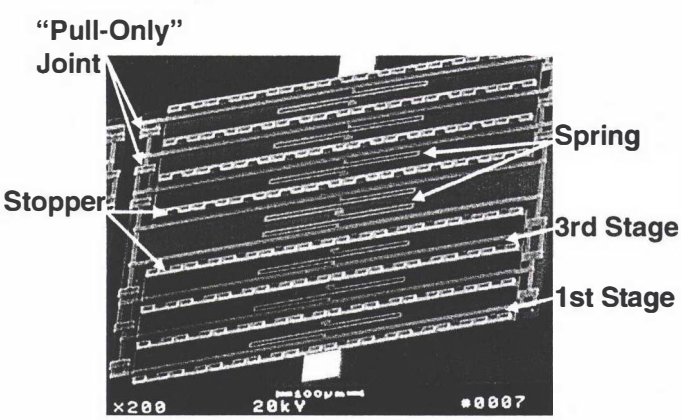

(a)

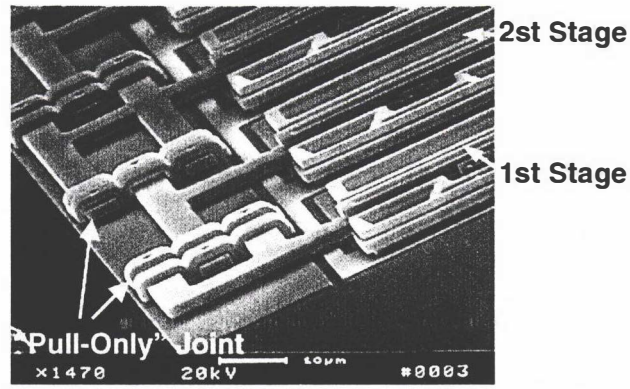

(b)

Figure1. *(a) SEM micrograph of electrostatic domino actuator (EDA). (b)Close-up look of the "pull-only" joint.*

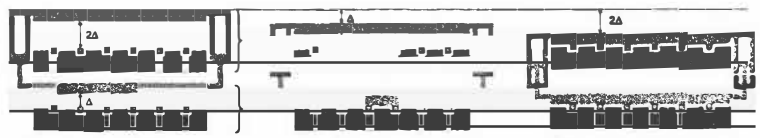

(a) *(b)* *(c)*

Figure2. *Principle of electrostatic domino actuator (only 2 stages are shown here).*

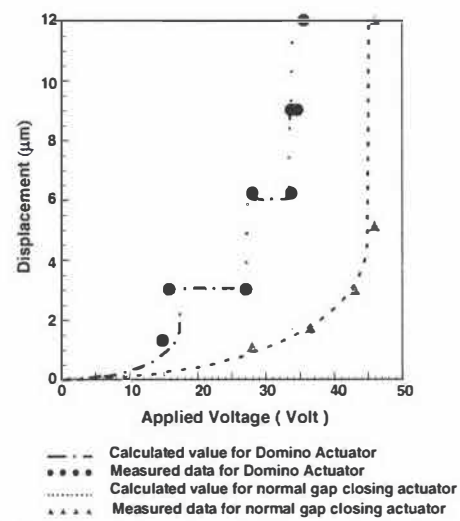

Figure 3. *Displacement vs. applied voltage for EDA and gap closing actuators.*

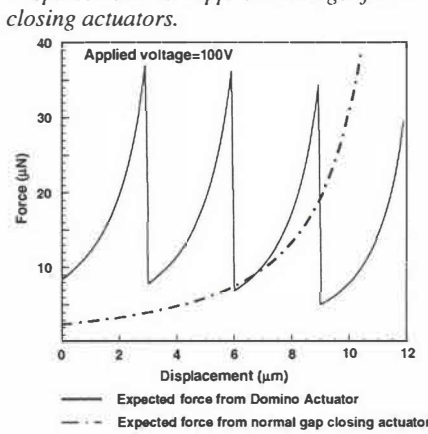

Figure 4. *Displacement vs. forces generated by EDA and gap closing actuators.*

SCANNING BLAZED-GRATINGS FOR HIGH-RESOLUTION SPECTROSCOPY

Jocelyn T. Nee, Kam Y. Lau, and Richard S. Muller
Department of EECS
Berkeley Sensor & Actuator Center
University of California at Berkeley
Berkeley, CA 94720-1774

ABSTRACT

We have used anisotropic etching and subsequent polysilicon surface micromachining in a new process to produce actuated blaze gratings. Using the etch properties of KOH in single-crystal (100)-oriented silicon, we obtain repeatable 54.7° blaze angles in the gratings by making use of the etched grooves as a mold for LPCVD-deposited polycyrstalline silicon. The designer can vary the grating period using conventional lithography techniques. After producing the grating structure in conventional surface-micromachining steps, it is "folded" out from the surface and actuated by an on-chip electrostatic drive. We present experimental results made using prototype polysilicon gratings having an 11.7 μm period in a square pattern 700 μm on a side. We have also produced and assembled 1.3 mm-tall grating structures that are now being tested. The polysilicon plates are mounted on torsion bars and actuated by electrostatic combdrives. If operated as high-order reflective gratings, these prototypes can be used to build integrated spectrometers with a resolving power of 1470 (wavelength resolution of approximately 0.4 nm).

INTRODUCTION

Diffraction gratings are dispersive elements that are commonly used in optical instruments and systems. In addition, their ability to differentiate optical wavelengths makes diffraction gratings particularly suitable as switching components for wavelength-division multiplexing (WDM) communication systems or as wavelength selectors in tunable external-cavity laser systems.

We have previously demonstrated electrostatic comb-driven first-order rectangular gratings fabricated using MCNC's Multi-User MEMS Process (MUMPS) [1]. The resolution and diffraction efficiency of the rectangular gratings are limited by the achievable linewidth of the fabrication process. Because high resolving power and diffraction efficiency are required for WDM and tunable laser systems, the rectangular grating is not satisfactory. Blazed gratings, on the other hand, are not limited by the achievable linewidth and thus offer an alternative solution for improved resolution and diffraction efficiency. Blazed gratings are diffraction gratings with triangular diffracting surfaces (Figure 1), and they obey the grating equation,

$$m\lambda = \Lambda(\sin\theta_m - \sin\theta_i). \qquad (1)$$

In Eq. (1), the diffraction angle θ_m and incident angle θ_i are measured from the grating normal (rather than the facet normal). Blazed gratings have large diffraction efficiency in the order of specular reflection, which is reflection of the light off the planar facet of each diffraction groove. In addition, since resolving power is proportional to the diffraction order, a larger resolving power is achievable due to the use of higher diffraction orders. Figure 2 shows SEM photograph of a combdrive-actuated blazed gratings that we have fabricated.

DESIGN

The electrostatic combdrive actuator for this system consists of 100 interdigitated fingers on the shuttle comb and 101 fingers on the stationary comb. The entire combdrive extended 1 mm in total width, with comb fingers 2 μm wide, 2 μm thick, and 40 μm long. The combdrive is hinged to the bottom of the grating by a cross-woven polysilicon-stripe assemblage to ensure firm locking of the joint. The gratings are mounted on the frames by two 50-μm-long torsion bars (with cross-sectional areas of 2 x 2 μm^2) as the rotational shafts. The dimensions of the polysilicon plates are 700 μm x 700 μm for the small plates and 700 μm x 1300 μm for the large plates. The actual areas of the grating on the plates are 550 μm x 500 μm and 550 μm x 1050 μm for small and large plates respectively.

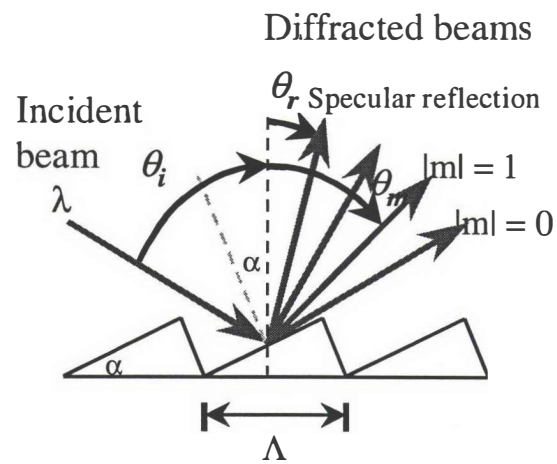

Figure 1. Schematic of a blazed diffraction grating and how it works. The period of the grating is Λ and the blaze angle is α.

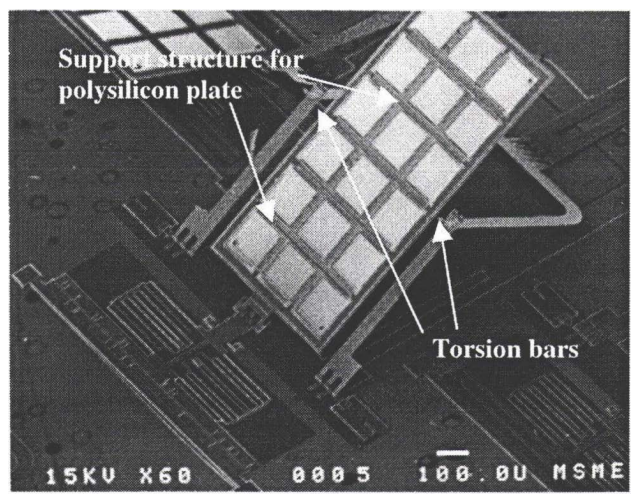

Figure 2. SEM of an actuated scanning blazed-grating. The diffracting surface is on the back side of the plate. The grid structure on the front side is a support structure for the thin polysilicon plate.

0-9640024-2-6/hh1998/$20©1998TRF
DOI 10.31438/trf.hh1998A.5

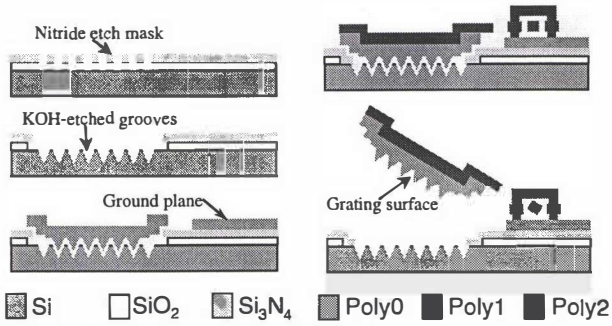

Figure 3. Cross section of the processing sequence for fabricating blazed diffraction gratings using anisotropically etched silicon substrate as mold. The grated polysilicon plate is defined in the Poly0 layer, and the support structure (criss-crossed beams) is defined in the Poly1 layer.

FABRICATION

The blazed diffraction gratings are fabricated in the UCB Microfabrication Laboratory using a new fabrication process, which combines a pre-process of anisotropic KOH etching of silicon and the traditional two-structural polysilicon surface-micromachining process. The processing sequence for the blazed gratings is shown in Figure 3. The mold for the grating surface is formed by parallel V-grooves etched in (100) silicon substrate using anisotropic KOH etching. A total of 49 9.7-μm-wide grooves, spaced by 2 μm, are etched in the silicon substrate. The grating has a blaze angle α of 54.7° as defined by anisotropic KOH etching of (100) silicon. A sacrificial LPCVD silicon dioxide (PSG) layer is deposited on top of the blazed grating mold. The 0.5-μm polysilicon layer (Poly0) deposited in the next step is then "molded" by these grooves and thus forms the grating surface. Support for the thin grating plate is provided by criss-crossed support beams in the first 2-μm structural polysilicon layer (Poly1). SEM photographs of the edge and surface of the grating surface are shown in Figure 4. The electrostatic combdrives are defined in the Poly1 layer, as are the frame and the torsion bars connecting the grating plate to the frame.

CHARACTERIZATION & DISCUSSION

We have measured the diffraction pattern of the blazed grating, as shown in Figure 5. Only the diffraction orders adjacent to the specular order are significant. We have also demonstrated non-resonance scanning of the grating. The mechanical design allows the shuttle comb to travel a distance of 5 μm in the non-resonant mode, which translates into a scanning angle of approximately 10° for a grating that is hinged at 50 μm above the substrate. Detailed characterization of the optical properties will be reported.

CONCLUSION

We have constructed novel scanning blazed gratings for high-resolution spectroscopy. Out-of-plane blazed gratings with dimensions as large as 700μm x 1300μm were fabricated using a new surface-micromachining process which we have developed. These remarkably large, thin plates are actuated by electrostatic combdrives and are structurally supported by wide polysilicon beams. Use of these blazed gratings, which have a wavelength resolution of roughly 0.4 nm and a scan angle of 10°, .in a scanning spectrometer will enable resolution of approximately 400 distinct wavelengths.

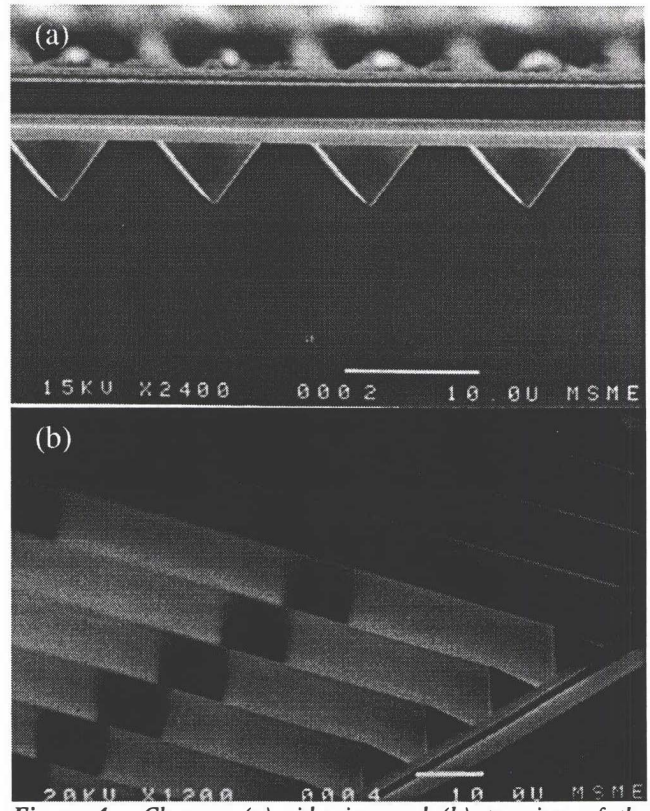

Figure 4. Close-up (a) side-view and (b) top-view of the diffracting surface of the blazed grating. The cross-section is triangular in shape.

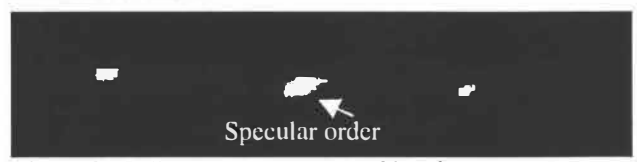

Figure 5. Diffraction pattern of the blazed grating. Diffraction orders not adjacent to the specular order are very small compared to the specular order.

ACKNOWLEDGEMENTS

The authors thank Ron Wilson and Wen-Chin Lee for help in obtaining SEM pictures, and Janice Hudgings for assistance with optical measurements.

This material is based upon work supported under a National Science Foundation Graduate Fellowship and DARPA grant contract number DABT-63-95-C-0055.

REFERENCES

1. M.-H. Kiang, J. T. Nee, K. Y. .Lau, and R. S. Muller, "Surface-Micromachined Diffraction Gratings For Scanning Spectroscopic Applications", *1997 International Conference on Solid State Sensors and Actuators (Transducers'97) Digest of Technical Papers*, Chicago, IL, USA,6/16-19/97, Transducer Research Foundation, Cleveland (1997), vol. 1, pp. 343-345.

DATA TRANSMISSION THROUGH A 16 CHANNEL MICRO-OPTO-MECHANICAL WAVELENGTH ADD/DROP SWITCH

Joseph Ford*, Chang Chung*, James Walker*, Vladimir Aksyuk, David J. Bishop** and Chris Doerr*****

Bell Laboratories, Lucent Technologies,

* Holmdel, NJ 07733-3030, ** Murray Hill, NJ 07974-0636, *** Holmdel, NJ 07733-0400

ABSTRACT

We demonstrate operation of a 16 channel fiber optic wavelength add/drop switch using free space optical wavelength multiplexing and a column of MEMS tilt-mirror switches. 622 Mb/s data transmitted on 8 parallel wavelengths was switched between two input and two output ports without signal degradation.

INTRODUCTION

Wavelength division multiplexed (WDM) fiber optic transmission allows multiple signals on closely-spaced wavelengths to be carried on a single fiber more efficiently than using multiple fibers. The next step beyond simple point-to-point links is dynamic routing of individual data channels into and out of the WDM stream without detecting and retransmitting all of the wavelength channels. Network operators want to reallocate transmission bandwidth in milliseconds for fault protection and to meet changing demands.

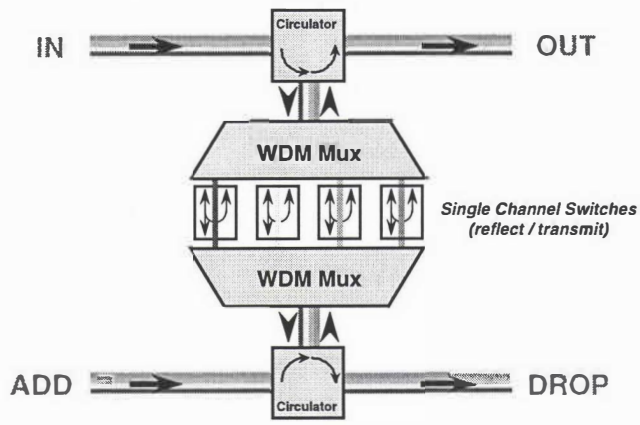

Figure 1. Wavelength add/drop switch layout.

Fig. 1 shows an multi-wavelength switch which demultiplexes the input by wavelength into individual reflect / transmit switches and re-multiplexes the transmitted output. This switch is placed between two optical circulators to separate the forward and backreflected signals and create a four-port component. Reflected signals flow from input to output, but any switch set to transmit routes one signal to the "drop" port and also opens a path from the "add" port to the output.

MICROMECHANICAL ADD/DROP SWITCH

This switch can be built using discrete components such as a waveguide router and individually packaged 1x1 switches. But our switch [1] uses free-space optical imaging through a planar diffraction grating to disperse the inputs onto a column of tilt-mirror switches. This approach offers low insertion loss and the potential to scale inexpensively to extremely large channel counts.

The active switching device (Figure 2) is a column of 16 micro-electro-mechanical tilt-mirrors which operates by electro-static deflection of a gold-coated polysilicon plate, similar to Texas

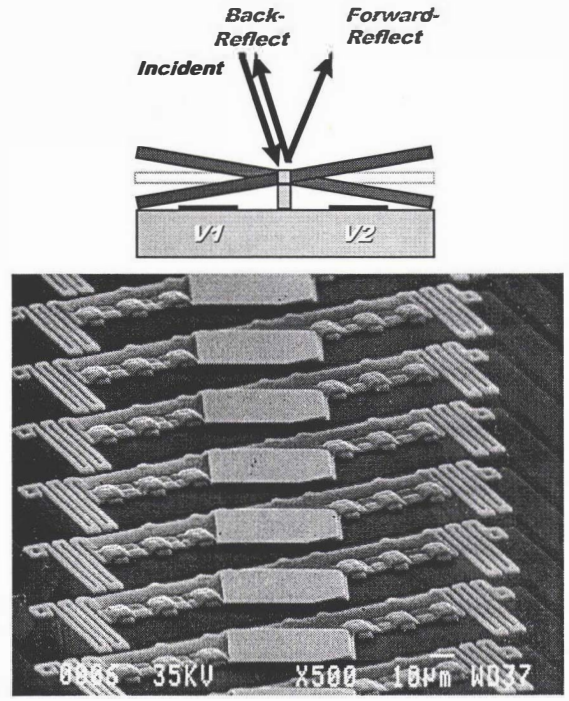

Figure 2. Tilt-mirror switch operation and fabricated device.

Instruments' digital mirror display. Our design was fabricated in MCNC's MUMPS foundry [2]. Approximately 20 volts was required to switch between the two mirror positions, which differed by about 4.5 degrees. Switching time was 20 microseconds.

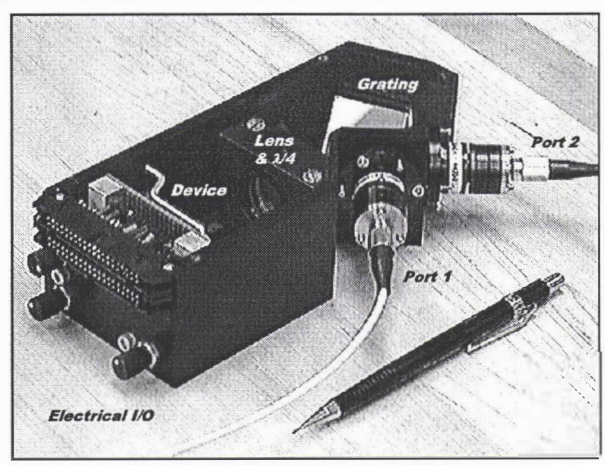

Figure 3. Wavelength multiplexing package.

The free space optomechanical package is shown in Figure 3. A single mode fiber input at port 1 is collimated, then diffracted by a 600 lp/mm grating and imaged onto the micromirror array. Depending on the mirror state, the light is either retroreflected back into the original input port, or tilted by about 9 degrees and carried

0-9640024-2-6/hh1998/$20©1998TRF
DOI 10.31438/trf.hh1998A.6

into a second output port. A λ/4 plate between the lens and grating rotates the reflected light polarization to compensate for any grating polarization dependence. The packaged component, between two commercial circulators, has 5 dB total fiber-to-fiber insertion loss and 0.2 dB polarization dependence, measured with a gold mirror at the device plane and single mode fiber.

With the device in place, the mirror edges define 16 allowed passbands spaced at 1.6 nm intervals.. Figure 4 shows the total fiber-to-fiber insertion loss of the passed and dropped outputs for both switch states measured using a broad spectrum (white light) source at the input. The switching contrast ratio was more than 20 dB for the pass output, and 30 dB (1000:1) for the dropped output. There was no detectable crosstalk between adjacent switches. The maximum insertion loss of 8 dB is better by more than a factor of two compared to our preliminary results previously reported [1].

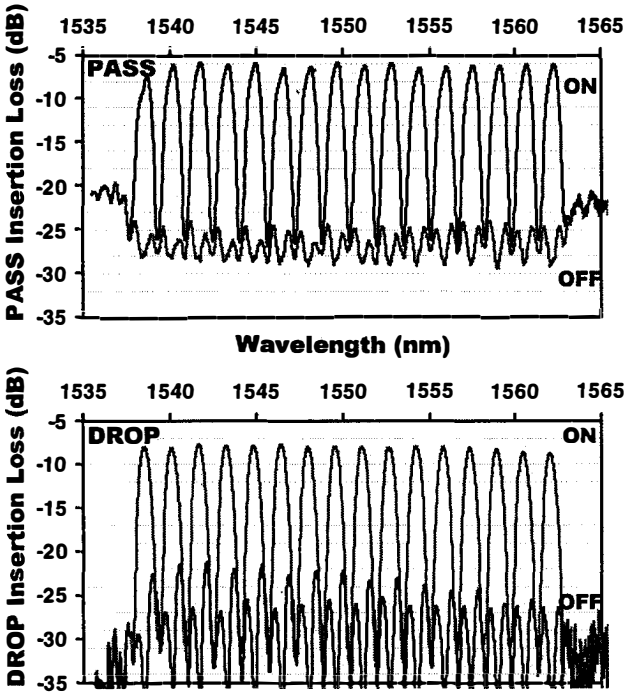

Figure 4: Switching for pass (top) and drop outputs

PARALLEL DATA TRANSMISSION

To operate the add/drop with multiple high-speed inputs, we used a pair of 8 channel x 200 GHz (1.6 nm) multi-frequency lasers [3] to produce multiple superimposed continuous output, then transmitted each fiber through optical modulators driven by two independent data generators to apply 622 Mb/s (OC-12) data patterns. The signals were connected to the input and add ports of the switch, and all the switches were set in either the "pass" or "drop" states, and the routed outputs were directed without demultiplexing into receivers. With this arrangement, crosstalk on any of the 8 channels will show up as closure of the detected transmission eye.

Figure 5 shows the eye diagrams for three cases: transmission from the input to the output, from the input to the drop port, and from the add port to the output. The left column shows the eye for a single data source, while the column on the right shows the same case but with the second signal (a potential source of crosstalk) applied to the switched-off port. In each case, the crosstalk source has no perceptible impact on the eye.

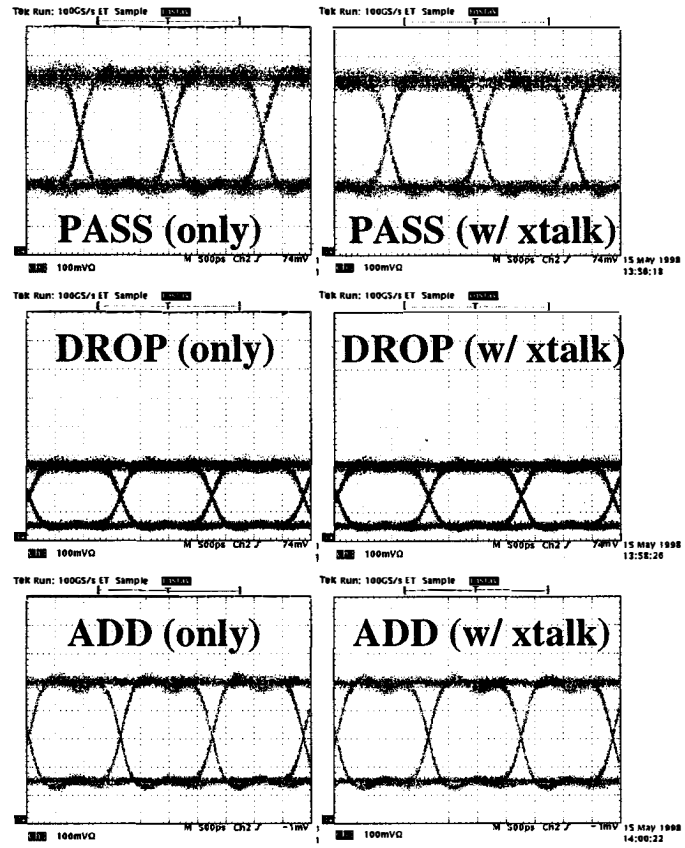

Figure 5. Transmission at 622 Mb/s for 8 summed wavelengths

It is important to note that in a complex optical network, where large numbers of passive components are cascaded, the effects of coherent noise will accumulate and the switching crosstalk performance required to achieve reliable transmission will increase. However, this first demonstration of transmission is encouraging for further development of micromechanically switched passive fiber-optic components

CONCLUSIONS

We have demonstrated parallel operation of the micro-mechanical wavelength-selectable add/drop, showing high-contrast (20 to 30 dB) switching of 8 simultaneous wavelengths channels carrying data at 622 Mb/s.

The authors thank Bob Ellard and Fred Beisser for custom machining, Ted Woodward and Brandon Collings for helpful discussions, Uzi Koren and Kevin Dreyer for the electroabsorption modulator, Charles Joyner and Larry Stultz for growth and packaging of the laser, and everyone whose electronics we "borrowed".

REFERENCES

1. J. E. Ford, J. A. Walker, V. Aksyuk and D. J. Bishop, "Wavelength-selectable add/drop with tilting micromirrors," *IEEE Lasers and Electro-Optics Society Annual Meeting,* Postdeadline paper PD2.3, 1997.

2. http://mems.mcnc.org/mumps.html

3. C. R. Doerr, C. H. Joyner, L. W. Stultz, J. C. Centanni, "Wavelength selectable laser with inherent wavelength and single-mode stability," *IEEE Photonics Technology Letters,* p.1430-2, Nov. 1997.

DEMONSTRATION OF A GAIN FLATTENED OPTICAL AMPLIFIER WITH A MICROMECHANICAL EQUALIZER ELEMENT

J.A. Walker, J.E. Ford, and K.W. Goossen
Lucent Technologies, Bell Laboratories
Holmdel, NJ 07733

ABSTRACT

Free-space optics and micromechanics are combined to produce a wavelength spectrum equalizer for use in dense WDM telecommunications networks. Equalization of the gain spectrum of an erbium doped fiber amplifier is demonstrated wherein the variation of gain over 23 nm is flattened from >13 dB to ±0.25 dB.

INTRODUCTION

In order to accommodate the rapid growth in traffic due to the Internet and data transmission, telecommunications providers are moving rapidly toward the use of dense wavelength division multiplexing (DWDM) solutions. A vital component in DWDM systems is the Erbium-Doped Fiber Amplifier (EDFA). In practice, the usable spectral range of EDFAs has been limited to roughly 12 nm due to the non-uniform gain profiles of these devices. In a chain of amplifiers, gain non-uniformity of one amplifier is further increased in the next stage, leading to transmission errors. A limitation in spectral width translates to a limitation on number of wavelength channels and therefore higher system costs. Fixed filters, such as long period fiber gratings, have been used to expand the usable spectrum to roughly 40 nm, but these cannot respond to changes occurring over the lifetime of the EDFA. Over the lifetime of a system, the power from the laser used to pump the EDFA will change, resulting in a change of the EDFA gain profile. Presently, operators choose sub-optimal performance at system inception to allow for changing pump conditions and an increase in system lifetime. Additionally, as DWDM systems become more complex network reconfiguration, such as wavelength add/drop, is becoming highly desirable. Reconfiguration leads to changing input power distribution to the EDFAs again resulting in transmission errors [1]. We present here a WDM equalizer with the ability to flatten the output of an EDFA with the capability to adapt to changes occurring over the lifetime of the amplifier.

EQUALIZER DEVICE TECHNOLOGY

A WDM equalizer system was reported earlier [2] that utilized segmented MARS elements that allowed independent control over each wavelength channel. While this type of device is very useful for equalizing the intensities of a set of given wavelength channels, the channel spacing is fixed by the spatial resolution of the elements and the optics in the system. In the work we report here, we demonstrate passband-free equalization that allows for equalization independent of channel spacing, as well as continuous smooth shaping of the wavelength spectrum.

In both equalizer configurations, we use the same device technology as that of the MARS optical modulator [3], which is based on optical interference effects between a dielectric film suspended above a substrate and the substrate. For a single element MARS device operating at a wavelength of 1.54 μm, a λ/4-thick membrane (1950 Å) of silicon nitride is formed suspended above a silicon substrate with an air gap equal to 3λ/4 (1.155 μm). The air gap and suspended nitride film form a multi-layer dielectric mirror stack or low finesse Fabrey-Perot cavity. If a voltage is applied between electrodes formed on top of the nitride film and the substrate, the membrane is moved toward the substrate thereby changing the reflectivity of the mirror stack. Attenuation levels of up to 30 dB over a broad wavelength range are attainable as shown in Figure 1.

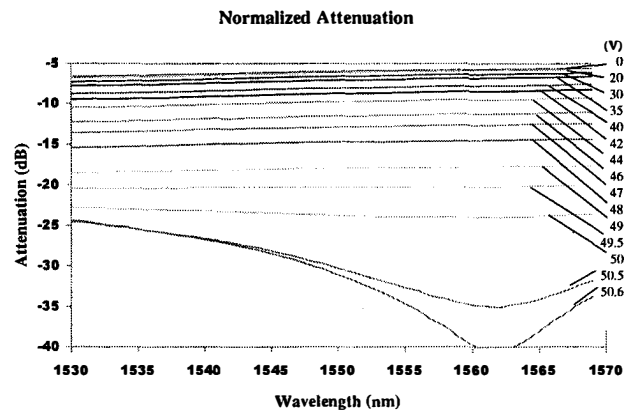

Figure 1. *Measured attenuation spectra of a MARS attenuator vs. applied voltage.*

In the case of a WDM equalizer, we form an optically active region of 35 μm by roughly 1 mm in length. 34 electrically independent electrode pairs are arrayed along the length of the device on a 28-μm pitch as shown in Figure 2. Figure 3 shows the free-space optical system, which directs the output of an EDFA with a spatial spread of wavelength along the 1-mm long length of the equalizer device. In this system, the input signal comes in via Port 1 and is collimated by lens system 1. The collimated beam is then spread out spatially by a diffraction grating and focussed onto the equalizer optical window by a focussing lens. Control voltages applied to the independent electrodes create a smoothly varying deflection of the nitride membrane. This deflection shape results in a reflectivity profile across the length of the optical window yielding the desired flattened spectrum. The shaped spectrum is reflected back through the focus lens, reflected back off the grating and is finally sent to Port 2 (output) via a fold mirror.

0-9640024-2-6/hh1998/$20©1998TRF
DOI 10.31438/trf.hh1998A.7

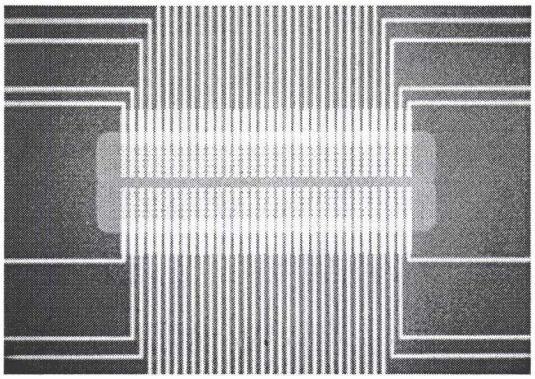

Figure 2. *A WDM equalizer element with an optically active region of 35 μm by 950 μm.*

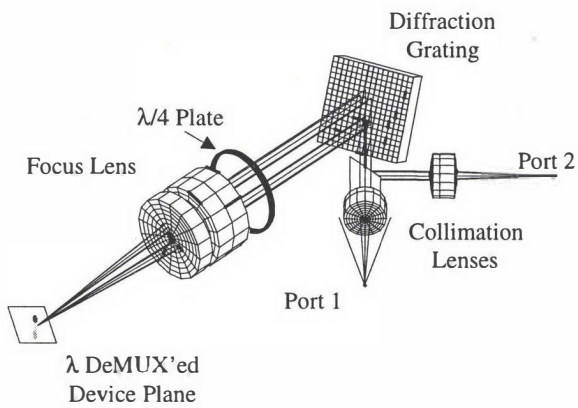

Figure 3. *WDM equalizer free-space optics system.*

EXPERIMENT AND RESULTS

The output of an EDFA amplifier with no input signal is its amplified spontaneous emission (ASE). The ASE is representative of the spectral shaping an EDFA would add to a flat input spectrum. Figure 4 shows the ASE output from a typical amplifier, the ASE signal transmitted through the equalizer without control, and the flattened output from the equalizer. As shown in Figure 4, the ASE input exhibits variation in intensity of over 13 dB across a 23-dB spectrum. The region where it is flat to within a few dB is roughly 12 nm. The transmitted spectrum shows an insertion loss of roughly 8 dB from the equalizer, but we feel some of this was due to optical system misalignment and expect that the insertion loss could be as low as 3 dB. The flattened spectrum shown in Figure 4 demonstrates the capability of reducing the dynamic range of the input signal from >13 dB to ±0.23 dB over a 23.5 nm bandwidth. In order to obtain the flat gain response, an additional 2-dB loss penalty was incurred (as evidenced over the range of 1337-1340 nm). The penalty resulted from the inability of the continuous membrane to affect a large change in required deflection over such a short distance as required by the large slope of the gain curve in this region.

CONCLUSIONS

We have demonstrated the ability to flatten the gain curve of an EDFA amplifier to ±0.23 dB over a 23.5 nm spectral width. In present DWDM systems, this would translate to an increase in the number of wavelength channels from 8 to 15, nearly doubling the capacity of the network. In addition to the increase in capacity, this method of spectral control also provides the ability to adapt to changing gain shape over the lifetime of the EDFA amplifier.

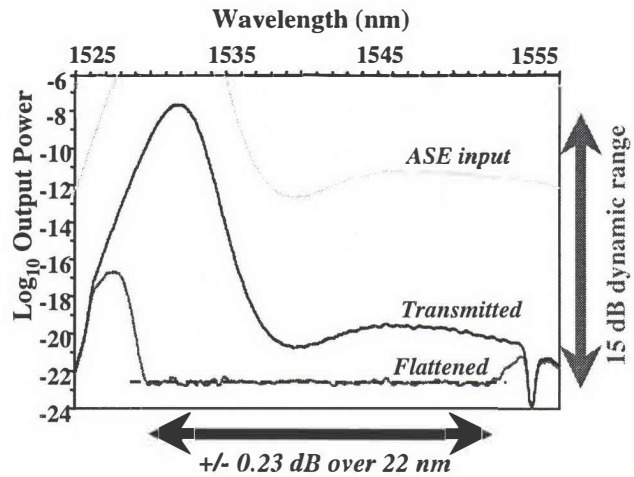

Figure 4. *Gain spectra for an erbium-doped fiber amplifier showing the signal directly from the amplifier, through the equalizer without perturbation, and gain flattened by the equalizer.*

REFERENCES

[1] Y. Sun, A.K. Srivastava, J.L. Zyskind, J.W. Sulhoff, C. Wolf, and R.W. Rkach, "Fast Power Transients in WDM Optical Networks with Cascaded EDFAs", *Electronics Letters*, Vol. 33, pp. 313-314, (1997).

[2] J.E. Ford, J.A. Walker, M. Nuss, and D.A.B. Miller, "32 Channel WDM Graphic Equalizer", *IEEE/LEOS 1996 Summer Topical Meeting on Broadband Optical Networks*, Keystone, CO, August 5-7, 1996 pp.26-27.

[3] K.W. Goossen, J.A. Walker, S.C. Arney, "Silicon modulator based on mechanically-active anti-reflection layer with 1 Mbit/sec capability for fiber-in-the-loop applications", *IEEE Photonics Technology Letters*, Vol. 6, No. 9, Sept. 1994, pp. 1119-1121.

THICK SINGLE CRYSTAL Si LATERAL RESONANT DEVICES INTEGRATED WITH A CONVENTIONAL CIRCUIT PROCESS

J. W. Weigold, A.-C. Wong, C. T.-C. Nguyen, and S. W. Pang
Department of Electrical Engineering and Computer Science, The University of Michigan
Ann Arbor, MI 48109-2122

ABSTRACT

A new, simple process has been developed which integrates thick single crystal Si lateral resonators with a standard circuit process. The process allows for the fabrication of mechanical devices as thick as 11 μm to be integrated with any conventional integrated circuit process with the addition of only a single masking step. Single crystal Si resonators have been fabricated and tested with working metal oxide semiconductor (MOS) transistors on the same chip. An 11 μm thick, 500 μm long clamped-clamped beam comb driven resonator is demonstrated with a resonant frequency of 32.3 kHz and an amplitude of vibration of 7.1 μm in air.

INTRODUCTION

One of the drivers in the micromachining industry is the ability to integrate mechanical structures with circuits. This can be used in sensors to detect a small signal produced by a sensor without having to take the signal off chip where parasitics are large. The ability to fabricate resonators and sensors with circuitry on the same chip, allows much more sensitive devices to be fabricated and small signals to be amplified and conditioned in a single device. There are products currently in volume production which utilize sensors with signal conditioning circuitry on the same ship. Most of these processes are surface micromachining processes in which the structural material is polysilicon and its thickness is limited. Also stress must be carefully tailored in the polysilicon film. Single crystal Si has excellent mechanical properties and thus it is a desirable material with which to fabricate mechanical devices. A process has been developed which combines the excellent properties of thick single crystal Si mechanical devices with the advantage of on chip circuitry.

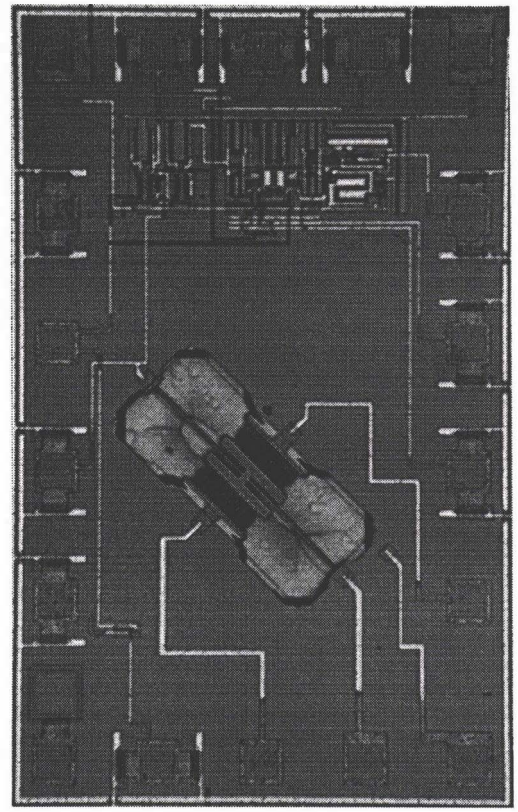

Figure 2. Photograph of the clamped-clamped beam resonator integrated with the transimpedance amplifier.

EXPERIMENTAL DETAILS

A schematic of the process flow used to fabricate the devices is shown in Fig. 1. [1,2] First, a deep B diffusion was selectively performed which will determine the thickness of the resonator. Devices can be fabricated

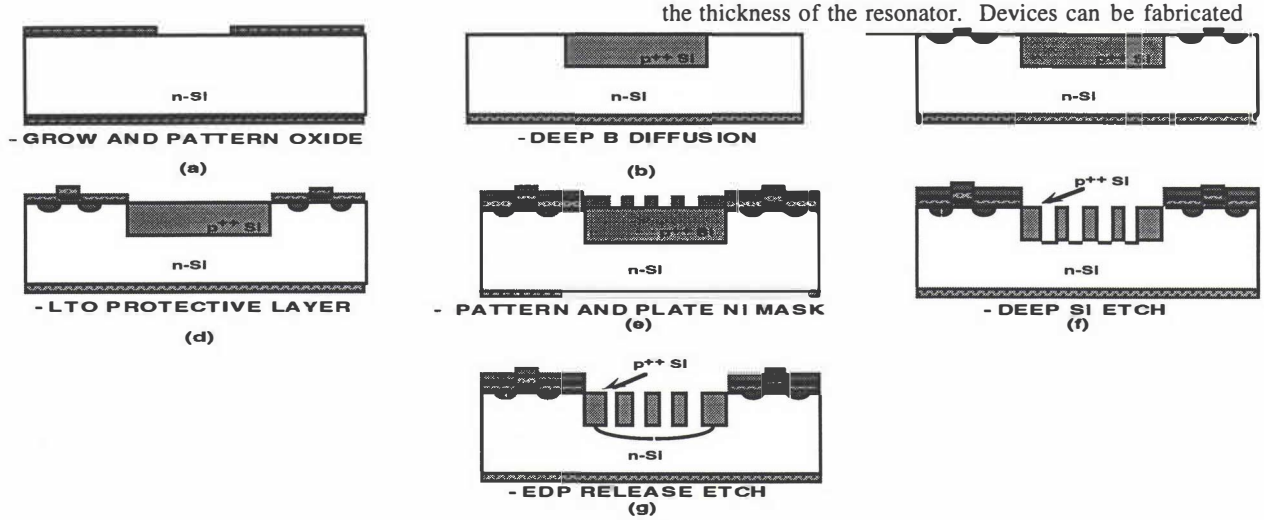

Figure 1. Schematic of the process used to fabricate the resonators and circuits

0-9640024-2-6/hh1998/$20©1998TRF
DOI 10.31438/trf.hh1998A.8

with any thickness up to the available thickness of a diffused B layer which is about 15 μm. Next, the standard circuit processing is done. Since the circuit processing is totally independent of the resonator processing, any circuit process can be used. A low temperature oxide was then grown on top of the circuit to serve as a passivation layer, and to later protect the transistors from an ethylenediamine pyrocatechol (EDP) etch. A Ni mask was electroplated through a photoresist mold which served as the etch mask for the dry etch. A dry etch in an inductively couple plasma (ICP) source using 250 W source power, 70 W stage power at 5 mTorr with 20 sccm of Cl_2 flow and a source to sample distance of 8 cm was performed. This etch defines the resonators and high aspect ratio elements can be achieved with fast etch rates in the ICP source. An EDP etch was done in order to undercut and release the structure. The EDP solution did not etch the heavily B doped Si structure. Finally, the Ni mask was removed. A photograph of the die with a clamped-clamped beam resonator and a transimpedence amplifier is shown in Fig. 2.

The transimpedance amplifier detection circuitry was fabricated using a 3 μm, 2-poly, 1-metal BiCMOS process at the University of Michigan. The amplifier has a measured 3 dB frequency of 100 kHz. To minimize power consumption, the transistors are operated in the subthreshold regime, with a bias current of less than 250 nA. For a 0-5 V rail-to-rail supply, the power dissipation is approximately 1.25 μW. The characteristics of an NMOS transistor was measured after the EDP release step and the I-V curves are shown in Fig. 3.

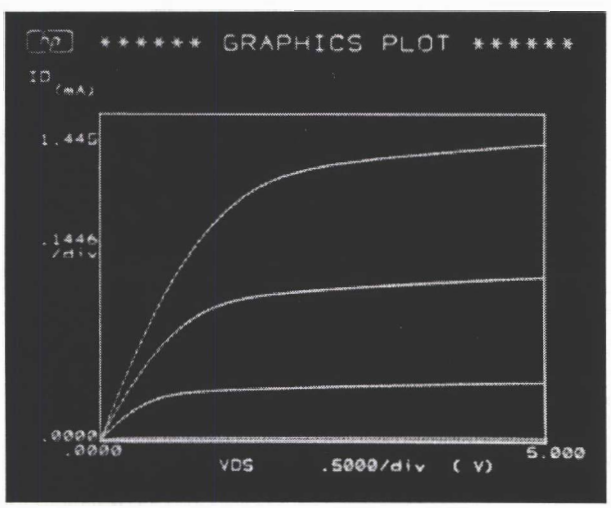

Figure 3. NMOS I-V curves for a transistor on the same die as the measured resonator after structure release.

The single crystal Si clamped-clamped beam comb drive resonator shown in Fig. 4 has been fabricated and tested in order to validate the integrated process. Figure 5 shows a close-up of the comb drive used to drive and sense movement in the resonator. The resonant beam was 11 μm thick, 5 μm wide, and 500 μm long with 3 μm wide comb fingers and 3 μm wide gaps between fingers. The resonant frequency of the devices was measured to be 32.3 kHz and a maximum amplitude of vibration of 7.1 μm was measured at the resonant frequency.

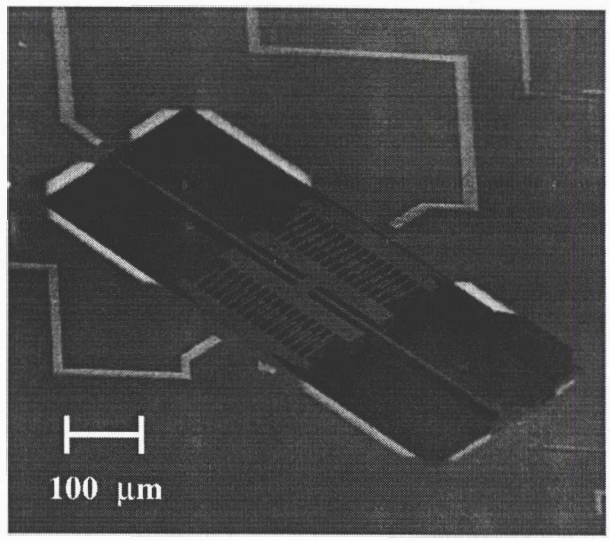

Figure 4. Micrograph of 11 μm thick, 500 μm long released resonator with 3 μm wide combs and 3 μm wide gaps.

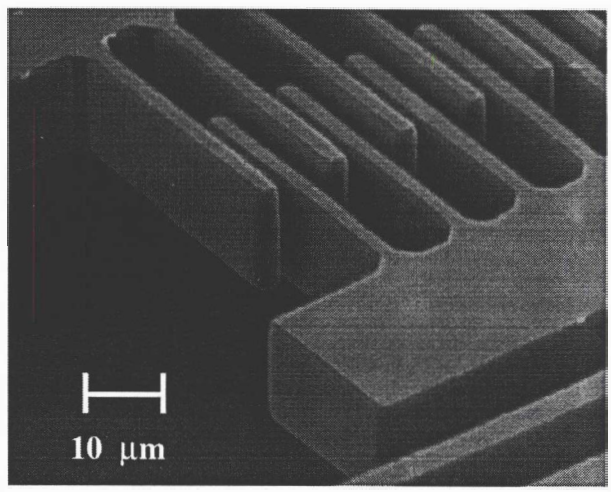

Figure 5. A close-up of the electrostatic comb drive with 3.0 μm wide fingers and 3.0 μm wide gaps.

SUMMARY

A simple process has been developed in which an 11 μm thick single crystal Si resonator has been integrated with BiCMOS circuitry.

REFERENCES

[1] Y. B. Gianchandani and K. Najafi, "A bulk silicon dissolved wafer process for microelectromechanical devices", IEEE J. Microelectromech. **1** (1992) pp. 77-85.

[2] J. W. Weigold and S. W. Pang, "A New Frontside-Release Etch-Diffusion Process for the Fabrication of Thick Si Microstructures", Transducers '97, Chicago, IL, pp. 1435-1438, 1997.

MEASUREMENTS OF THE EFFECT OF SPECIMEN SIZE ON YOUNG'S MODULUS AND TENSILE STRENGTH OF POLYSILICON

William N. Sharpe, Jr. and Kevin Turner
Department of Mechanical Engineering,
The Johns Hopkins University
Baltimore, Maryland 21218-2686

Richard. L. Edwards
Applied Physics Laboratory
The Johns Hopkins University
Laurel, MD 20723-6099

ABSTRACT

Techniques and procedures are described for tensile testing of polysilicon specimens that are 1.5 or 3.5 μm thick and have various widths and lengths. The specimens are fixed to the wafer at one end and have a large free end that can be gripped by electrostatic forces. This enables easy handling and testing and permits the deposition of 18 specimens on a one-centimeter square portion of a wafer. The displacement of the free end is monitored, which allows one to extract Young's modulus from the force-displacement record. Some of the wider specimens have two gold lines applied so that strain can be measured interferometrically directly on the specimen to record a stress-strain curve.

The specimens were produced at the Microelectronics Center of North Carolina (MCNC). Earlier measurements on wider MCNC specimens that were 3.5 μm thick gave a modulus of 169 GPa. The narrower 3.5 μm thick specimens tested here had a modulus of 142 GPa, and the 1.5 μm thick specimens showed 136 GPa. The strengths measured earlier on wider specimens averaged 1.20 GPa, but the average strength for each thickness tested here was 1.3 Gpa. The different widths and lengths for each thickness had no systematic effect on the Young's modulus or strength.

INTRODUCTION

There is an obvious need for accurate measurements of the elastic and strength properties of polysilicon, but conducting stress-strain tests is not so easy. In earlier work [1], 3.5 μm thick polysilicon tensile specimens that were 600 μm wide and 4 mm long were prepared by etching away the underlying silicon wafer. The large grip ends were glued into a small test machine and two supporting side strips were then cut with a diamond saw to completely free the specimen. Friction in the load train was eliminated by a linear air bearing, and the specimen was elongated by an electrostatic actuator.

Strain was measured by laser interferometry between two gold lines 0.5 μm thick and 20 μm wide that were deposited on the central portion of the tensile specimen. In fact, two sets of gold lines were used to enable the first-ever measurements of Poisson's ratio of this thin material. Very consistent results were obtained — Young's modulus of 169 ± 6 GPa and strength of 1.20 ± 0.15 GPa for 48 tests from five different production runs. Nineteen of those tests had two sets of gold lines to measure Poisson's ratio of 0.22 ± 0.01.

The disadvantage of this approach is that only one specimen is available per die and the etching procedure is time consuming. Tuschiya et al [2] conceived a new technique in which narrow tensile specimens are deposited with one end fixed and the other free so that it can be gripped by electrostatic forces. This makes it easier to handle the specimens and allows one to deposit many specimens on a die. Tuschiya has conducted an extensive series of tests to measure the strength of polysilicon.

Greek et al [3] tested polysilicon tensile specimens that have one end fixed to the substrate. The free end has a large ring into which a probe is fitted for a mechanical connection to the specimen. They measured the overall displacement as a function of force and used specimens of two different lengths to eliminate the unknown stiffness of the test system. By this method, they measured both Young's modulus and strength.

The approach used here is a combination of the three described above. The specimens are similar in shape to those of Tuschiya et al so that they can be gripped electrostatically, and displacement is recorded as well. Some of the wider specimens have two gold lines on them (none are wide enough for two sets) so that strain can be measured directly.

SPECIMEN SHAPE AND TEST SETUP

Figure 1 is a schematic of the new test setup and of the specimen. The polysilicon specimen remains fastened to the substrate at one end; the other large end is gripped electrostatically by an insulated probe. The specimen substrate is mounted on a piezoelectric stage with a least count displacement on the order of 10 nanometers. The probe is attached to a load cell mounted on a 3-axis micrometer stage to allow positioning and alignment. The laser is focused on two thin gold lines deposited in the center of the tensile specimen; this generates interference fringes which are monitored with photodiode arrays to record their motion [1]. A capacitance-based displacement transducer records the displacement of the specimen mount. The test is conducted under computer control and records force, strain, and displacement.

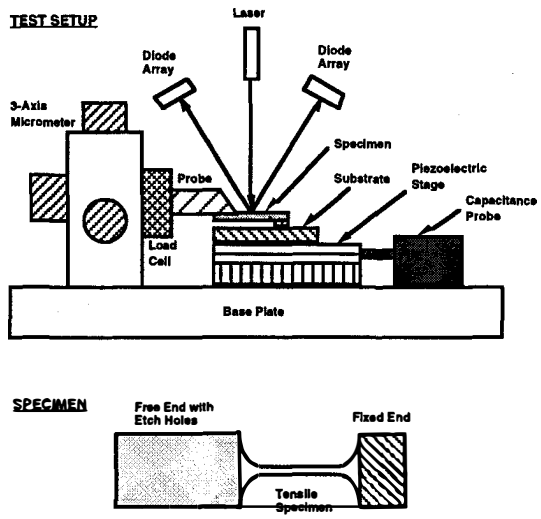

Figure 1. Schematic of the specimen and the test setup.

0-9640024-2-6/hh1998/$20©1998TRF
DOI 10.31438/trf.hh1998A.9

Figure 2 is a photograph of the specimens that were manufactured by the Microelectronics Center of North Carolina on their MUMPs 19 run. There are 18 specimens on a one-centimeter square chip; nine are 1.5 μm thick and nine are 3.5 μm thick. The specimens have various widths ranging from 2 to 50 μm and lengths ranging from 20 to 500 μm to permit examination of the effect of specimen size on the mechanical properties.

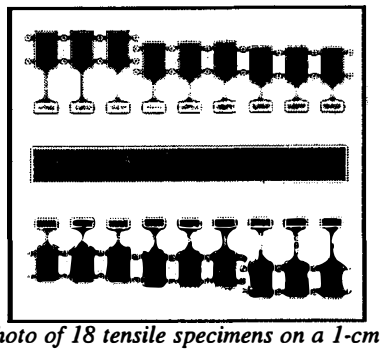

Figure 2. Photo of 18 tensile specimens on a 1-cm square die.

FORCE-DISPLACEMENT AND STRESS-STRAIN

One can extract Young's modulus from the record of the force versus displacement of the system if the stiffness of the measurement system is known. Figure 3 is a plot of the force-displacement record for two specimens on the same die, and the modulus is calculated using a system stiffness of 0.00651 N/μm.

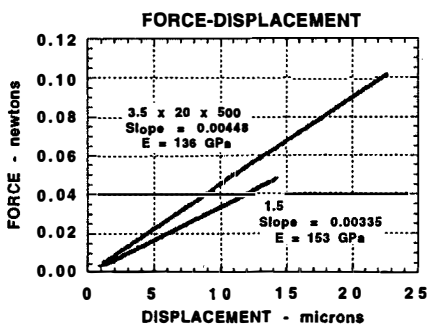

Figure 3. Force-displacement record of two specimens identical in shape, but of different thicknesses.

One can also measure the strain directly on the larger specimens as reported earlier [1], and two stress-strain curves are shown in Figure 4.

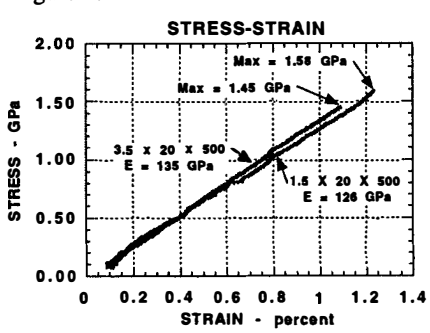

Figure 4. Stress-strain record of the same two specimens whose force-displacement curves are shown in Figure 3.

Figures 3 and 4 show similar behavior (within the scatter of the results) for the two specimens of different thickness.

PRELIMINARY MODULUS AND STRENGTH DATA

Several tests have been conducted, and an extensive test program is underway. Figures 5 and 6 show the preliminary results to date.

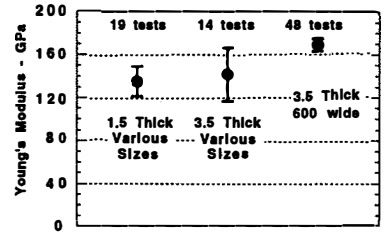

Figure 5. Modulus data for various sizes.

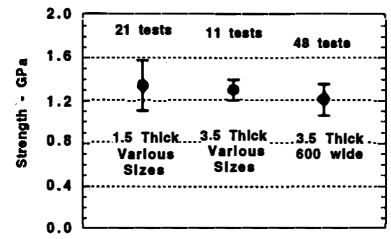

Figure 6. Strength data for various sizes.

No trends of modulus or strength with specimen width or length were observed for either thickness.

CONCLUSIONS

The decrease in modulus as the specimen size gets smaller is in contradiction with what one would expect. On the other hand, the variation in strength, although slight, is not so surprising. The microstructure of vapor deposited polysilicon is columnar in structure perpendicular to the film [1]. It is not unreasonable to expect that the nature of this grain structure changes as the 'mold' into which the polysilicon is deposited becomes smaller. Detailed microstructural examinations are underway to complement the continuing test program.

ACKNOWLEDGMENTS

This research was sponsored by the National Science Foundation and by the Air Force Office of Scientific Research.

REFERENCES

1. W. N. Sharpe, Jr., , B. Yuan, R. L. Edwards, and R.Vaidyanathan, "Measurements of Young's modulus, Poisson's ratio, and Tensile Strength of Polysilicon", *Proc. Tenth IEEE International Workshop on Microelectromechanical Systems*, Nagoya, Japan, pp. 424-429 (1997).

2. T. Tsuchiya, O. Tabata, J. Sakata, and Y. Taga, "Specimen Size Effect on Tensile Strength of Surface Micromachined Polycrystalline Silicon Thin Films", *Proc. Tenth IEEE International Workshop on Microelectromechanical Systems*, Nagoya, Japan, pp. 529-534 (1997).

3. S. Greek and S. Johansson, "Tensile Testing of Thin Film Microstructures", *Micromachined Devices and Components III - SPIE, Volume 3224*, pp. 344-351 (1997).

A ROBUST CAPACITIVE PRESSURE SENSOR ARRAY

Jeong-Bong Lee, Sung-Pil Chang, and Mark G. Allen
School of Electrical and Computer Engineering, Georgia Institute of Technology, Atlanta, Georgia 30332-0269
Phone: (404) 894-8807, Fax: (404) 894-5028, e-mail: jeong-bong.lee@ece.gatech.edu

ABSTRACT

In this work, robust substrates, such as a stainless steel, are studied as substrates for micromachined devices. The use of robust substrates may allow for the co-fabrication of micromachined sensors and sensor packages. Lamination combined with traditional micromachining processes has been investigated as a suitable technology for these investigations. To illustrate this technology, a capacitive pressure sensor array has been designed, fabricated, and characterized using a stainless steel substrate, Kapton film as a diaphragm, and an electroplated nickel fixed back electrode. The net capacitance change over the applied pressure range (0 to 34 kPa) was approximately 0.23 pF.

INTRODUCTION

Micromachined devices have been primarily realized using silicon substrates [1]. In this work, the use of robust substrates (such as stainless steel) as suitable starting points for both bulk and surface micromachined structures, as well as the possibility of the substrate forming essential structural components of the device package, have been investigated. In addition to new robust substrates, alternative fabrication techniques such as lamination have been studied. To illustrate these principles, a robust capacitive pressure sensor array has been fabricated with ultimate application to flow control problems, such as the guidance of unmanned airborne vehicles (UAV). An important attribute of this design is that only the steel plate and the pressure sensor inlet is exposed to the flow; i.e., the sensor is self-packaged.

THOERY AND DESIGN

The sensor device concept is based on the pressure-induced deflection of a metallized diaphragm and the subsequent measurement of the capacitance between this deflecting diaphragm and a fixed surface micromachined backplate suspended over the diaphragm.

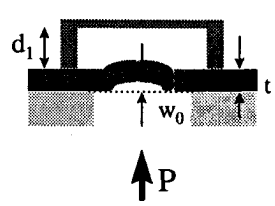

Figure 1. *A schematic diagram of the side-view of the capacitive pressure sensor.*

Figure 1 shows a schematic diagram of the side-view of the device, where d_1 is an initial gap distance between the fixed back electrode and the flexible diaphragm electrode, w_o is the deflection at the center of the diaphragm, t is the thickness of the flexible Kapton diaphragm, and P is the applied pressure. For analytical modeling, several assumptions have been made: (a) neglect stretching on the diaphragm, (b) neglect thickness of metallic electrode on the diaphragm, and (c) neglect fringing effects. The sensor capacitance can be described as follows:

$$C_{sensor} = \varepsilon_0 \int_0^{2\pi}\int_0^{a} \frac{r dr d\theta}{\left(d_1 - w(r)\right)}, \qquad (1)$$

where a is the radius of the diaphragm, and $0 \le r \le a$. The solution of equation (1) can be expressed as a Taylor series expansion as follows:

$$C_{sensor} = C_0\left(1 + K_1 P + K_2 P^2 + \cdots\right), \qquad (2)$$

where C_0 is the capacitance when the diaphragm is undeflected, and K_n are constants.

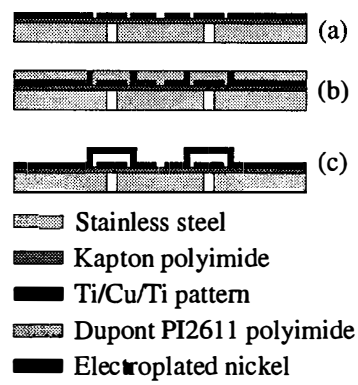

Figure 2. *Fabrication sequence: (a) lamination of milled stainless steel and Kapton polyimide film and bottom electrode patterning; (b) polyimide deposition and electroplating of nickel posts; (c) backplate electroplating and removal of polyimide sacrificial layer.*

FABRICATION AND MEASUREMENT

The fabrication sequence of the robust capacitive pressure sensor array is shown in Figure 2. The process began with milling an 8*8 array of pressure inlet holes (2mm diameter) in a 0.5 mm thick, 2 1/4 inch on a side stainless steel shim stock. Lamination of Dupont Kapton HN200 (50 μm thick) polyimide film on the stainless steel was performed using a hot press. The regions of the Kapton polyimide film over the pressure inlet holes will form the pressure-sensitive diaphragms. A Ti/Cu/Ti (200/2,000/500 Å respectively) metallic layer was deposited on the Kapton surface and patterned using a lift-off technique to form bottom electrodes, bonding pads, and electroplating seed layers for backplate posts (see Figure 3). Multiple layers of Dupont polyimide PI2611 were coated on the patterned metallic layer, hard cured (resulting in a final thickness of 36 μm), and anisotropically dry etched using reactive ion etching to form plating molds. Nickel was electroplated through the polyimide molds to form backplate posts. Another Ti/Cu/Ti metallic seed layer was deposited and thick photoresist (Shipley PR 5740) was patterned as electroplating

0-9640024-2-6/hh1998/$20©1998TRF
DOI 10.31438/trf.hh1998A.10

molds for the fixed backplates. Electroplated nickel backplates approximately 15 μm thick were formed and the photoresist molds and metallic seed layers were removed. Finally, an isotropic dry etch process was performed using a barrel plasma etcher (a gas mixture of O_2 and CF_4) to remove the polyimide molds for backplate posts as well as polyimide sacrificial layers to create air cavities between the fixed backplates and the pressure sensitive Kapton polyimide diaphragms. Figure 4 shows photographs of a fabricated pressure sensor array, where (a) gives a side-view and (b) gives a close-up view of the gap defined between the backplate and the diaphragm.

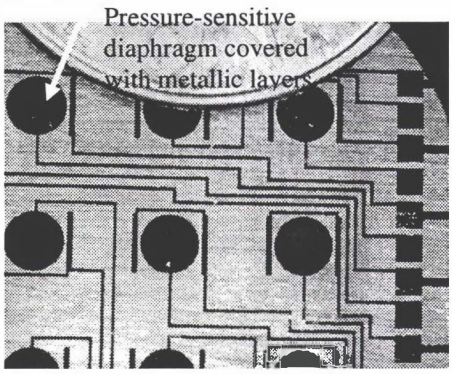

Figure 3. A photograph of top-view of the metallic seed layer which corresponds to the fabrication sequence shown in Figure 2 (a). The pressure-sensitive diaphragms are located underneath the circular metallic patterns. The array is shown next to a penny for size comparison.

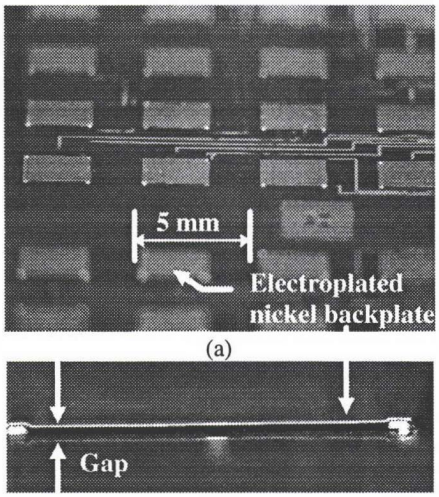

Figure 4. Photographs of fabricated pressure sensor array: (a) A side-view of the pressure sensor array; (b) a close-up view of the gap (approximately 36 μm) defined between electroplated nickel backplate and pressure sensitive Kapton diaphragm.

The capacitance of individual sensors was measured using a Keithley 3322 LCZ meter. Measured capacitances for undeflected pressure sensors were in the range from 11.02 pF to 17.52 pF depending on the length of interconnections between bonding pads and sensors. It was observed that capacitance monotonically increases for increasing applied pressure, meaning that the pressure sensitive Kapton diaphragm deflects toward the fixed backplates. Over an applied pressure range from 0 to 34 kPa, the net capacitance change was approximately 0.23 pF. Theoretical and measured net capacitance change over the applied pressure range are compared in Figure 5. Theoretical data shown in Figure 5 is based on initial gap of 33 μm. There is approximately 10% difference between the measured gap and the theoretical gap value, and this difference could be explained by fringing effect of the sensor capacitance. The measured values of relative capacitance change are in the range from 1.54 % to 2.14 %. The values of capacitance changed produced by the sensors are easily measurable in their current form; however, if required, the parasitic effect can be reduced using an unchanging reference capacitance and appropriate subtraction circuitry. By doing so, the relative capacitance change over the applied pressure range could be increased to 22.3%.

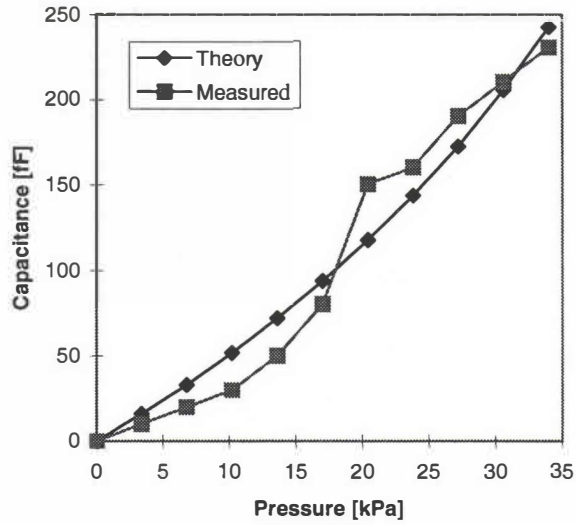

Figure 5. A comparison of theoretical and measured values of net capacitance change over the full range of applied pressure ranging from 0 to 34 kPa (10 in-Hg).

CONCLUSIONS

Robust materials have been studied as suitable substrates for micromachined devices. Lamination using a hot press, combined with traditional micromachining processes, has been investigated as a suitable fabrication process for the robust substrates. A capacitive pressure sensor array using a robust substrate (500 μm thick stainless steel shim stock), Kapton HN200 diaphragm, and lamination processing has been designed, fabricated, and characterized. Over the applied pressure range from 0 to 34kPa, the net capacitance change of the pressure sensor is approximately 0.23 pF.

ACKNOWLEDGMENT

The support of the staff of the Microelectronics Research Center at Georgia Tech is acknowledged. This work was supported by Defense Advanced Research Project Agency (DARPA) and Air Force Office of Scientific Research (AFOSR) under Contract F49620-97-1-0519.

REFERENCES

1. H. Baltes, "CMOS Micro Electro Mechanical Systems," *Sensors and Materials*, v. 9, n. 6, p.331-346 (1997).

SELF-ALIGNED POLYSILICON MEMS- REDUCED MASK COUNT SURFACE MICROMACHING

J.Mark Noworolski & S.R Sanders
EECS, 341 Cory Hall,
University of California, Berkeley, 94720

ABSTRACT

A burst-proof surface micromachined polysilicon resonant pressure sensor is designed, fabricated, and tested. Fabrication is conducted by a versatile 2 mask self-aligned micromachined polysilicon on nitride (SAMPSON) process. As compared to conventional sacrificial oxide based surface micromachining approaches, this fabrication sequence enables rapid fabrication, improves yields, and reduces parasitic capactances.

INTRODUCTION

To date, polysilicon based surface micromachining techniques have been used to fabricate lateral [1] and vertical resonators. These fabrication techniques typically require 3 or more masking steps for basic designs. In this work, we present a versatile 2 mask self-aligned micromachined polysilicon on nitride (SAMPSON) process. This process results in extremely rapid fabrication, high yields, and low parasitic capacitances.

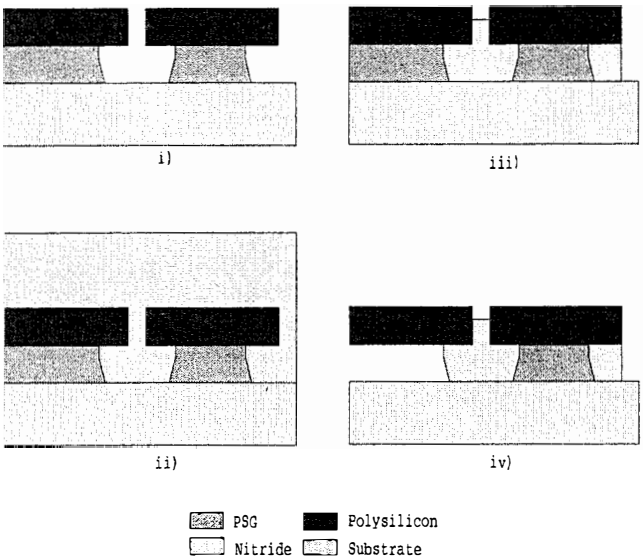

Figure 1: SAMPSON process flow. Cross sections correspond to cut line AB in Figure 2.

Due to the self-alignment feature, the SAMPSON process flow can fabricate virtually all conventional lateral and vertical surface micromachined devices with a one mask savings over conventional approaches.

To date, most microelectromechanical (MEM) pressure sensors are fabricated with a sealed vacuum cavity which acts as a pressure reference [2]. Hence, MEM pressure sensors are usually fabricated using costly combinations of wafer bonding and surface or bulk micromachining methods.

In this work, a novel burst-proof pressure sensor is fabricated using only the surface micromachined SAMPSON process flow. This squeeze-film based resonant pressure sensor does not require a sealed vacuum chamber, simplifying processing. Furthermore, the burst pressure limitation is established by mechanical brittleness limits of uniformly compressed Silicon, rendering the pressure sensor essentially burst-proof.

FABRICATION

The basic SAMPSON process flow, illustrated in *Figure 1*, begins with an n type silicon substrate. The first step deposits a 1μm layer of CVD phosphosilicate glass (PSG), the sacrificial layer, followed by a 2μm structural layer of polysilicon. The thickness of the PSG layer defines the spacing of the final device from the substrate.

The structural polysilicon is then patterned and etched. This etch step defines the perimeter of the areas of the final device which are to be attached to the substrate (*Figure 2*). The thickness of the device is defined by the as-deposited polysilicon thickness.

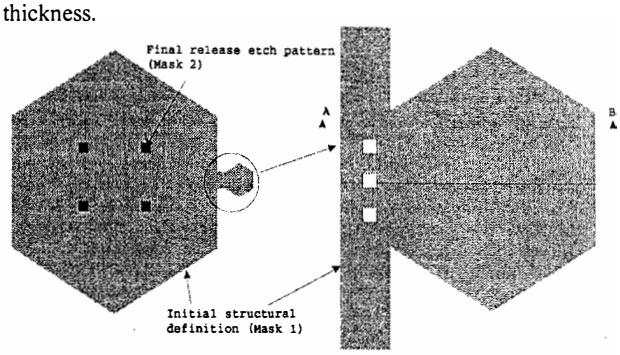

Figure 2: SAMPSON vertical resonator layout

Next, an anneal and subsequent timed 5:1 BHF etch is performed, removing PSG and undercutting the polysilicon regions as shown in *Figure 1*i. In this work, the undercut distance was approximately 5μm, but it can be varied from a few to tens of μm.

Next, 1.3μm of CVD silicon nitride is deposited. This is a conformal process, depositing nitride underneath the undercut areas as well as on exposed surfaces.

This conformal lateral deposition is a key concept in any SAMPSON-based process flow. Naturally, SAMPSON-based process flows can use undoped polysilicon, tungsten, or other conformally deposited materials instead of silicon nitride.

Of course, to achieve complete refill of the undercut regions the conformal deposition thickness must equal at least half the sacrificial layer thickness. In this work, the deposition of silicon nitride forms fully refilled insulating supports for our resonators, but thinner layers of silicon nitride can be deposited to form different structure geometries. For example, thin depositions can enable out-of-plane-pivoting polysilicon lever fabrication.

The deposited nitride is now removed by a two fold process, a plasma etch followed by a more selective hot phosphoric acid etch. This leaves areas of silicon nitride which were 'shadowed' by polysilicon areas, in effect self-aligning the nitride support regions (*Figure 1*iii).

A second and final lithography and polysilicon etch step completes the fabrication process, defining the release etch holes (for membrane resonators) or movable areas (for lateral

0-9640024-2-6/hh1998/$20©1998TRF
DOI 10.31438/trf.hh1998A.11

resonators). Finally, an HF release prepares the devices for test (*Figure 1*iv).

FABRICATION DISCUSSION

Figure 2, a low parasitic capacitance bond pad layout, demonstrates a feature of the SAMPSON process flow. Post-release, this layout results in a bond pad comprised of polysilicon on top of an encapsulated PSG layer, offering decreased parasitics as compared to silicon nitride.

In addition to improved yields due to reduced mask counts, the SAMPSON process flow carefully orders etching steps for further yield improvement. This is most obvious for membrane devices. In these layouts the most challenging etch step is performed at the beginning of the process sequence, leaving only the simple release hole etch as the end step. This particular ordering of etch steps has resulted in improved yields for our fabrication runs, allowing identification and rework of poorly defined or etched wafers early on in the process flow.

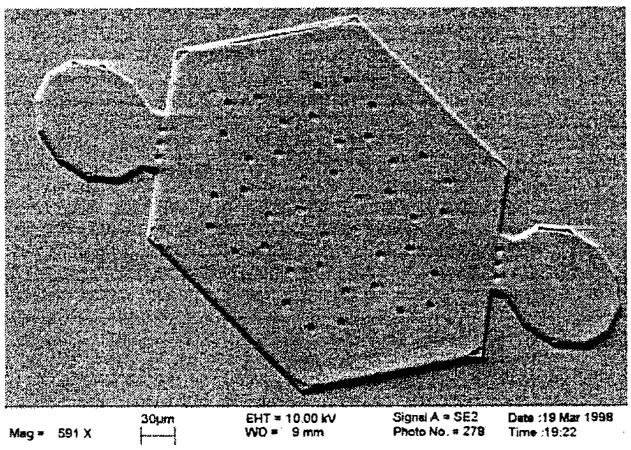

Figure 3: Electron micrograph of fabricated squeeze-film based SAMPSON resonant sensor.

RESULTS

In [3], a complex bulk micromachining approach was used to form a squeeze-film based vertical resonator, which was then characterized as a pressure sensor. In this work, the much simpler SAMPSON process is used to fabricate squeeze film based resonant pressure sensors (Figure 3).

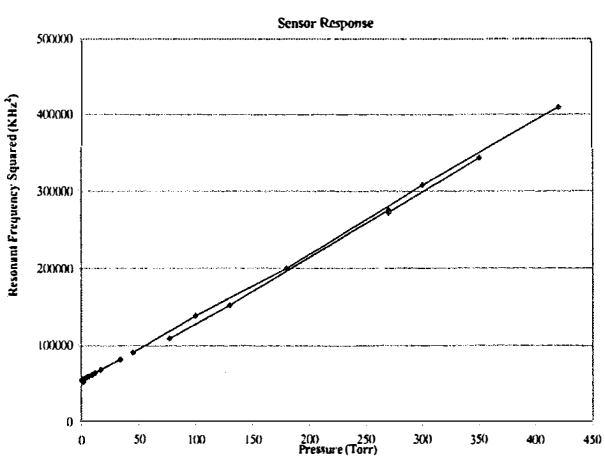

Figure 4: Measured resonant pressure sensor response.

Compared to the bulk micromachined approach [3], the SAMPSON process offers decreased resonator plate mass and interplate spacing. Decreases in these values result in increased squeeze numbers, increasing the sensor dynamic range. *Figure 4* shows the measured frequency^2 vs pressure response for a fabricated pressure sensor with a 1µm gap. As the figure shows, agreement with the high squeeze number response is excellent.

CONCLUSION

We have introduced the SAMPSON fabrication sequence, a reduced mask count surface micromachining process. The SAMPSON process offers decreased development time, and reduced parasitic capacitances over conventional processes.

A burst-proof squeeze-film based resonant pressure sensor was fabricated using this fabrication technique. The sensor resonant frequency exhibited a 3x change for air pressure ranges from vacuum to 450torr.

REFERENCES

1 W.C Tang, T.-C. Nguyen, and R.T. Howe, "Laterally driven polysilicon resonant microstructures," IEEE Micro Electromechanical Systems Workshop, Salt Lake City, Feb 20-22, 1989, 53-59.

2 W.P. Eaton, J.H. Smith, "Micromachined pressure sensors: review and recent developments," Proceedings of SPIE, vol 3046, March 4-6, 1997, 30-41.

3 M. Andrews, I. Harris, G. Turner, "A comparison of squeeze-film theory with measurements on a microstructure," Sensors and Actuators A, 36 (1993), 79-87.

SLED CARRIERS AND MOLDED THREE-SURFACE TIPS FOR ATOMIC FORCE MICROSCOPE CANTILEVERS

R. P. Ried, H. J. Mamin, D. Rugar
IBM Research Division, Almaden Research Center
San Jose, CA 95120

ABSTRACT

Novel sleds with silicon nitride atomic force microscope (AFM) cantilevers have been fabricated for an experimental AFM data storage system. The dimpled sleds slide over a surface and limit the maximum loading force on the AFM tip, thus allowing reduced constraints on the external loading system. Readback from a patterned rotating disk has been demonstrated using an AFM cantilever on a sled. Novel molded three-surface tips have been included on the cantilevers. The molded three-surface tips are expected to be more consistently sharp than conventional molded pyramidal tips.

INTRODUCTION

We have been investigating compact, high-density data storage using topographic readback by an AFM; conceptually the scheme may be likened to a tiny version of a phonograph with an AFM cantilever serving as a stylus **[1]**. Not surprisingly, maintaining a sharp AFM tip is a key issue. This paper addresses three aspects of the tip sharpness issue: improved loading force control, tip structure, and harder tip materials.

SLEDS

Air-bearing sliders are used to maintain gaps as low as 20 nm between a magnetic head and a spinning surface in magnetic disk drives. We wish to apply this air bearing technology to set the loading position of an AFM cantilever upon a surface, and thus improve upon the reliability and vibration immunity provided when a macroscopic actuator directly positions an AFM cantilever. Load control is particularly important for the AFM data storage application, where cantilever lengths of 10 µm or less are desired to achieve high data rates **[2]**. Since in previous work we have observed negligible wear of a polycarbonate data disk under an AFM tip with low loading pressure, we have made silicon nitride sleds - which slide in contact with a data disk - as a first step toward making air-bearing sliders with AFM cantilevers.

Figure 1 is a scanning-electron microscope (SEM) image of the underside of a 370 µm-long, 140 µm-wide sled formed from 0.7 µm-thick silicon nitride. The sled is connected to a glass support chip by two compliant, 390 µm-long silicon nitride tethers. The perimeter of the sled is covered with smooth corrugations that serve three functions: 1) stiffen the sled, 2) provide a smooth surface for the sled to ride over peaks of a patterned medium, 3) plow contaminating debris from the path of the oncoming AFM tip. An "H" shaped AFM cantilever is in the center of the sled. The AFM tip is on the center bar of the "H". Ideally, the AFM tip should project slightly further out of plane than the corrugations so that when the sled is flat on a patterned medium, the AFM tip contacts the surface with a small applied loading force. Interdigitated fingers are located at the far end of the cantilever for interferometrically measuring cantilever deflection **[3]**. The sleds are fabricated in a similar way to the original silicon nitride AFM cantilevers **[4]**.

In operation, the glass support chip is canted roughly 6 degrees with respect a spinning patterned medium. The support chip is initially brought toward the medium, so that the far end of the sled contacts the medium, and then moved closer so that the tethers bend and the sled rides flat on the surface. Further reduction in the spacing between the support chip and medium results in an increased loading force on the corrugations, with no increase in the AFM tip loading force expected.

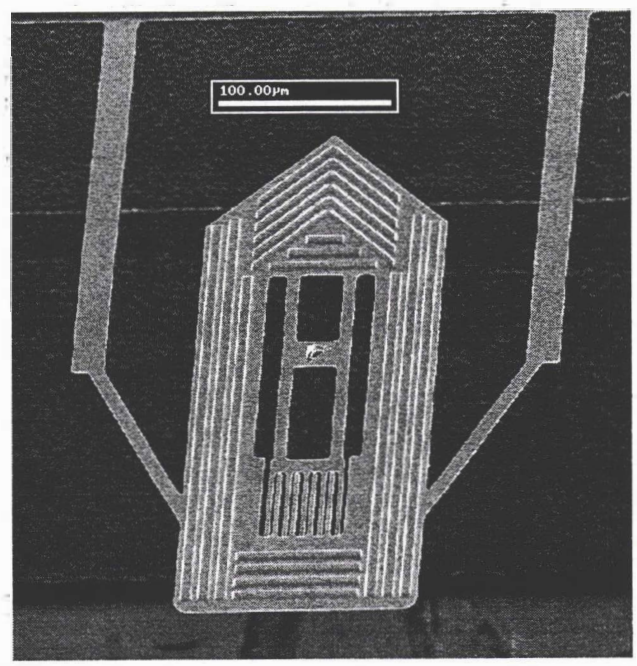

Figure 1. SEM image of corrugated sled with integral AFM cantilever and interdigitated fingers for interferometric readout. The sled is attached to a glass support chip via the tethers. The AFM tip projects beyond the corrugation depth in order to make contact when the sled is pressed flat on a data medium.

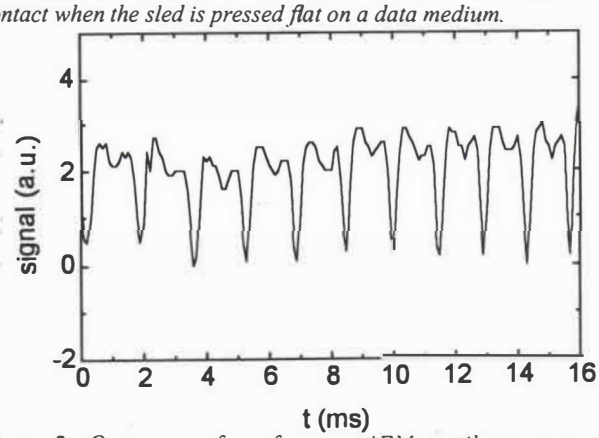

Figure 2. Output waveform from an AFM cantilever on a sled riding over 60 nm-deep, 0.5 µm-wide grooves with 5 to 9 µm-spacing on a spinning polycarbonate disk.

Figure 2 shows a waveform obtained by optical beam-deflection measurements from an AFM cantilever on a sled riding over 60 nm-deep, 0.5 µm-wide grooves with 5 to 9 µm-spacing on a spinning polycarbonate disk. Thus, proof of concept has been suc-

0-9640024-2-6/hh1998/$20©1998TRF
DOI 10.31438/trf.hh1998A.12

cessfully demonstrated. The varying base line in Fig. 2 is attributed to disk height variations and/or a spurious bending mode of the sled. Further testing to characterize the response is in progress.

MOLDED THREE-SURFACE TIPS

The four silicon {111} planes which are used to define a conventional molded AFM tip are prone to converge to a wedge rather than to a single point. The wedge shaped tip is duller than a perfect pyramidal tip. We have developed novel molded three-surface tips which converge toward a single point and which have a higher aspect ratio than the conventional pyramidal tip. Sharp, single-crystal-silicon tips defined by three planes were developed in previous work **[2]**.

Figure 3 outlines the process flow for forming a molded three-surface tip. In Fig. 3a, a high aspect-ratio trench with a curving mask shape is etched into a silicon (001) wafer, and then the trench is filled with silicon dioxide. Next, in Fig. 3b, the surface oxide is patterned as shown. In Fig. 3c, a wet anisotropic silicon etch is performed to leave two {111} planes meeting at the vertical oxide sidewall of the trench to form a tip mold. Subsequently, the mold is filled with a material such as silicon nitride, cantilevers are patterned, and the silicon wafer and oxide trench are etched away.

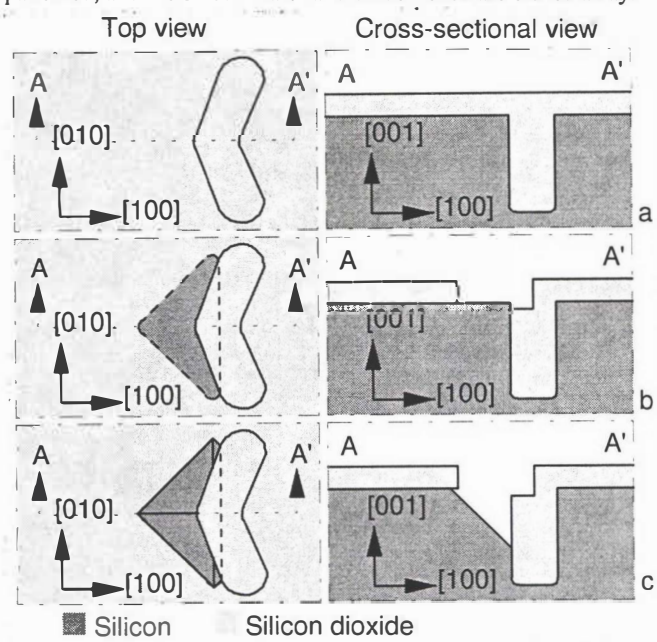

Figure 3. Fabrication of mold for three-surface tip. a) High aspect-ratio trench formation and filling trench with oxide. b) Pattern surface oxide. c) Wet anisotropic etch of silicon.

Figure 4 is an SEM image of the molded three-surface tip on the sled shown in Fig. 1. The measured tip radius of curvature is roughly 20 nm. We believe that that the tip was dulled by the finite etch rate of the silicon nitride in the long hydrofluoric acid etch used to remove the 3 μm-thick oxide trench. Tip sharpness could be improved with the use of a thinner oxide trench or a different tip material. Other possible tip variations include oxide sharpening of the mold **[5]**, and modifying the masking patterns so as to produce a pyramidal tip with a cylindrical hole in the center.

DIAMOND TIPS

Arrays of diamond tips have been successfully fabricated by

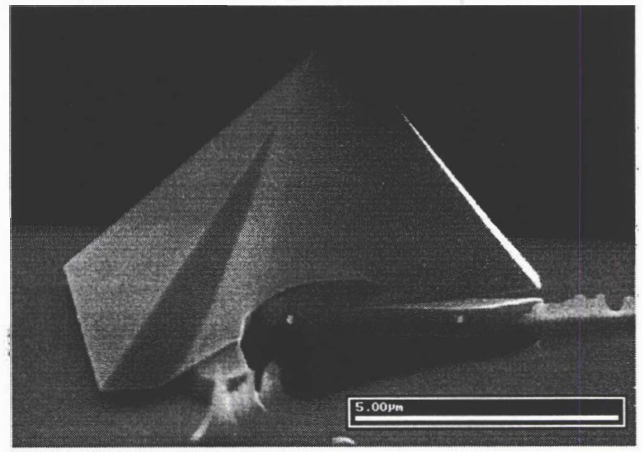

Figure 4. SEM image of molded three-surface tip from sled of Fig. 1. The vertical curving surface and one of the {111} planes which define the tip are visible. Two ancillary {111} planes are also visible on the structure. The shorter, high aspect-ratio ridges in the foreground arise from incomplete oxide filling of the trench.

depositing a 1 μm-thick layer of polycrystalline diamond **[6]** into pyramidal silicon molds and subsequently removing the silicon with tetramethyl ammonium hydroxide (TMAH). SEM measurements have shown that the radius of curvature of the tips are as low as 20 nm.

Future work may include integration of pyramidal and three-surface diamond tips onto cantilevers, sleds, and air-bearing sliders to investigate the increased durability of diamond tips for AFM data storage applications.

ACKNOWLEDGEMENTS

This work is supported in part by DARPA contract number DABT63-95-C-0019. Devices were partially fabricated at the Stanford Nanofabrication Facility.

References

1. H. J. Mamin, B. D. Terris, L. S. Fan, S. Hoen, R. C. Barrett, and D. Rugar, "High-density data storage using proximal probe techniques," *IBM J. Res. Dev.*, vol. 39, pp. 681-699, 1995.
2. R. P. Ried, H. J. Mamin, B. D. Terris, L. S. Fan, and D. Rugar, "6 MHz, 2 N/m piezoresistive cantilevers with INCISIVE tips," *IEEE J. Microelectromech. Syst.*, vol. 4, pp. 294-302, 1997.
3. S. R. Manalis, S. C. Minne, A. Atalar, and C. F. Quate, "Interdigital cantilevers for atomic force microscopy," *Appl. Phys. Lett.*, vol. 69, pp. 3944-3946, 1996.
4. T. R. Albrecht, S. Akamine, T. E. Carver, and C. F. Quate, "Microfabrication of cantilever styli for the atomic force microscope," *J. Vac. Sci. Technol. A*, vol. 8, pp. 3386-3396, 1990.
5. S. Akamine and C. F. Quate, "Low temperature thermal oxidation sharpening of microcast tips," *J. Vac. Sci. Technol. B*, vol. 10, pp. 2307-2310, 1992.
6. Films deposited at Crystallume Inc., Santa Clara, CA.

FABRICATION OF A MICRO TURBINE/BEARING RIG

Chuang-Chia Lin, Reza Ghodssi, Arturo A. Ayon, Dye-Zone Chen, Martin A. Schmidt
Microsystems Technology Laboratories and Gas Turbine Laboratory
Massachusetts Institute of Technology
Cambridge, MA 02139

ABSTRACT

This paper reports on an effort to build a 5-level wafer-bonded micro-machined rotary machine. The device has been successfully fabricated through the use of aligned bonding, deep silicon etching, and laser-assisted etching of silicon. The preliminary spin testing of the micro turbine has demonstrated continuous operation at 30000rpm.

INTRODUCTION

The first major fabrication challenge of realizing a miniature gas turbine generator is to demonstrate a baseline process capable of integrating the turbine rotor, bearings, and gas interconnects into a small package [1]. This structure, which we call the micro-bearing rig, not only validates a process methodology for fabrication of freely-rotating high aspect ratio devices, but it is also a vehicle for research into critical bearing stability issues. At MIT, we have developed a 5-wafer bonded device, which utilizes aligned wafer bonding, double-sided deep reactive ion etching (DRIE) by time-multiplexed deep silicon etching, and Laser-Assisted-Etching (LAE) (Fig.1). The device is composed of a center wafer which contains the free silicon rotor and a journal bearing, and is capped from above and below by two pairs of wafers which provide fluidic interconnect and serve as thrust bearing surfaces.

FABRICATION PROCESS

The process flow involves the use of 5 wafers, 16 masks, and 9 deep silicon etching steps. A schematic illustration of the process is shown in figure 2. The fabrication starts by etching shallow global alignment marks on both sides of all wafers. Next, two shallow patterns are etched to depths of 1 μm and 4.5 μm, which define a thrust bearing gap and blade clearance in a first wafer, called the Forward End Plate (FEP). This is followed by a deep silicon etch on the opposite side of the wafer to a depth of 350 μm. This deep etch process, first developed by Bosch, has been exhaustively characterized, and is reported elsewhere in this meeting [2]. Next, the FEP wafer is inverted, a lithography operation is performed, and the wafer is reversably attached to a second carrier wafer (using a resist bond) and deep etching is performed to etch through the wafer to the deep features on the front surface. This wafer is fusion bonded to a second wafer, called the rotor plate (RP), which has been etched to a depth of 200 μm to define turbine blades. Following a lithography operation on the RP to define a journal bearing, the RP/FEP pair is deep etched to fully define the rotor (using the reversable bond process described earlier). In principle, the rotor at this point is free, however, tabs have been created in the process of fabricating the FEP which bond to the rotor and hold it in place. These tabs will be removed by laser-assisted etching once the rotor is contained from above and below by the end plates. The process proceeds with the fabrication of an Aft End Plate (AEP), which is similar in process to the FEP, and a Forward Foundation Plate (FFP) and Aft Foundation Plate (AFP), which provide fluidic interconnect. The AEP and AFP are fusion bonded together, after which this pair is bonded to the RP/FEP pair, and then bonded to the FFP, completing the stack. (Fig.3) The 5-level stack is sawed into 1.5 cm^2 dies and immersed in diluted HF to remove any surface oxide that will prevent proper etching during LAE. A focused argon laser beam then heats the tabs that held the rotor to near melting point in a chlorine flowing chamber. The heated silicon volume reacts with chlorine to form volatile silicon tetrachloride that is carried away by the flow. [3] The rotor is freed once the tabs are completely removed, and this concludes the micro bearing rig fabrication process.

RESULTS

In order for the rotor to reach the design speed, it is critical to keep the rotor lubricated by a continuous fluid film. This is accomplished by a set of bearings - a pair of hydrostatic thrust bearings keeps the rotor centered axially, and a journal bearing provides lateral supports to prevent wall strikes. [4] In start-up, the thrust bearings are pressurized so that the rotor is floating axially, then the main turbine air is supplied to turn the turbine rotor. Preliminary test results show a continuous operation at speed of about 30000rpm. (Fig 4) Fluctuations in rotor speed are observed, and we are currently investigating the origins of this effect, as well as exploring means to stablly increase the rotor speed.

CONCLUSIONS

In this paper we demonstrated a process to fabricate a micro bearing rig using bonding and deep silicon etching. The process can be applied to many areas to build devices with complicated micro fluid interconnects. The micro rotary machinery will also open new opportunities for fabricating micro valves, pumps, micro coolers, and micro propulsion devices.

ACKNOWLEDGEMENT

The authors would like to thank U.S. Army Research Office (Dr. R. Paur) for sponsoring this project. Gratitude also goes to the whole microengine team at MIT.

REFERENCES

1. A. H. Epstein, S.D. Senturia, et. al. "Power MEMS and Microengines", *IEEE Transducer 97.*

2. A. A. Ayon, C.-C. Lin, R. A. Braff, R. Bayt, H.H. Sawin and M. A. Schmidt, "Etching Characteristics and Profile Control in a Time Multiplexed Inductively Coupled Plasma Etcher", *1998 Solid-State Sensor and Actuator Workshop.*

3. T. Bloomstein, "Laser Microchemical Etching of Silicon" *Ph.D. Thesis, MIT (1996).*

4. E.S. Piekos, D. J. Orr, S.A. Jacobson, F.F. Ehrich, and K.S. Breuer, "Design and Analysis of Microfabricated High Speed Gas Journal Bearings", *28th AIAA Fluid Dynamics Conference, June 29-July 2, 1997.*

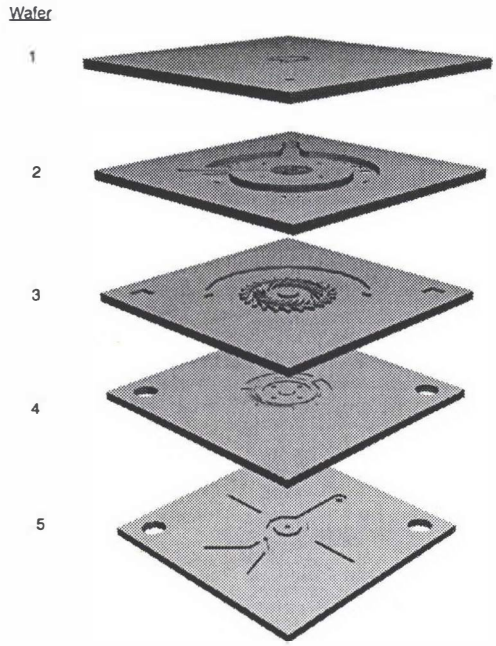

Figure 1 Exploded view of the micro bearing rig. The five layers are: 1. Forward foundation plate (FFP), 2. Forward endplate (FEP), 3. Rotor plate (RP), 4. Aft endplate (AEP), and 5. Aft foundation plate (AEP).

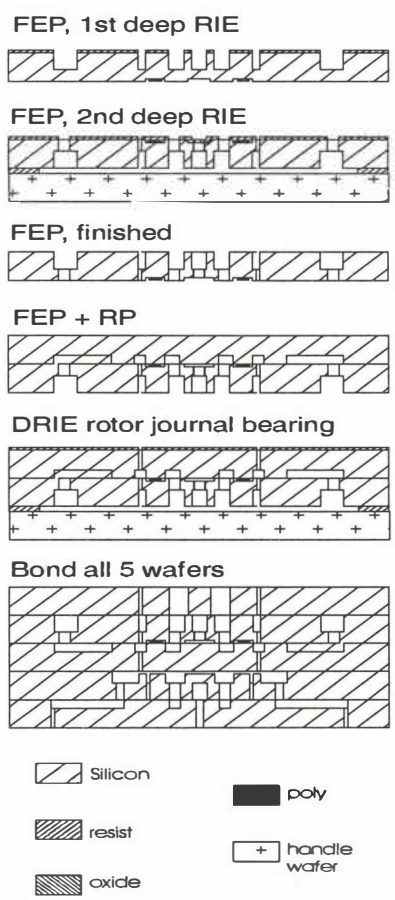

Figure 2 Micro Bearing Rig Fabrication Process

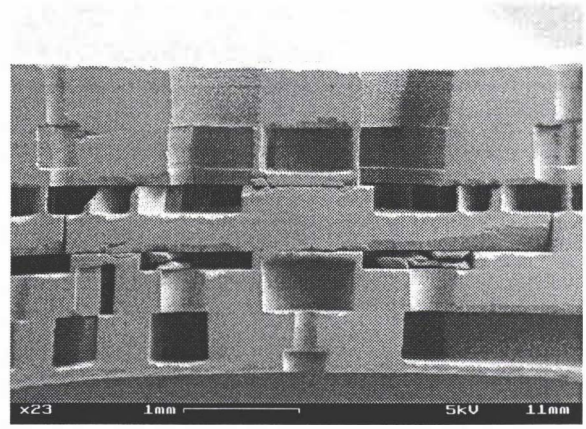

(a)

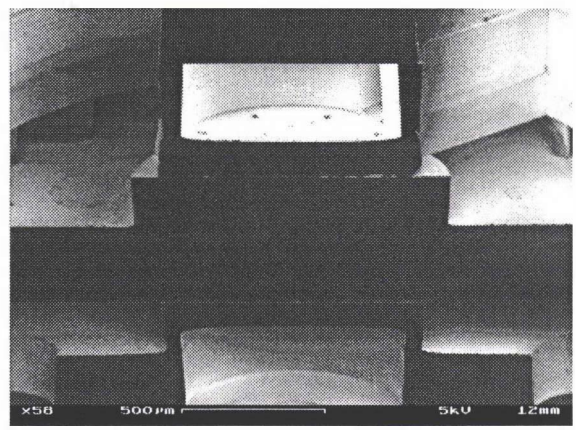

(b)

Figure 3 (a) SEM of micro bearing rig cross section.
(b) Close view of micro rotor thrust bearings.

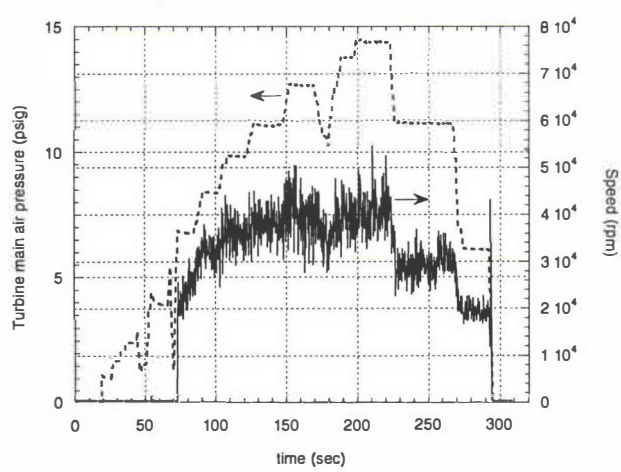

Figure 4 Rotor spin test result showing rotor speed increases with turbine main flow pressure.

A SILICON MICROMACHINED GATE VALVE

M. Walters, V. Dhuler, R. Mahadevan, A. Cowen, R. Wood, E. Hill
MCNC
PO Box 12889
Research Triangle Park, NC 27709

I. Kao
Dept. of Mechanical Engineering
State University of New York at Stoneybrook
Stony Brook, NY 11794

ABSTRACT

A novel silicon based microvalve that incorporates a simple gate valve design is described. The design, fabrication, and operation of the valve are discussed. Experimental results are presented which show that silicon die of 4mmx4mm dimension that contain these valves are capable of controlling air flows in excess of 5000sccm with a momentary input power of less than 1 watt.

INTRODUCTION

Silicon microvalve technology has advanced over the past decade and is now competing with conventional solenoid valves in the commercial marketplace[1]. Current silicon microvalve technology incorporates multi-wafer stacks that utilize vertical displacement of a boss structure to open or close a valve orifice[1]. The maximum flow rate through these valves is limited by the amount of vertical displacement that can be obtained for a given actuation mechanism and bossed diaphragm size. For flow rates on the order of 1000 sccm, these valves typically employ bossed diaphragms approaching 1cm in width, and can consume on the order of 1 watt of continuous power.[1,2] This work presents an entirely new silicon microvalve based on a single wafer system comprised of a linearly actuated gate valve design. These gate valves can be designed to be normally open or normally closed, are capable of controlling higher gas flows while consuming less power, and are smaller and less expensive to manufacture than current silicon microvalves.

DESIGN AND FABRICATION

A cross-sectional representation of the gate valve design is shown in Fig. 1. Actuation of the valve gate is provided by MCNC's in-plane thermal actuator[3], which has been shown to provide low voltage displacements up to 60μm and forces up to 15mN. Fabrication of the valves was performed at MCNC. The sliding mechanism of the gate valve is comprised of electroplated nickel. Valve seats are formed from deposited polysilicon and nitride layers. Openings through the silicon substrate are fabricated using a combination of deep silicon reactive ion etching and KOH etching. Several designs were fabricated which incorporate a single actuator to close or open multiple openings for increased gas flow. Photographs of two of the fabricated designs are shown in Fig. 2 and 3. Supplying power to the actuator causes movement of the sliding gate mechanism. In the linear gate valve design (Fig. 2), the actuation distance supplies the full range of motion to completely traverse the 40μm wide openings, while in the rotary gate valve designs (Fig. 3), mechanical advantage is used to provide motion over 200μm wide openings. An electrostatic clamping force is used to hold the valve gate in place once it has been switched, and springs are utilized to return the valve gate to its normal position when the electrostatic force is removed. Thus, appreciable power is only consumed during the short amount of time it takes to switch the valve from its normal state.

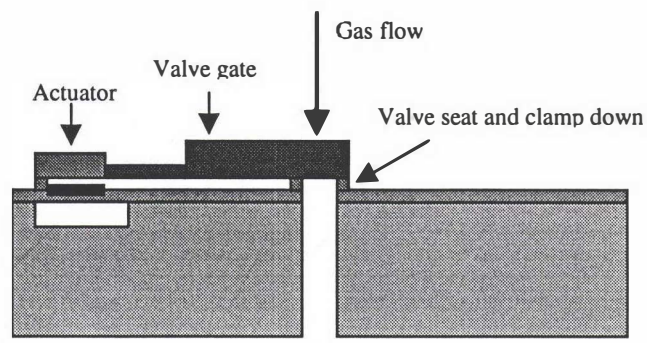

***Figure 1**: Schematic of a normally open gate valve design in the closed position. Power is supplied to the thermal actuator to move the valve gate. Once switched to the closed position, the power to the actuator is removed, and the valve gate is held in place using an electrostatic pull down voltage and the pressure from the gas flow. To switch back to the open position, the pull down voltage is removed and mechanical springs (not shown in schematic) are used to return the valve gate to its normal position*

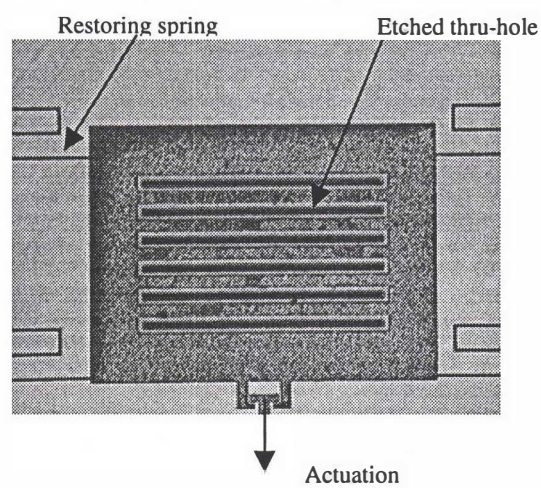

***Figure 2**: Fabricated normally open linear gate valve*

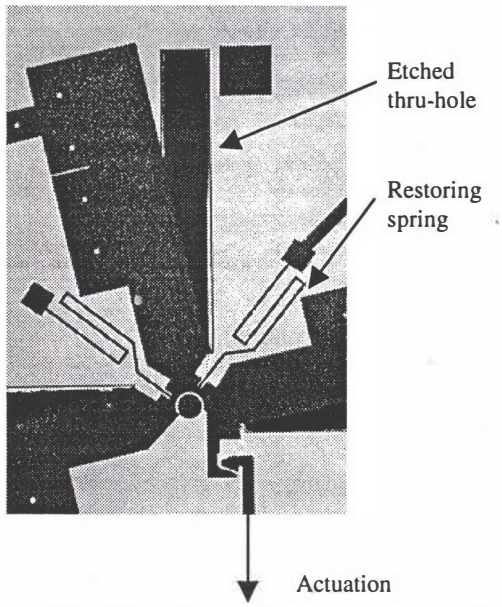

Figure 3: Fabricated normally open rotary gate valve

EXPERIMENTAL RESULTS

To facilitate flow testing, the valves were packaged in sealed T08 packages containing inlet and outlet ports available from T&E industries of Orange, New Jersey. Testing of the valves was conducted at SUNY-Stoneybrook. The inlet port was connected to a pressure regulated compressed air supply. A pressure gauge at the inlet port was used to determine the supply pressure. A flowmeter with a range of 0 to 5000 sccm was inserted at the outlet port. A power supply was used to provide the necessary current

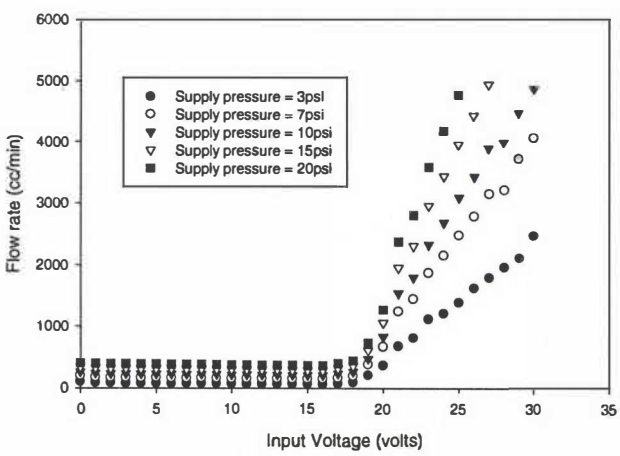

Figure 4: Measured flow rates as a function of input actuation voltage for a normally closed linear valve design (non-clamping).

and voltage for actuation and clamp down. Figure 4 shows a plot of the outlet flow rate versus applied voltage to the actuator for a normally closed linear valve design.

The data presented in Figure 4 is without a clamping voltage applied to the valve gate. The observed flow rates below 20V of applied actuation voltage represent the leakage flow rates without clamping down the valve gate. When the valve gate was clamped down, these leakage rates were too low to be measured. Over the operating voltage range of 20-30 volts, the input current was measured to be in the range of 27-30 mA, yielding an input power level for valve actuation of 0.5W to 1.1W.

The plot in figure 4 also shows that above an input actuation input of about 20V, the response of the valve is very linear, owing to the simple gate valve design. This linearity is further illustrated in figure 5, which shows a plot of the measured flow rates as a function if input pressure.

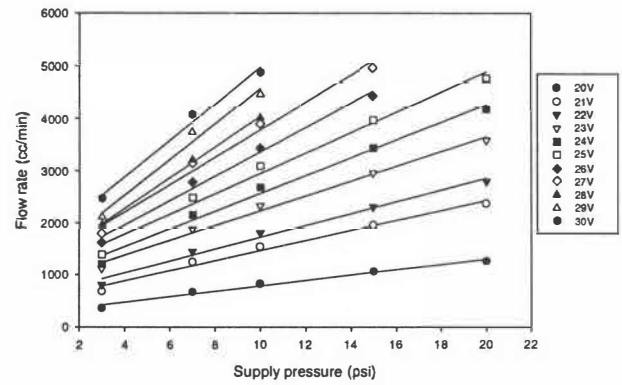

Figure 5: Measured flow rates as a function of supply pressure for a normally closed linear valve design).

SUMMARY

Table 1 summarizes the performance results obtained to date on the microvalve design presented in this paper. Because of their simple design and small size requirements, these valves are potentially more economical to manufacture than current commercially available diaphragm-based microvalves.

Table 1: Performance summary of the silicon micromachined gate valve

Die size	4mm x 4mm
Input Power	0.5-1.1 Watt (to switch) < 20mW (static)
Response time	≈ 50msec
Max. Flow rate	> 5000sccm (at 10psi or higher)
Max. Supply pressure	> 20 psi

REFERENCES

[1] P.W. Barth, "Silicon Microvalves for Gas Flow Control", *Technical Digest of the 8th Int. Conf. On Solid-State Sensors and Actuators, and Eurosensors IX*, Stockholm, Sweden, 6/25-29,1995, pp 276-279.

[2] P.W. Barth, C.C. Beatty, L.A. Field, J.W. Baker, and G.B. Gordon, "A Robust Normally-Closed Silicon Microvalve", *Technical Digest of the 1994 Solid-State Sensor and Actuator Workshop*, Hilton Head Isl., SC, 6/13-16/94, Transducer Research Foundation, Cleveland (1994), pp. 248-250.

[3] MCNC Patent Pending

VELOCIMETRY FOR MEMS

J.G. Santiago[1], C.D. Meinhart[2], S.T. Wereley[2], D.J. Beebe[1], and R.J. Adrian[3]

[1]Department of Electrical and Computer Engineering
and Beckman Institute for Advanced Science and Technology
University of Illinois at Urbana-Champaign
Urbana, IL 61801

[2] Department of Mechanical & Environmental Engineering
University of California - Santa Barbara
Santa Barbara, CA 93117

[3]Department of Theoretical and Applied Mechanics
University of Illinois at Urbana-Champaign
Urbana, IL 61801

ABSTRACT

We have developed a micron-resolution particle image velocimetry (micro-PIV) system to measure instantaneous and ensemble-averaged flow fields in micron-scale fluidic devices. The system images 100-300 nm diameter seed particles and determines vector fields using a double-frame cross-correlation algorithm. Velocity fields have been measured with vector-to-vector distances of less than 3.5 microns. This diagnostic tool has achieved the highest velocity measurement resolution to date of an internal fluid flow.

INTRODUCTION

Significant progress has been made in the development of microfluidic devices based on micro-electromechanical system (MEMS) technologies, such as bioanalysis systems, flow sensors, and micro-valves [1-2]. Although the scientific community has witnessed a surge of miniaturization designs, relatively few studies have specifically addressed the physics related to scaling down engineering systems. Since the flow passages of many microfluidic devices have length scales of 1 - 100 microns, traditional flow diagnostic tools cannot be used. Most measurements in microfluidic devices have been limited to bulk properties of the flow. To address this need, we have developed a micron-resolution Particle Image Velocimetry (PIV) system to measure both instantaneous and ensemble-averaged velocity fields in microfluidic devices, with characteristic dimensions of 10 – 100 microns. Using this micro-PIV system, we have demonstrated velocity field measurements with 3.5 micron vector-to-vector spacings [3]. Vector spacings of 1 micron are achievable.

EXPERIMENTAL SETUP

Our system is designed specifically for measuring velocity fields in bioanalysis systems where low-light level imaging is critical. The acquisition system incorporates an epifluorescent microscope with a continuous illumination Mercury-arc lamp, 100 to 300 nm diameter flow-tracing fluorescent particles, and an intensified CCD camera. To use this system, prototype microfluidic devices must have optical access to the flow field for high numerical-aperture microscope lenses. We have fabricated microfluidic devices by bulk-micromachining [100] Silicon substrate (using a wet KOH etch) and then sealed the fluid microchannels with a 170 micron thick glass cover slips (see Figure 1). The microchannels are 70 micron wide and 35 micron deep and have the characteristic trapezoidal cross-section of anisotropic [100] etching (no corner compensation was used). The figure also shows a schematic of the microchannel regions we investigated.

RESULTS AND DISCUSSION

We have used our micro-PIV system to investigate the velocity field of microfluidic devices with characteristic dimensions as low as 10 microns. Figure 2 shows nearly-instantaneous vector fields obtained in the cross-pattern microchannel shown in Figure 1. These velocity fields were each obtained using two images (of 200 nm diameter particles) with a center-to-center temporal spacing of 12 ms and an exposure time of 2 ms. The Reynolds number of these flows (based on channel depth and bulk velocity) is 3×10^{-2}. The maximum flow velocity in both cases is approximately 1.8 mm s^{-1}. The axis values in Figure 2 correspond to the number of CCD pixels. The measurements clearly show the details of the velocity field to within a few microns of the wall. Note that measurement uncertainty due to Brownian motion and image noise is apparent in both images. However, this Brownian motion is uncorrelated in time and space (from particle-to-particle) and can therefore be substantially reduced by either ensemble averaging over several measurements (as discussed below) or by spatial averaging of the instantaneous flow fields.

Figure 3a shows a nearly-instantaneous vector field measurement of a 3×10^{-4} Reynolds number Hele-Shaw flow around roughly cylindrical obstruction. Most of the noise in this velocity field measurement is due to the influences of Brownian motion and image noise. Ensemble averaging eight measurements substantially reduces this unbiased noise and yields the velocity data shown in Figure 3b. The approaching mean velocity is 35 micron s^{-1} (at the midplane) from the lower left to the upper right. The interrogation spots of the PIV algorithm [4] were 32 x 32 pixels with a cross-correlation window offset of six pixels in both the horizontal and vertical directions. Each interrogation spot was overlapped by 50%, producing approximately 900 vectors over a 120 x 120 micron field. The spatial resolution is defined by the 6.9 x 6.9 x 1.5 micron interrogation volume (which corresponds to a 3.45 micron vector-to-vector).

CONCLUSIONS

A micro-PIV technique that can be used to measure velocity fields with vector-to-vector distances of less than 3.5 microns has been demonstrated. This technique combines fluorescence microscopy, intensified CCD imaging, and cross-correlation PIV and can be applied to the study of the flow physics of MEMS-based microfluidic devices. The spatial resolution and accuracy of our systems is ultimately limited by: (1) the diffraction-limited spatial resolution of the imaging system, (2) noise in the particle-image field, (3) the interaction of the fluid with the finite-sized seed particles, and (4) the stochastic influence of Brownian motion.

0-9640024-2-6/hh1998/$20©1998TRF
DOI 10.31438/trf.hh1998A.15

REFERENCES

1. J.P. Brody, P. Yager, R.E. Goldstein, R. H. Austin, "Biotechnology at low Reynolds numbers." *Biophys J.*, 71, 3430-3441, (1996).

2. P. Gravesen, J. Branebjerg, O.S. Jensen , "Microfluidics - A Review," *J. of Micromechanics and Microengineering* , (1993).

3. Santiago, J.G., S.T. Wereley, C.D. Meinhart, D.J. Beebe, and R.J. Adrian , "A Particle Image Velocimetry System for Microfluidics," in press, *Experiments in Fluids* (1997).

4. R. J. Adrian, "Particle-imaging techniques for experimental fluid mechanics." Annual Review of Fluid Mechanics, 23, 261-304 , (1991).

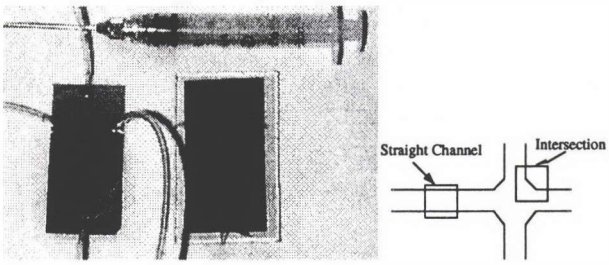

Figure 1. *To the left are two sealed cross-pattern microfluidic channels next to a 3 cc syringe. The channels are sealed with a 170 micron thick glass and an RTV adhesive. To the right is a schematic of two regions in the system that were analyzed using the micro-PIV technique.*

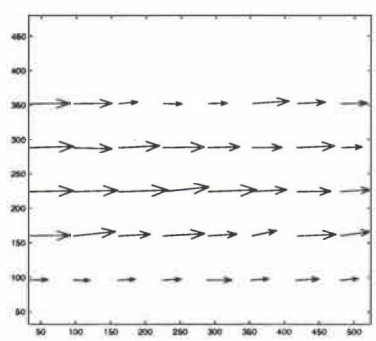

(a)

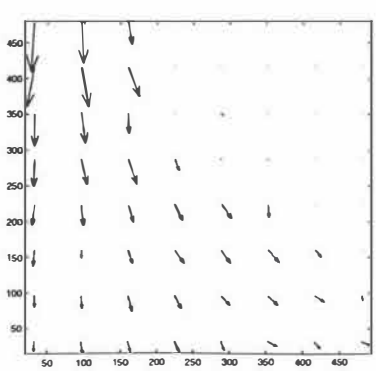

(b)

Figure 2. *Velocity field measurements obtained in one of the microfluidic systems shown in Figure 2. Each of these velocity fields were obtained from two particle images. Axis values are number of pixels with 0.23 micron/pixel. (a) Velocity field in a straight section of the cross-pattern microchannel system, (b) Velocity field in the microchannel intersection.*

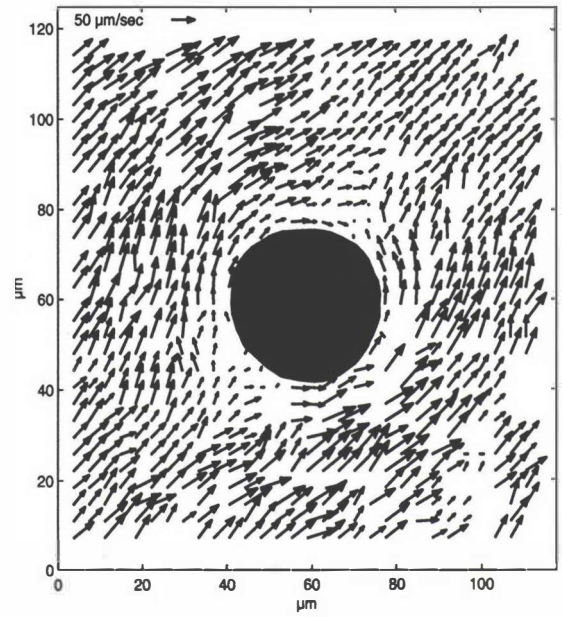

(a)

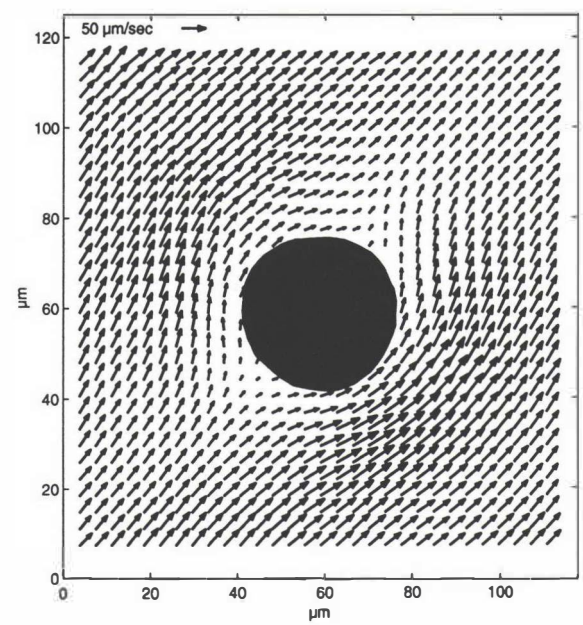

(b)

Figure 3. *Vector fields of a surface-tension driven Hele-Shaw flow around a 30 micron diameter obstacle. Each field contains approximately 900 velocity vectors covering a 120 x 120 micron field of view. Each velocity vector was measured with a 6.9 x 6.9 x 1.5 micron measurement volume: (a) Instantaneous vector field measurement, (b) Eight-image ensemble-averaged PIV velocity vector field.*

NUMERICAL INVESTIGATION OF PUMPING EFFECTS IN FPW-DEVICES

Nam Trung Nguyen*, Roger W. Doering and Richard M. White
Berkeley Sensor & Actuator Center, Department of Electrical Engineering and Computer Science
University of California Berkeley
Berkeley CA 94720

ABSTRACT

In this paper, we will present the numerical investigation of acoustically driven flow in micromachined flexural plate wave pumps using computational fluid dynamics (CFD). The simulation uses moving grids and moving wall models of a commercially available CFD tool (CFDRC Corporation). The simulation is carried out for a two-dimensional simple channel structure. The results will be discussed at the end of this paper.

INTRODUCTION

Recently there has been considerable interest on the use of flexural plate wave (FPW) devices for pumping fluid **[1,2]**. The pumping principle is based on the phenomenon of acoustic streaming in which high intensity acoustic fields cause the fluid flow. The acoustic field occurs near a surface on which flexural plate waves propagate. This pumping principle enables the realization of an "active" micro channel, which overcomes the high impedance problem encountered during the delivery of fluids through micro channels.

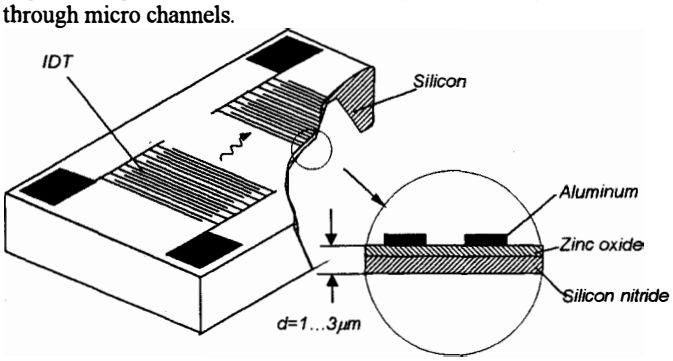

Figure 1. *Classical flexural plate wave device*

In our previous work **[3]**, an analytical theory was presented, which has demonstrated that acoustic streaming in the fluid is responsible for the pumping effect. Recently a numerical study of flow through wavy-walled channels that is similar to our case was reported **[4]**. However, this work only studied the first-order velocity field. Our paper presents the numerical results of time-averaged velocity field that causes acoustic streaming.

The numerical model is based on pumping water with a basic FPW-device shown in Fig. 1. The device consists of a rectangular flow channel that has a thin membrane on the bottom. The membrane is made of piezoelectric zinc oxide, aluminum, and low-stress silicon nitride. The typical thickness of the membrane measures from 1 to 3 microns. The flexural plate waves have a typical frequency of 3MHz and a wavelength of 100 microns. Interdigitated transducers (IDTs), that are arrays of finger pairs placed at wavelength intervals, generate the flexural plate waves.

FORMULATION OF THE NUMERICAL MODEL

Fig. 2 describes the two-dimensional model of the FPW-device. The channel model has a length of three wavelengths ($3\lambda = 300\mu m$). Wave amplitude and channel height are $10nm$ and $50\mu m$ respectively. The model contains a moving wall as the flexural surface, a rigid wall as the opposite surface and two cyclic boundaries as inlet and outlet. The cyclic boundary condition forces all variables (e. g., velocity, pressure) at the inlet and outlet to be equal. Fig. 2 shows how points on the device surface move elliptically in a counterclockwise direction as the flexural wave travels from left to right.

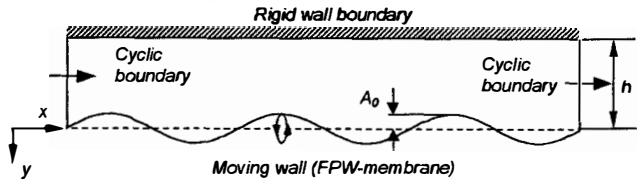

Figure 2. *Model of FPW-pump devices*

The vertical displacement Δy of the plate is given by:

$$\Delta y = A_0 \sin(\omega t - kx), \quad (1)$$

where A_0 is the wave amplitude, $\omega = 2\pi f$ is the angular frequency of the wave, and $k = 2\pi / \lambda$ is the wave number. With a membrane thickness d, the horizontal displacement is **[5]**:

$$\Delta x = (A_0 \pi d / \lambda)\cos(\omega t - kx). \quad (2)$$

Thus the ratio of the minor to the major axis of the ellipse is given by $\pi d / \lambda$. For instance, with the wavelength of $\lambda = 100\mu m$ and the membrane thickness of $d = 3\mu m$, the ratio of the minor to major axis of the elliptical motion will be 0.093.

From Eqs. (1) and (2) the velocity boundary conditions for the moving wall are:

$$u_w = d(\Delta x)/dt = -2\pi^2 (A_0 d f / \lambda)\sin(\omega t - kx) \quad (3)$$

$$v_w = d(\Delta y)/dt = 2\pi f A_0 \cos(\omega t - kx) \quad (4)$$

Since the CFD program implements both the moving wall and moving grid, there are two ways for building flexural plate wave boundary conditions: updating grid coordinates in the whole model or updating wall velocity components on the moving wall.

Using the first strategy, we assume that the computational grid moves elliptically. The grid position is updated for every time step using equations (1) and (2). For the second case we assume that the wave amplitude is much smaller than channel height h (several tens of nanometers versus several tens or hundreds of microns). The grids don't move; only the velocities of the moving wall are updated for every time step using Eqs. (3) and (4). The results presented in this paper were obtained with the first strategy.

A user library routine written in FORTRAN modifies the grid positions and velocity boundary conditions. Essential parameters of the model, and the current time and grid position, can be provided from pre-defined user constants and user routines of the software package. In order to make a realistic initial condition, the wave amplitude is described as a function of time:

$$A_0(t) = A_{\max}(1 - \exp(-t/\tau)) \quad (5)$$

For the results in this paper, we assume a time constant τ for water of one wave period $T = 1/f$. The simulation extends over more then 15 periods with 10 time steps each. The pressure field and the first-order velocity field of every time step are saved and used as the initial condition for the next time step. The time-averaged

* Poster presenter

0-9640024-2-6/hh1998/$20©1998TRF
DOI 10.31438/trf.hh1998A.16

velocity field can be than calculated and depicted by using MATLAB.

RESULTS

Fig. 4(a) illustrates the evolution of the pressure distribution in a one-wavelength portion of the channel over one time period. The mesh plot represents the pressure values of the last contour plot. Fig. 4(a) shows clearly that the acoustic field is evanescent with a decay length of about $20\mu m$.

Fig. 4(b) shows the time-dependent velocity field of the same region shown in Fig. 4(a). Using this field, the time-averaged velocity field shown in Fig. 4(c) can then be calculated. This field is responsible for the pumping effect. A shear viscous field penetration depth of about $5\mu m$ can be observed in Fig. 5. The maximum time-averaged velocity is 2.2 mm/s.

CONCLUSIONS

We have demonstrated the numerical simulation of the pumping effect in flexural plate wave devices using commercial CFD tools. However, the simulation is very time consuming. For a model with 3240 elements and 150 time steps (15 periods), the results presented in this paper took about 24 hours running on 200 MHz Pentium-PC with Windows NT. An optimization considering the number of grids, time step and time constant of the wave amplitude function could be done in order to get a faster simulation with acceptable accuracy. Most importantly the results reported in this paper show that the systematic design and optimization of acoustic micropumps is possible.

ACKNOWLEDGEMENTS

The authors would like to thank Dr. A. Lal of the University of Wisconsin-Madison and the staff of CFDRC Corporation for the initial work on this subject and their assistance.

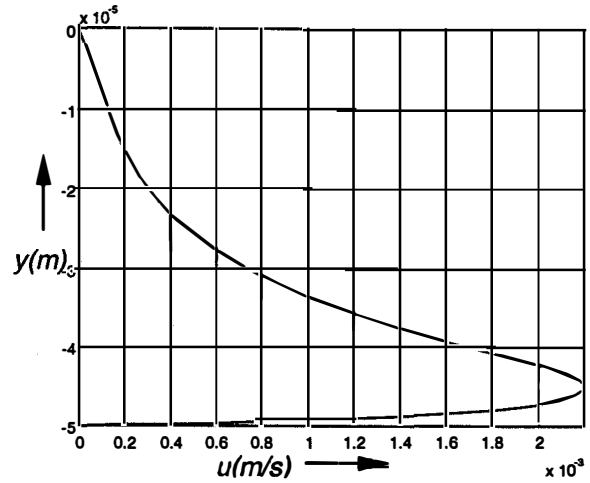

Figure 5. Profile of the time-averaged velocity over the channel height (velocity component in x-direction)

REFERENCES

1. R. M. Moroney, R. M. White, R. T. Howe, "Microtransport induced by ultrasonic Lamb waves", *Applied Physics Letters*, 59,7(1991), pp. 774-776.
2. P. Luginbuhl, S. D. Collins, G. A. Racine, M. A. Gre'tillat, N. F. de Rooij, K. G. Brooks and N. Setter, "Microfabricated Lamb wave device based on PZT sol-gel thin film for mechanical transport of solid particles and liquids", *Journal of Microelectromechanical Systems*, 6, 4(1997), pp. 337-346.
3. C. E. Bradley, R. M. White, "Acoustically driven flow in flexural plate wave devices: Theory and experiments" *Proc. IEEE Ultrasonics Symp.* (1994), pp. 593-597.
4. S. Selvarajan, E. G. Tulapurkara and Vasanta Ram, "A numerical study of flow through wavy-walled channels", *International Journal for Numerical Methods in Fluids*, 26(1998), pp. 519-531.
5. T. Sashida and T. Kenjio, "An instroduction to Ultrasonic Motors", Oxford: Clarendon Press, 1993, pp. 130.

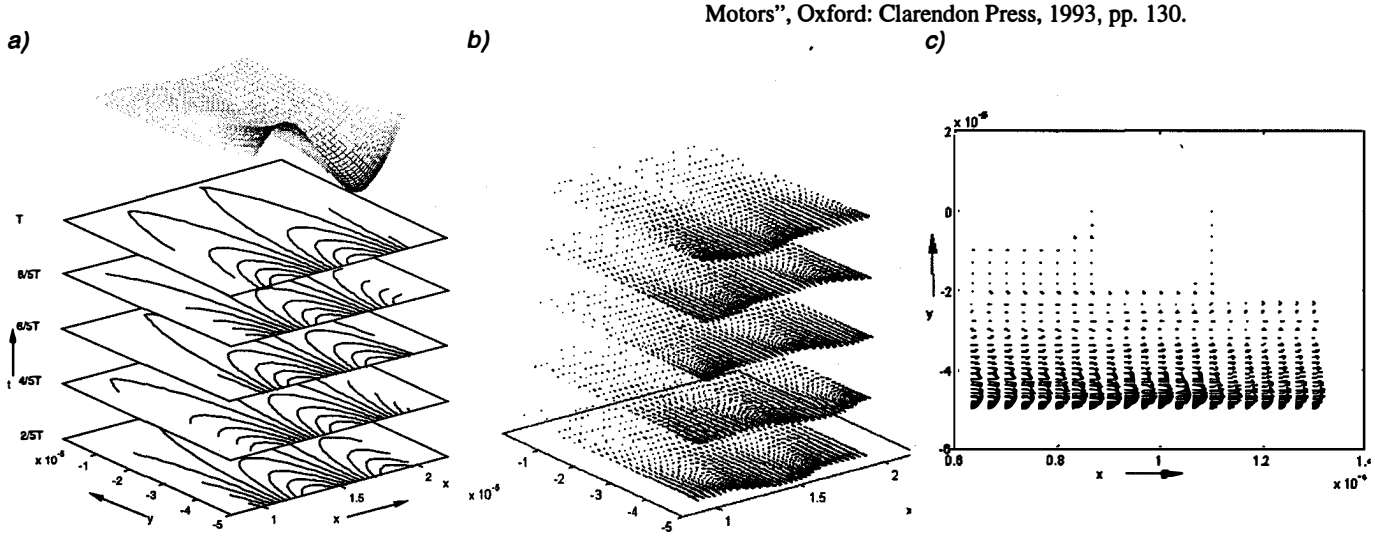

Figure 4. Simulation results for the micromachined FPW-pump. (a) The pressure fields over a time period T (propagation is in the x direction). (b) The velocity fields corresponding to the pressure fields shown in (a). (c) The time-averaged velocity field in the channel resulting from the time-dependent velocity fields in (b).

ELECTROCHEMICAL PRESSURE GENERATION

T. Stanczyk, B. Ilic, P.J. Hesketh, J. Boyd

Microfabrication Application Laboratory

Department of Electrical Engineering and Computer Science, University of Illinois at Chicago

Chicago, Il 60607

ABSTRACT

Electrochemical pressure generation between two platinum electrodes, and a reference Ag/AgCl electrode, has been investigated. The electrodes were immersed in a H_2SO_4/KCl solution and were subject to varying currents from a galvanostat. The desired reaction was O_2 production at the working electrode although several parasitic reactions came into play. These were divided into desired parasitic (production of H_2 at the counter electrode and the production of Cl_2 at the working electrode) and unwanted parasitic reactions (reduction of O_2 to H_2O at the counter electrode and oxidation of $H_2$to H^+ at the working electrode). The calculated values of the time to pressurize a cavity of 1.35 cm^3 (at varying currents and assuming O_2 production as the main reaction) to a value of 2000 Pa were compared to the experimental values. In each case, the experimental value was more then twice as fast as the calculated one. This is mainly due to the desired parasitic reactions that take place. At a current of 250 mA the time recorded to reach 2000 Pa was 0.6 seconds. The short amount of time to pressurize a chamber this size and the facts that relatively little power was consumed and that high pressure can be maintained with out extra power input, suggest that this mechanism of pressure generation would be good for precise liquid dispensing schemes.

INTRODUCTION

Electrochemical actuation is a relatively new way of creating large amounts of pressure based on electrolysis of an aqueous electrolyte solution. It has been previously investigated by Janchoa [1] and Kempe [2]. The electrolysis is driven by a potential that is applied to a working and a counter electrode. Depending on the metals used as the electrodes and the potential applied, gas can be generated at one or both of the electrodes. Neagu [3] has previously generated oxygen through the use of copper and platinum electrodes. Three-electrode systems also exist in which a potential is applied with respect to a reference electrode. The benefit of the three-electrode system is having a stable applied potential and knowing what reactions are taking place at that potential. In a closed system, pressure can be generated by gas formation and the reverse reactions can also be accomplished by shorting the electrodes or by switching the polarity. The reverse reactions depend upon the kinds of metals used for the electrodes and any other coating which may be used, such as Nafion [3], to limit negative ions and non-polar compounds from diffusing toward the electrodes. Otherwise, if pressure is generated and the applied voltage is cutoff, (ideally) the pressure would remain constant. Although this depends on a couple of factors: 1) how well the cavity is sealed and 2) any reverse reactions due to the standard reduction potentials. Depending on these variables, a pressure could be maintained for a long period of time with minimal power input.

THEORY

When a voltage greater than the equilibrium potential is applied between two electrodes, the production of gas is governed by the Faraday equation n = (It)/F, where n = the number of moles of gas, I = the current flow, t = the time of the applied voltage, and F = 96487 C/mol (Faraday's constant). At atmospheric pressure this gas will occupy a volume V given by V = n(RT)/P, where R = 8.314 J/mol/K, T = temperature in Kelvin, and P = pressure. From this one can calculate the time necessary to inflate a rigid chamber to a desired pressure given that this is the desired (half-cell) reaction:

$$2H_2O = O_2 + 2H^+ + 4e \qquad 1.229\ V$$

Although there are other parasitic reactions that happen:

Counter electrode	$2H^+ + 2e = H_2$	0.000 V
	$O_2 + 2H^+ + 4e = 2H_2O$	1.229 V
	$Pt + 4Cl^- = PtCl_4^{2-} + 2e$	0.730 V
Working electrode	$H_2 = 2H^+ + 2e$	0.000 V
	$2Cl^- = Cl_2 + 2e$	1.358 V

At the high potentials used there might be Platinum Chloride formation on the anode, which could impede gas formation. However, using two platinum electrodes has the advantage that the reduction potential between them is not a factor. Also, platinum is inert so that there is no oxide formation that can be a problem when other metals are used.

EXPERIMENTAL DETAILS

Figure 1 is the experimental layout used for our experiments. The electrochemical experiments were done inside of a teflon chamber that had 4 port connections. One port was used to connect the pressure sensor. The second port was used to insert the Ag/AgCl reference electrode. The third port was connected to a nitrogen tank. This was done in order to pressurize the chamber and measure the leakage rate (while no chemicals were present). The fourth port was where the platinum electrodes were inserted in order to seal the teflon cavity. The total volume of the teflon chamber was 1.73 cm^3. 0.35 cm^3 of the cavity was filled with the 9 part 0.1 M H_2SO_4/ 1 part 0.1M KCl solution. The KCl was present so that the Cl from the Ag/AgCl reference electrode would not dissolve into solution. The platinum electrodes that were used were made on [100] P-type silicon wafers. 2500 A of nitride was deposited and then 2000 A of platinum was sputtered at 110 W on the unpolished side of the

0-9640024-2-6/hh1998/$20©1998TRF
DOI 10.31438/trf.hh1998A.17

wafer. Subsequent to photolithography, Aqua Regia ($HCl + HNO_3$) was used to etch the platinum and then Piranha ($H_2SO_4 + H_2O_2$) was used to clean the platinum surface. The approximate size of each electrode that was exposed to the solution mixture was 4.0 mm^3 (the electrodes themselves are each 6.1 mm^3). The

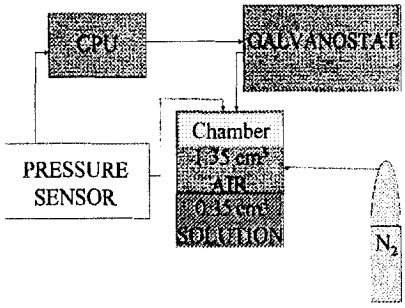

Figure 1. *Experimental Setup*

Ag/AgCl reference electrodes were made in the lab from 0.01" Ag wire. The specified potential of Ag/AgCl electrodes vs. NHE was –0.045 V although we repeatedly obtained a value of –0.068 V [4]. O-rings were also placed throughout the chamber in order to minimize leakage. When tested for this, the leakage rate was 1 Pa/s at moderate (2 to 5 kPa above atmosphere) pressures. The galvanostat was hooked up to the two platinum electrodes and to the Ag/AgCl reference electrode. Then different currents of 1mA, 10mA and 250 mA were applied to see the pressure generation rate. At 1 mA 2000 Pa was generated in 250 seconds. At 10 mA the same pressure was achieved in 19 seconds (Fig. 2). In both cases, the actual rate of gas production was more than twice as fast as the calculated values.

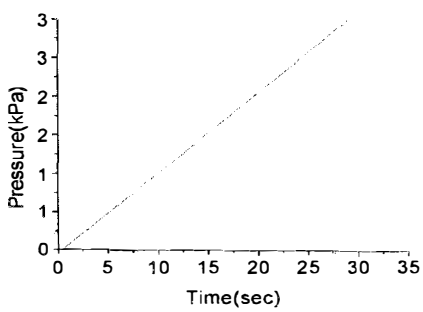

Figure 2. *At 10 mA, 2000 Pa was generated in 19 seconds. The calculated value, considering O_2 generation only, is 42.7 seconds.*

At a current of 250 mA the pressure rise was rapid and went above a value of 27,000 Pa in less than 50 seconds. It took only 0.6 seconds to generate a pressure of 2000 Pa at this rate (Fig 3). The rate in this run was also more then twice as fast as the calculated rate. We reasoned that this was from the generation of hydrogen and chlorine gas. This was confirmed when we took a voltammogram of our setup (Fig 4). The wave, which occurs at approximately 1.25 volts, is an indication of Cl_2 evolution.

CONCLUSIONS

The advantage of an electrochemical pressure generation is that once the pressure is built it should not change. This, however, is ideal and assumes no gas loss whether it is due to leakage through the chamber or due to reverse reactions. By two platinum electrodes in the three-electrode system we tried to minimize the reverse reactions and other retarding reactions. In the process we actually achieved faster pressure generation, 2000 Pa in 0.6 seconds, due to Cl_2 and H_2 generation in addition to the O_2 generation. However, there are still issues that have to be dealt with: 1) the sealing of the cavity, 2) reducing any oxygen and chloride reduction or hydrogen oxidation, and 3) reducing the formation of Platinum Chloride.

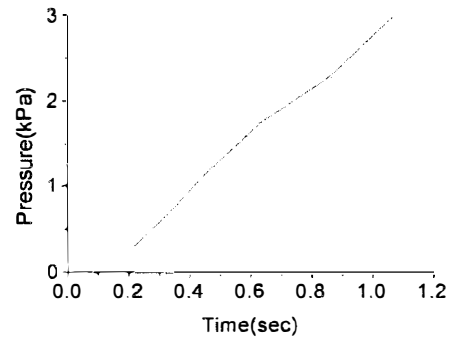

Figure 3. *At 250 mA a pressure of 2000 Pa was generated in 0.6 seconds*

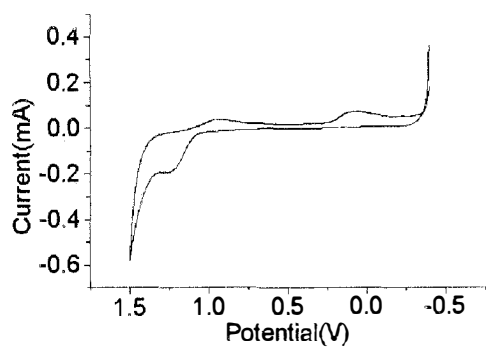

Figure 4. *A voltammogram done with between two platinum electrodes in a 9 part 0.1 M H_2SO_4 / 1 part 0.1 M KCl solution. Ag/AgCl reference electrode was used*

ACKNOWLEDGEMENTS

The authors would like to acknowledge and thank DARPA (grant # N66001-97-1-8911), for their financial support, and Tony Cocco, for his technical assistance.

REFERENCES

1. H. Janocha, "Neu aktoren", *Proc. Actuator,* 88, 389 (1988).

2. W. Kempe and W. Schapper, "Electrochemical actuators", *Proc. Actuator,* 90, 162 (1990).

3. C.R. Neagu, J.G.E. Gardiers, M. Elwenspoek, and J Kelly, "An electrochemical Microactuator: Principle and First Results", *Journal of Microelectromechanical Systems*, 5, 1 (1996).

4. A.E.G Cass, *Biosensors,* Oxford University Press, New York, 1990, pp. 60-61.

EXCESS ANALYTE DISPERSION GENERATED BY TURNS ON MICROCHIPS

Christopher T. Culbertson, Stephen C. Jacobson, and J. Michael Ramsey
Oak Ridge National Laboratory, P.O. Box 2008
Oak Ridge, TN 37831-6142

ABSTRACT

Introducing turns into the separation channel on a microchip device generally introduces an additional geometrical contribution to analyte dispersion. A simple, one-dimensional model has been developed which predicts the amount of excess dispersion introduced by turns in microchip channels. This model accounts for migration length differences, field strength differences, and transverse diffusion effects. The model describes the experimental data well.

INTRODUCTION

Microfluidic devices have been successfully demonstrated for a wide variety of separation techniques including capillary electrophoresis(CE), [1-3] synchronized cyclic electrophoresis(SCE),[4] free-flow electrophoresis, [5] and gel electrophoresis(GE).[6, 7] There has been a concerted effort to integrate these separation techniques with other physical manipulations and chemical reactions on monolithic microchip devices[8-12] as the advantages of combining sample processing and analysis in a single device are numerous. This increased level of integration, however, is reflected in a more complex channel manifold with a greater number of channels and interconnections. To maintain the overall small compact footprint of the microchip the channel manifold has to be carefully designed. Often these designs require that several turns be introduced into various channels, including the separation channel which in general has the greatest channel length requirements.[3]

Unfortunately, the introduction of turns into the separation channel also introduces a potential source of analyte dispersion.[3] This potential source of dispersion is introduced as a consequence of the differences in the arc length and field strength across the channel width in the turns (Figure 1A). As an analyte band traverses a turn, the individual molecules in the band will migrate different distances around the turn and feel different electric field strengths depending upon their respective positions across the width of the channel. This can result in an elongation of the band (Figure 1B). We have developed a model to describe the dispersion generated by a turn which accounts for the travel distance and the field strength differences experienced by molecules as they transit the turn and includes the effects of transverse diffusion. This model predicts that the variance introduced by a turn will be given by equation 1 below:

$$\sigma^2_{turn} = \frac{\left(2\theta w\left(1-exp\left(-t_D/t_t\right)\right)\right)^2}{24} \qquad (1)$$

where θ is the angle subtended by a turn, w is the channel width, t_D is the analyte transverse diffusion time, and t_t is the time that an analyte spends traversing the turn. The constant in the denominator is determined from the input response function which generated the variance.

Using this model the contribution of the geometrically generated dispersion to the total peak variance is examined as a function of the ratio of the transverse diffusion time to the analyte turn transit time (t_D/t_t).

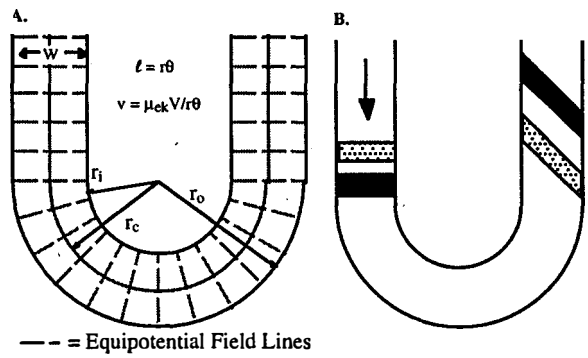

Figure 1. A. The distance (ℓ) that an analyte molecule travels around a turn and the field strength experienced in a turn depend upon the molecule's radial position. B. When the diffusion time across the channel is slow compared to the transit time around the turn (t_D/t_t large) then excess dispersion is introduced by the turn as the molecules situated along the inside of the turn move more quickly through the turn than those along the outside.

EXPERIMENTAL

Chip Design. The general design of the microchips used in this study can be found in Figure 2. They were fabricated from soda-lime glass slides using standard photolithographic, wet chemical etching, and cover plate bonding techniques.[3]

Apparatus. All experiments were performed using a single point, laser induced fluorescence (LIF) detection system similar to that previously described.[10] The 514nm laser line was focused through two cylindrical lenses to create an ellipsoidal excitation spot - the long axis of the ellipse being orthogonal to the channel axis. The fluorescence was collected using a 20x microscope objective and was focused onto a 150 μm wide air slit. This slit was long enough to sample the entire width of the separation channel. The signal passing through the slit was

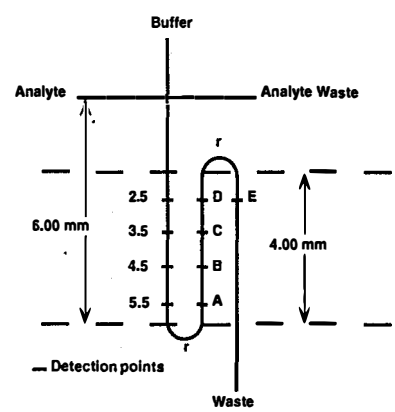

Figure 2. Schematic diagram of chip geometry.

0-9640024-2-6/hh1998/$20©1998TRF
DOI 10.31438/trf.hh1998A.18

Solid-State Sensors, Actuators, and Microsystems Workshop
Hilton Head Island, South Carolina, June 8-11, 1998

spectrally filtered using a bandpass filter (560df40; Omega). before being measured at a photomultiplier tube (PMT, Oriel #77340). The electrophoretic separations and injections were performed using four independent and remotely programmable high voltage (0-10 kV) power supplies (Ultravolt 10A12-P4). **Experimental protocol.** Electrophoretic injections of all analytes were performed in the pinched (constant volume) mode.[3] Each experimental sequence consisted of 2 or 3 replicate runs at several detection points (Figure 2). A plot of the peak variance versus migration time for one of these experimental sequences allows the quantitation of all of the major analyte band variance sources on the chip.

RESULTS AND DISCUSSION

To determine the robustness of the model developed above for predicting the magnitude of the geometrical dispersion introduced by turns, a wide range of t_D/t_t values were examined using a variety of chips and buffer conditions. A total of 37 experiments were performed. Each of these experiments consisted of approximately 30 electrophoretic runs. The actual variance introduced by the turn was determined using the equation below

$$\sigma^2_{turn,act} = \sigma^2_A - \sigma^2_{5.5mm} - 2*D*(t_A - t_{5.5mm}) \qquad (2)$$

where σ^2_A is the peak variance at detection point A after the first turn (see Figure 2), $\sigma^2_{5.5mm}$ is the peak variance at the 5.5 mm detection point just prior to the turn, D is the analyte diffusion coefficient, t_A is the migration time for the analyte at point A, and $t_{5.5mm}$ is the migration time of the analyte at the 5.5 mm detection point. The actual variances were then normalized using $(2\theta w)^2$ and plotted against the t_D/t_t ratio as shown in Figure 3. Eleven chips of varying channel widths

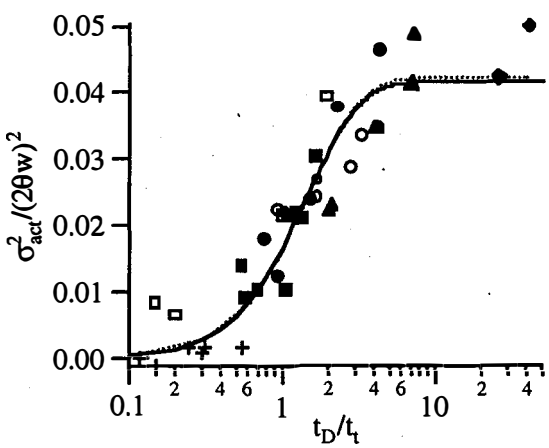

Figure 3. The effect of the t_D/t_t ratio on the excess dispersion introduced by a turn. The dotted line shows the best fit to the data. The solid line is that predicted by equation 1

and radii of curvature were used in collecting the data points shown. The channels on the chips ranged from 38 to 60 µm in width at the top of the channel. The turns on the chips had radii of curvature of 125 µm (▲, ◆), 250 µm (●,○), or 500 µm (■,□). The analytes and buffer systems consisted of Rhodamine B in a 50/50 (v/v) MeOH/20 mM NaBorate buffer (▲,●,■), TRITC-Arg in a 10 mM NaBorate buffer (○,□), and a restriction digest of ϕX174 in a gel filled capillary with a 0.5x TBE buffer (◆). The analyte velocities varied from 0.0051 cm/sec to 0.212 cm/sec. The results are consistent with the model.

ACKNOWLEDGMENTS

This research is sponsored by The Office of Research and Development, US Department of Energy, under contract DE-AC05-96OR22464 with Oak Ridge National Laboratory, managed by Lockheed Martin Energy Research Corporation. C.T.C. was supported through an appointment to the ORNL Postdoctoral Research Associates Program administered jointly by ORNL and the ORISE.

REFERENCES

1. Harrison, D.J., *et al.*, *Micromachining a Miniturized Capillary Electrophoresis-Based Chemical Analysis System on a Chip.* Science, 1993. **261**: p. 895-897.
2. Effenhauser, C.S., A. Manz, and H.M. Widmer, *Glass Chips for High-Speed Capillary Electrophoresis Separations with Submicrometer Plate Heights.* Analytical Chemistry, 1993. **65**(19): p. 2637-2642.
3. Jacobson, S.C., *et al.*, *Effects of Injection Schemes and Column Geometry on the Performance of Microchip Electrophoresis Devices.* Analytical Chemistry, 1994. **66**(7): p. 1107-1113.
4. Burggraf, N., *et al.*, *Synchronized Cyclic Capillary Electrophoresis - A Novel Approach to Ion Separations in Solution.* Journal of High Resolution Chromatography, 1993. **16**: p. 594-596.
5. Raymond, D.C., A. Manz, and H.M. Widmer, *Continuous Sample Pretreatment Using a Free-flow Electrophoresis Device Integrated onto a Silicon Chip.* Analytical Chemistry, 1994. **66**(18): p. 2858-2865.
6. Effenhauser, C.S., *et al.*, *High-Speed Separation of Antisense Oligonucleotides on a Micromachined Capillary Electrophoresis Device.* Analytical Chemistry, 1994. **66**(18): p. 2949-2953.
7. Woolley, A.T. and R.A. Mathies, Proceedings of the National Academy of Sciences USA, 1994. **91**: p. 11348.
8. Jacobson, S.C., *et al.*, *Precolumn Reactions with Electrophoretic Analysis Integrated on a Microchip.* Analytical Chemistry, 1994. **66**(23): p. 4127-4132.
9. Fluri, K., *et al.*, *Integrated Capillary Electrophoresis Devices with an Efficient Postcolumn Reactor in Planar Quartz and Glass Chips.* Analytical Chemistry, 1996. **68**(23): p. 4285-4290.
10. Jacobson, S.C. and J.M. Ramsey, *Integrated Microdevice for DNA Restriction Fragment Analysis.* Analytical Chemistry, 1996. **68**(5): p. 720-723.
11. Woolley, A.T., *et al.*, *Functional Integration of PCR Amplification and Capillary Electrophoresis in a Microfabricated DNA Analysis Device.* Analytical Chemistry, 1996. **68**(23): p. 4081-4086.
12. Waters, L.C., *et al.*, *Microchip Device for Cell Lysis, Multiplex PCR Amplification, and Electrophoretic Sizing.* Analytical Chemistry, 1998. **70**(1): p. 158-162.

A MICROFLUIDIC DEVICE COMBINING DIELECTROPHORESIS AND FIELD FLOW FRACTIONATION FOR PARTICLE AND CELL DISCRIMINATION

Peter Gascoyne, Xiaobo Wang and Jody Vykoukal
Section of Experimental Pathology, University of Texas M.D. Anderson Cancer Center
Houston, Texas 77030

Harold Ackler, Stefan Swierkowski and Peter Krulevitch
Electronics Engineering Technology Division, Lawrence Livermore National Laboratory
Livermore, CA

ABSTRACT

The technique of dielectrophoretic field flow fractionation (DEP/FFF) is described and a microfluidic device incorporating this principle is demonstrated. In operation, the device positions particles within a pressure-driven hydrodynamic flow profile by dielectrophoretic levitation according to their dielectric properties. Particles having different dielectric properties are differentially levitated and transported at different rates thereby separating them.

INTRODUCTION

The discrimination and separation of cells and other particulate matter is a central requirement if microfluidic devices are to reach their full potential in biomedical applications. One effect that can be readily exploited for particle manipulation and discrimination on the microscale is dielectrophoresis (DEP). This phenomenon arises when an applied electrical field induces electrical polarization in particles and spatial inhomogeneities in the field distribution act on this induced polarization to produce translational electrostatic forces. DEP is an appealing force for microscale applications because it depends only on the dielectric properties of the target particles and of their suspending medium. The required inhomogeneous electrical fields can be produced by easily fabricated electrodes and the electrical signals needed are of the order of only one volt. Furthermore, unlike electrophoresis, DEP utilizes high frequency AC electrical fields and electrolytic products are not a concern. Finally, through appropriate choice of the frequency of the applied field, frequency-dependent differences in the dielectric properties of particle subpopulations can be exploited for their sorting and separation from mixtures.

Here, a separation device is presented that utilizes hyperlayer field flow fractionation (FFF) in which particles are separated by being maintained by an applied force field at differential positions within a pressure-driven parabolic hydrodynamic flow profile. In our case, DEP and gravitational forces are balanced so as to accomplish this positioning. Different particle types emerge from the device at times that reflect their respective positions within the flow profile in accordance with their dielectric properties.

THEORY

A particle in a non-uniform, stationary AC electric field will experience a dielectrophoretic force

$$\langle F(t)\rangle = 2\pi\varepsilon_m\, r^3\, \mathrm{Re}(f_{CM})\nabla E^2(rms)$$

where the function $\nabla E^2(rms)$ describes the spatial inhomogeneity of the applied AC electrical field. The factor f_{CM} is the well-known Clausius-Mossotti factor

$$f_{CM}(\varepsilon_p^*, \varepsilon_m^*) = \frac{\varepsilon_p^* - \varepsilon_m^*}{\varepsilon_p^* + 2\varepsilon_m^*}$$

which describes the polarizability of the particle in terms of its complex dielectric permittivity ε_p^* and that of its suspending medium, ε_m^*. If the particle has a polarizability less than that of the suspending medium, the DEP force is negative, meaning that the particle is repelled from high field regions. Under these conditions and utilizing an electric field produced by an electrode array on the bottom wall of our device, a DEP levitation force is created on the particle. The particle therefore rises to the position where the DEP levitation force, which is height dependent, balances the gravitational sedimentation force. The equilibrium height is

$$h_{eq} = \frac{d}{2\pi}\ln\left\{\frac{3\varepsilon_m U^2 Ap}{2(\rho_c - \rho_m)g}\mathrm{Re}(f_{CM})\right\}$$

for a parallel electrode geometry, where U is the electrical potential applied to the electrode array, A is a geometrical term, p is the proportion of the applied field that is unscreened by electrode polarization, and $(\rho_c - \rho_m)g$ is the sedimentation force.

If the particle suspending fluid is flowing, a hydrodynamic flow profile will be present. Unless steps are taken to influence the profile, it will be parabolic in form and the fluid velocity at the height h_{eq} is given by

$$v_p = 6\langle v\rangle\frac{h_{eq}}{H}\left(1 - \frac{h_{eq}}{H}\right),$$

where H is the thickness of the chamber and $\langle v\rangle$ is the mean fluid velocity. Particles having different dielectric properties are levitated to different heights and therefore carried along at different rates by the flow profile. In this way, a mixture of particles becomes separated as it is carried through the chamber. This DEP/FFF principle is illustrated in Figure 1.

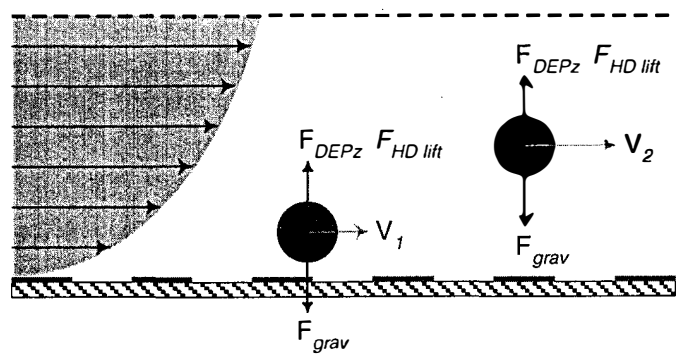

Figure 1. *Forces on particles during DEP/FFF separations. Particles having different dielectric properties are levitated by the DEP electrode to different equilibrium heights within the hydrodynamic flow profile (represented by the vectors on the blue area) and are carried through the chamber at different rates.*

0-9640024-2-6/hh1998/$20©1998TRF
DOI 10.31438/trf.hh1998A.19

TYPICAL RESULTS

Using polystyrene beads as test particles, the properties of DEP/FFF separators made with microelectrode arrays were characterized and the expressions given in the theoretical section were verified for frequencies of the applied electrical field at which electrode polarization effects could be ignored. Figure 2 shows the very clean fractionation that was obtained for two types of polystyrene beads having similar sizes and densities but different surface properties (non-functionalized *versus* carboxylated beads). Similarly clean discrimination was observed for other types of beads. Currently we are investigating beads activated to respond to target agents as well as undertaking cell discrimination experiments in diagnostic applications.

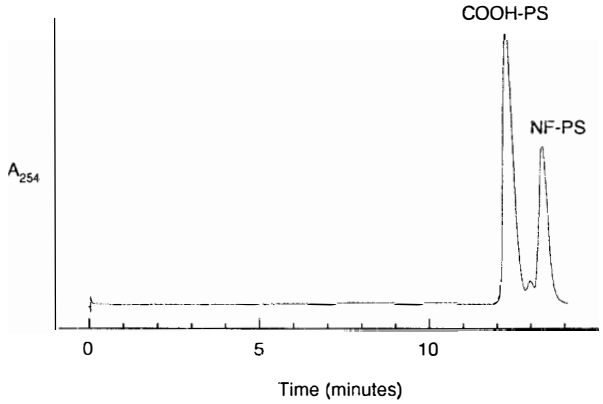

Figure 2. *DEP/FFF fractogram illustrating the separation of non-surface-functionalized polystyrene micro beads from similar micro beads having a carboxylated surface. A mixture of the two bead types was loaded near the inlet of the separation chamber, fluid flow was initiated, and beads leaving the exit port were detected with an ultraviolet sensor (by measuring the absorbance at 254 nm). The suspending medium was a sucrose/dextrose buffer of conductivity 10 mS/m and an applied voltage of 1.24 V RMS at a frequency of 50 kHz was used. While the two types of beads had similar sizes and densities, their different surface characteristics lent them distinguishable dielectric properties at 50 kHz.*

MICROFLUIDIC IMPLEMENTATION

The discriminating ability of a DEP/FFF separator depends on the length of the separation chamber. This demands that the chamber be made as long as practical. In the microfabricated implementation presented here, this length criterion is satisfied within a practical amount of real estate by utilizing a serpentine geometry for the separation channel. In this way a 100 mm channel occupies 3.5 cm^2. The serpentine configuration affords a secondary advantage in that the channel can be laid over a simple electrode array so that the channel passes over each electrode element several times. Devices were fabricated by bonding two borosilicate glass (Pyrex) substrates. A 200 micron deep separation channel was etched into one substrate using a wet isotropic etch. One mm holes were ultrasonically drilled through the outer substrate to provide inlet and outlet ports and electrical contacts. The electrode pattern was then etched from a sputter-deposited chrome/gold layer on this substrate using a mask of electrodeposited resist. Finally, the two substrates were bonded together to form the DEP/FFF separation chamber using a vacuum hot press at 267 psi and 600°C. A photograph of a two-separator version of such a device is shown in Figure 3.

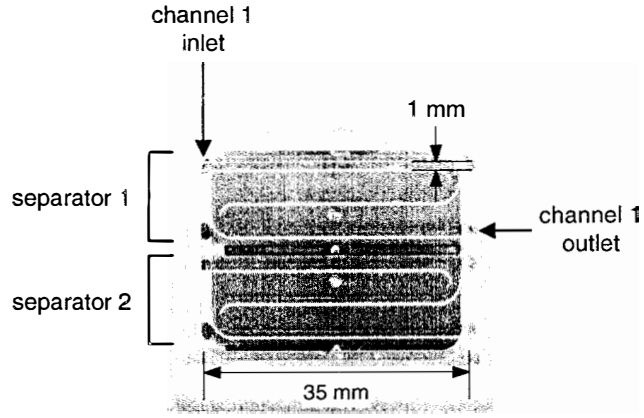

Figure 3. *Microfluidic implementation of a dual DEP/FFF separator device. Two separators are fabricated next to one another. Each of the separators has three straight segments and two turns. The device is shown from below within its test package. On separator 1, PEEK tubing (red) that brings fluids in and out of the ports on the top side is visible through the bonded glass body of the device. The darker area covering the separators is an electrode array consisting of two groups of 350 parallel gold elements 50 microns in width and having 50 micron spacing. These electrodes provide the dielectrophoretic levitation force by which particles are discriminated in the flow stream.*

CONCLUSIONS

The technique of dielectrophoresis combined with field flow fractionation has been described. The method is able to discriminate between beads having different surface functionalities and is being tested in detection and cellular diagnostic applications. The glass bonding method affords a straightforward approach to the fabrication of microfluidic devices utilizing this technique. DEP/FFF is an attractive microscale technology because it requires no moving parts except the fluids themselves, it uses AC fields that eliminate problems associated with electrolysis, and it does not require particles to touch any surfaces of the separation chamber.

REFERENCES

Gascoyne PRC, Y Huang, X Wang, J Yang, G De Gasperis and X-B Wang 1996 Cell separation by conventional dielectrophoresis combined with field-flow-fractionation *Biophys. J.* **70**: A333.

Huang Y, X-B Wang, F F Becker and PRC Gascoyne 1997 Introducing dielectrophoresis as a new force field for field-flow-fractionation *Biophys. J.* **73:** 1118-1129.

Markx GH, J Rousselet and R Pethig 1997 DEP-FFF: field-flow-frcationation using non-uniform electrical fields *J. Liq. Chrom & Rel. Technol.* **20:** 2857-2872.

Wang X-B, MP Hughes, Y Huang, F F Becker and PRC Gascoyne 1995 Non-uniform spatial distributions of both the magnitude and phase of AC electric fields determine dielectrophoretic forces *Biochim. Biophys. Acta* **1243:** 185-194.

ACKNOWLEDGEMENTS

This work was supported by the Defense Advanced Research Projects Agency under Contract N66001-97-C-8608 from the Space and Naval Warfare Systems Command. The microfabrication work was conducted under the auspices of the U.S. Dept. of Energy by Lawrence Livermore National Laboratory, contract number W-7405-ENG-48.

A FOREST WITHOUT TREES: DEVELOPMENT OF HIGH-SURFACE-AREA MATERIALS FOR ENHANCED-SENSITIVITY SAW ARRAY

W. Graham Yelton, Antonio J. Ricco, and Alan W. Staton
Microsensor R&D Dept., Sandia National Laboratories
Albuquerque, New Mexico 87185-1425

INTRODUCTION

Chemical sensor arrays are an alternative to the tedious development of highly specific single-analyte detectors [1]. Our recent efforts have focused on the chemical and physical diversity of interface materials for SAW sensor arrays [2]. However, the issues of wide dynamic range and high sensitivity must also be addressed for sensor arrays to compete in applications requiring low detection limits. Because SAW devices respond in proportion to change in mass per nominal unit area of the device surface, sensitivity is enhanced by surface modification with high-area, thin-film coating materials: a greater mass of analyte is adsorbed at a given ambient concentration.

We are exploring several classes of electrochemically prepared high-area films, materials whose formulations and processing are well documented [3] for applications other than chemical sensors. We present results from films formed by anodization, chemical conversion, and electroplating, yielding surface area enhancements as high as 170x.

EXPERIMENTAL RESULTS AND DISCUSSION

Figure 1 shows three high-area coating materials, each with a unique morphology. Figure 1a shows the leafy crystal morphology of copper oxide formed by chemical conversion of 400 nm of evaporated copper using potassium persulfate. Figure 1b reveals a highly dendritic coating of platinum "black," electroplated from chloroplatinic acid laced with lead acetate. Figure 1c is a porous Al_2O_3 film formed from an evaporated Al film under fixed DC potential in dilute phosphoric acid. Not shown but also studied were Al_2O_3 films formed by anodization in sulfuric and oxalic acids, as well as cathodically deposited "black" (high area) films of Pd, Au, Ni, and Cr [3].

To determine film surface areas, we recorded *in-situ* nitrogen adsorption isotherms at 77 K in a variant of the BET technique developed specifically to characterize thin films on SAW devices [4]. Figure 2 shows such an isotherm for a Pd black film, one of the materials with which we most consistently obtained high area enhancements. The area enhancements calculated from the N_2 isotherm, along with the mass/area of N_2 adsorbed at p/p_{sat} = 90%, are summarized in Table 1 for a number of films.

A factor limiting surface area enhancement is attenuation of the SAW by the high-area films. Thick, dense films attenuate the SAW, and feature sizes comparable to (or a significant fraction of) the 32 μm acoustic wavelength scatter the waves, causing further attenuation. In practice, coating feature sizes are typically much smaller than 32 μm (Figure 1), so film mass/area is the primary limitation. Thus, we achieved significantly better results (thicker usable films) with black Pd than with black Pt or Au, which have almost twice the density of Pd. Lower density materials such as black Cr should be better still, and the exceptionally low density of porous Al_2O_3 ought to be best. For these materials, however, we have had difficulty in producing high-area, open-pore structures with as much accessible surface area as the Pd black.

To evaluate the sensitivity and selectivity of the electrochemically formed films, we recorded adsorption isotherms from 18 analytes [1] over the 0.1 – 80% of p_{sat} range using arrays of 6 high-area film-coated SAW devices (devices and test system described in [1,2,4]). The *n*-propanol and *i*-octane isotherms of Figure 3 typify the response enhancement due to surface mass loading on the high-area coatings: the signal is 50 – 60 times larger for the copper oxide-coated device at p/p_{sat} = 50% than for the uncoated reference. Parameters found to influence the extent of enhancement include coating thickness and density, the potentials used to apply and process the films, and, importantly, details of the "seed" substrate layers upon which these films are formed.

Table 1. BET surface areas obtained from 77 K N_2 adsorption isotherms of electrochemically formed films on SAW devices.

Coating (thickness, nm)	Surface Area Enhancement	Max. N_2 (μg/cm^2)
Pd black	173	17
CuO conversion (1450)	50	4.6
Cr black	42	6.2
Pt black (390)	41	2.4
Au black (530)	22	1.5
Ni black	20	1.7
Al_2O_3 from $H_2C_2O_4$ (300)	19	2.8
Al_2O_3 from H_3PO_4 (210)	4.0	0.6
Al_2O_3 from H_2SO_4 (130)	3.7	9.2
Au seed layer (20)	2.8	5.5
Bare quartz	0.9	0.2

CONCLUSIONS

By enhancing SAW device surface area, detection limits can be improved by a factor of at least 100. We are using the chemical diversity of the high-area materials reported here, as well as further chemical modification of these films, to achieve the chemical diversity necessary to develop a multielement array of high-sensitivity SAW sensors.

Sandia is a multiprogram laboratory operated by Sandia Corporation, a Lockheed Martin Company, for the United States Department of Energy under Contract DE-AC04-94AL85000.

REFERENCES

1. A. J. Ricco *et al.*, "Dendrimer-Coated SAW Arrays for Volatile Organic Detection...", *Technical Digest of the 1998 Solid-State Sensor and Actuator Workshop*, Transducers Research Foundation, Cleveland (1998).
2. A. J. Ricco, G. C. Osbourn, and R. M. Crooks, "SAW Chemical Sensor Arrays: New Chemically Sensitive Interfaces...", *Accts. Chem. Res.*, *31*, xxxx (1998).
3. J. W. Dini, *Electrodeposition: The Materials Science of Coatings and Substrates*, Noyes, Park Ridge (1993).
4. A. J. Ricco, G. C. Frye, and S. J. Martin, "Determination of BET Surface Areas of Porous Thin Films Using Surface Acoustic Wave Devices," *Langmuir*, *5*, 273 (1989).

0-9640024-2-6/hh1998/$20©1998TRF
DOI 10.31438/trf.hh1998A.20

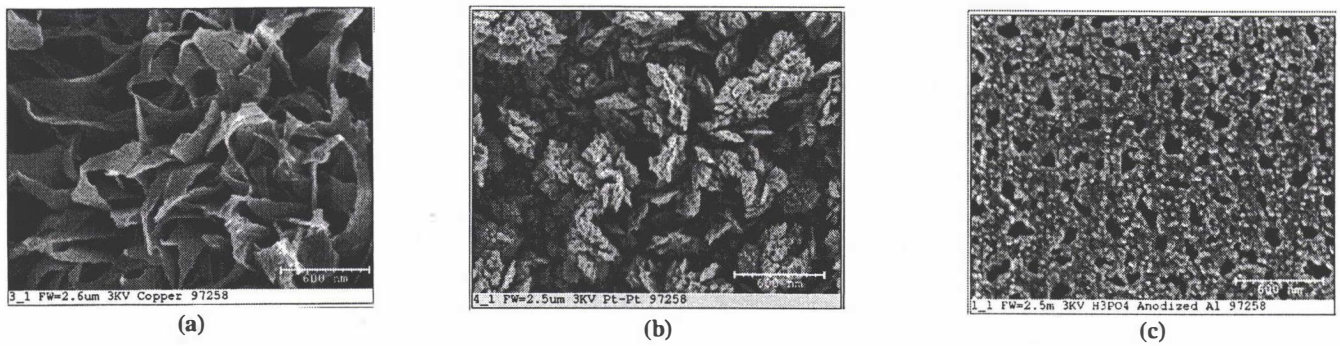

Figure 1. *Scanning electron micrographs of (a) copper oxide, (b) black Pt, and (c) anodized Al thin films. The scale bar at the lower right of each panel is 600 nm long; all three panels are shown at the same magnification.*

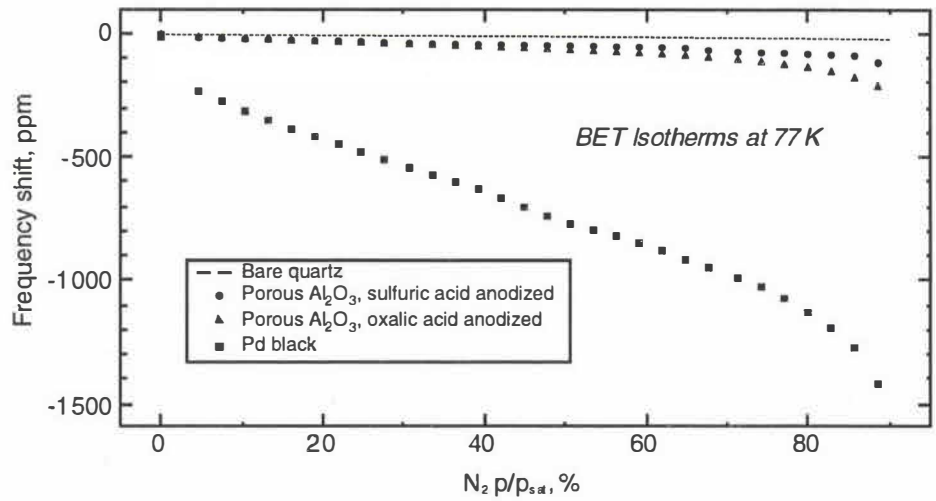

Figure 2. *SAW-measured N_2 adsorption isotherms at 77 K from one bare and three high-area film-coated SAW devices. A one ppm frequency shift is equivalent to a 97 Hz frequency change for these 97-MHz ST-quartz delay lines. Increased mass loading causes negative shifts in oscillation frequency.*

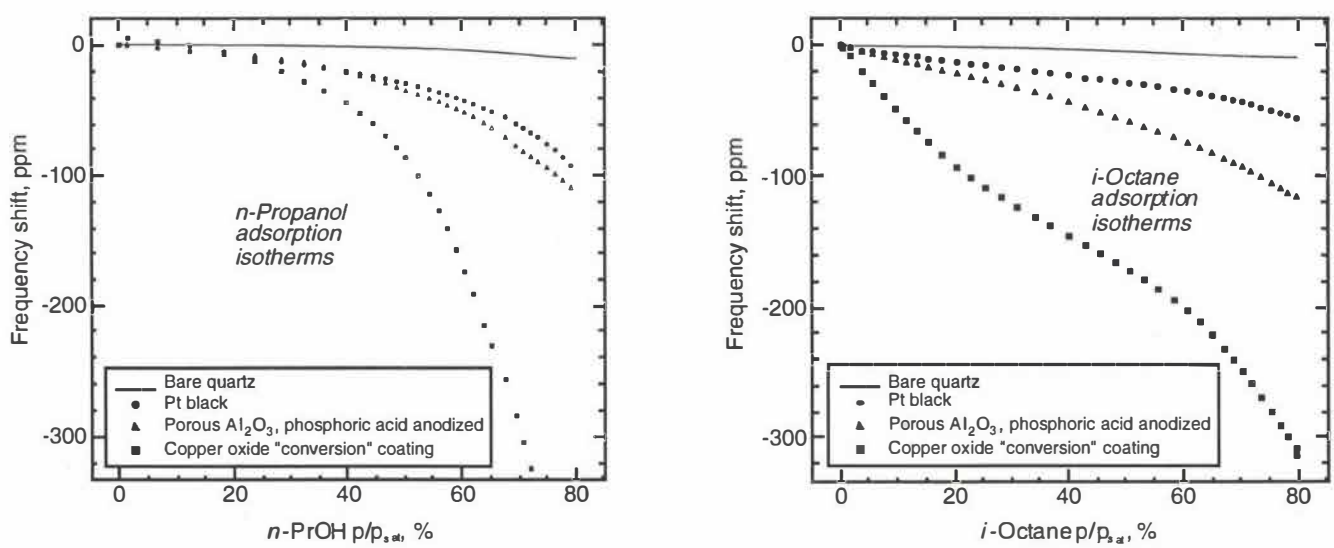

Figure 3. *Adsorption isotherms of n-propanol and isooctane on one bare and three high-area film-coated SAW devices.*

MOLECULAR RECOGNITION IN GAS SENSING: RESULTS FROM ACOUSTIC WAVE AND IN-SITU FTIR MEASUREMENTS

Andreas Hierlemann and Antonio J. Ricco
Microsensor Research & Development Department, Sandia National Laboratories
Albuquerque, New Mexico 87185-1425

Karl Bodenhöfer and Wolfgang Göpel
Institut für Physikalische und Theoretische Chemie, Universität Tübingen, Auf der Morgenstelle 8
72076 Tübingen, Germany

ABSTRACT

Surface acoustic wave (SAW) measurements were combined with direct, in-situ molecular spectroscopy to understand the interactions of surface-confined sensing films with gas-phase analytes. This was accomplished by collecting Fourier-transform infrared external-reflectance spectra (FTIR-ERS) on operating SAW devices during dosing of their specifically coated surfaces with key analytes.

INTRODUCTION

Molecular recognition is an important topic when searching for new, selective coating materials for chemical sensing. Recently, the general idea of molecular recognition in the gas phase was challenged by Grate *et al.* [1]. However, in earlier thickness-shear mode resonator (TSMR) investigations, convincing evidence was presented for specific recognition of particular analyte target molecules [2,3].

In this study, we systematically investigated coatings previously shown to be highly selective, such as the bucket-like cyclodextrins for chiral recognition [2], Ni-camphorates for the specific detection of the bases pyridine [3] and DMMP (dimethylmethylphosphonate), and phthalocyanines to specifically detect benzene, toluene, and xylene (BTX). In the case of the cyclodextrin (CD), oriented adsorption of the molecules within the CD torus (inclusion of the analyte molecule in the supramolecular cage) seems to control the recognition process; in the case of Ni-camphorate, it is probably coordinative ligand-metal donor bonding; for the phthalocyanines, it is likely "π-stacking", an intense interaction of the delocalized π electron systems of the phthalocyanine and the volatile aromatic compounds.

To further elucidate these interactions, we performed combined SAW/in-situ FTIR-ERS measurements. During each experiment, the film-coated SAW device, which simultaneously acts as a reflector for an IR beam at grazing incidence, is exposed to various volatile organics. From simultaneously recorded changes in the device frequency (principally due to mass changes) and changes in the IR signature of the volatile organic compound, one can reach fundamental conclusions about the coating/analyte interaction processes. Suitable control experiments, using "ordinary" organic polymers expected to show only simple physical interactions with the analytes, were conducted for comparison.

EXPERIMENTAL DETAILS

The coating materials chosen for this study (Fig. 1) were: a modified γ-cyclodextrin (3-*O*-butanoyl-2,6-di-*O*-*n*-pentyl-γ-cyclodextrin, CD) as cage compound; a nickel camphorate (Ni(II)-*bis*[(1R)-(+)-3-heptafluorobutanoyl-8-methylidencamphorate, Ni-cam) as coordinating agent; and a soluble nickel phthalocyanine (Ni-oktakis-*O*-pentyl-phthalocyanine, Ni-PC) as a material with a large, delocalized π-electron system. In addition, we used the reference polymers poly(etherurethane) (PEUT; Thermedics Inc., Woburn, MA) [2] and polyisobutylene (PIB, MW ≈ 380,000; Aldrich, Milwaukee, WI). The coatings on the SAW/FTIR-devices were prepared by spin casting or spray coating from methylene chloride solutions.

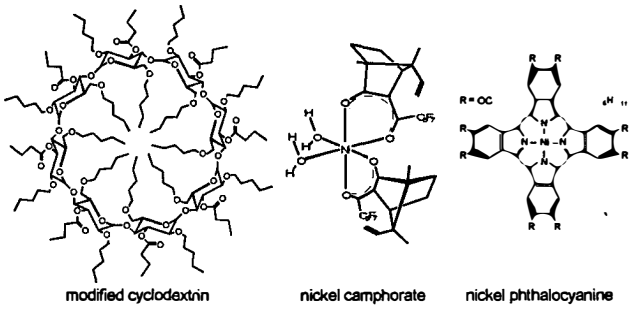

Figure 1. *Molecular recognition coating materials used in this study.*

The TSMR array consisted of discrete piezoelectric quartz crystals (AT-cut) with gold electrodes operating at a fundamental frequency of 30 MHz (plate thickness: 55.6 μm) purchased from Kristallverarbeitung Neckarbischofsheim, Germany [4].

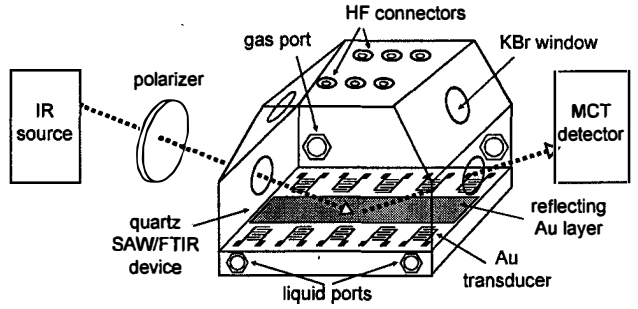

Figure 2. *Setup for simultaneous SAW/in-situ FTIR external reflectance measurements.*

SAW devices were custom designed at Sandia National Laboratories to provide a large gold reflection area for the FTIR measurements (Fig. 2). Five sets of independent interdigital Au transducers were defined on a 30 x 10 mm ST-quartz substrate; only the three center delay lines were used for measurements. The operating frequency of the devices was 97 MHz. SAW measurements were performed according to previously described procedures [5]. The SAW/FTIR devices were mounted in a custom gas-flow test cell (Fig. 2), which was attached to a gas manifold, using nitrogen as the carrier gas and bubblers for vaporizing the volatile organics.

FTIR measurements were performed using a Nicolet Magna-IR 750 spectrometer. Reflection spectra were obtained using a Harrick Scientific (Ossining, NY) Seagull accessory with an inci-

0-9640024-2-6/hh1998/$20©1998TRF
DOI 10.31438/trf.hh1998A.21

dent angle of 80° off normal. The orientation of the IR radiation (*s* or *p*) was selected by a wire-grid polarizer.

Volatile organics were used as received from Aldrich, Milwaukee, WI; the pure enantiomeric compounds were purchased from Fluka, Buchs, Switzerland.

RESULTS AND DISCUSSION

Our SAW/FTIR results support earlier conclusions derived from TSMR data **[2,3]**. In most cases where specific chemical interactions—metal coordination, cage compound formation, or pi-stacking—are expected, we record distinctive changes in the IR spectra, together with anomalously large SAW sensor responses, upon analyte dosing. In contrast, for standard physisorption processes (i.e., the "standard" polymers PEUT or PIB with various volatile organics), no changes in the IR spectra occur and the SAW responses are much smaller. In addition, the partition coefficients (or SAW sensor signals) roughly followed the fraction of saturation vapor pressure (variations do occur when comparing the nonpolar PIB to the polar PEUT).

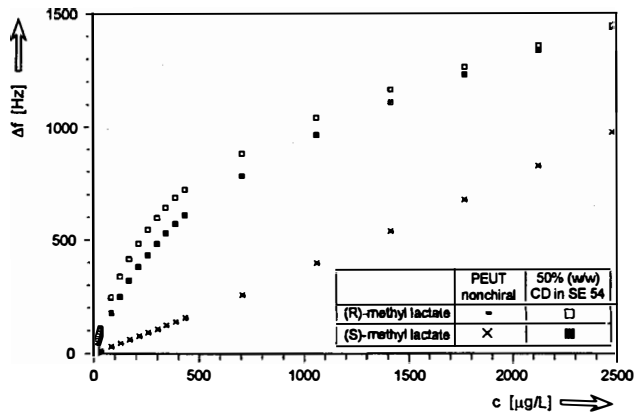

Figure 3. *Typical sensor responses representing preferential sorption (bent curves) and standard physisorption (straight line).*

Fig. 3 shows the response of a CD-coated TSMR upon exposure to methyl lactate over a wide concentration range. A curve typical of preferential sorption is shown: Langmuir-type behavior in the low concentration range gives way gradually to a linear physisorption curve, similar to that depicted for PEUT. Similar nonlinear sorption behavior at low analyte concentrations occurs for any of the investigated "molecular recognition" coatings with the corresponding specifically detectable molecules, including CD with methyl lactate; Ni-camphorate with pyridine or DMMP; and Ni-PC with aromatics like the BTX compounds.

Fig. 4 shows portions of the IR-spectra of methyl lactate recorded simultaneously with the SAW response. There are three main changes in the spectrum of methyl lactate sorbed into the CD in comparison to the reference spectra of the same compound in PEUT or PIB: (1) a new peak in the OH region at 3470 cm^{-1}; (2) a shoulder in the CO region at 1725 cm^{-1}; and (3) a new peak at 1190 cm^{-1}. The intensity of all these peaks for *s*-polarized light (not shown) is considerably lower than for the *p*-polarized light (Fig. 4), the latter having greater sensitivity to near-surface dipoles **[6]**. The intensity also varies somewhat between the *R* and *S* enantiomers, the changes in the *R*-methyl lactate spectrum being more pronounced than those in the spectrum of the *S* enantiomer, consistent with stronger sorption of the *R* enantiomer into the CD matrix as previously shown by GC and TSMR measurements **[3]**.

CONCLUSIONS

The method of simultaneous SAW/in-situ FTIR measurements is an effective, powerful tool for elucidating interactions between coatings and gaseous analytes, providing direct evidence for molecular recognition in acoustic wave gas sensors. Sandia is a multiprogram laboratory operated by Sandia Corporation, a Lockheed Martin Company, for the United States Department of Energy under Contract DE-AC04-94AL85000.

REFERENCES

1. J. W. Grate, S. J. Patrash, and M. Abraham, "Selective Vapor Sorption by Polymers and Cavitands on Acoustic Wave Sensors: Is This Molecular Recognition?", *Anal. Chem.*, *68*, 913 (1996).
2. A. Hierlemann, K. Bodenhöfer, M. Fluck, V. Schurig, and W. Göpel, "Selective detection of Nitrogen and Oxygen Containing Volatile Organic Compounds...", *Anal. Chim. Acta*, *346*, 327 (1997).
3. K. Bodenhöfer, A. Hierlemann, M. Juza, V. Schurig, W. Göpel, "Chiral Discrimination of Inhalation Anesthetics and Methyl Propionates by Thickness Shear Mode Resonators...", *Anal. Chem.*, *69*, 4017 (1997).
4. K. Bodenhöfer, A. Hierlemann, G. Noetzel, U. Weimar, and W. Göpel, "Performance of Mass-Sensitive Devices for Gas Sensing: Thickness Shear Mode and Surface Acoustic Wave Transducers", *Anal. Chem.*, *68*, 2210 (1996).
5. R. C. Thomas, H. C. Yang, C. R. DiRubio, A. J. Ricco, and R. M. Crooks, "Chemically Sensitive Surface Acoustic Wave Devices...", *Langmuir*, *12*, 726 (1996).
6. R. M. Crooks, L. Sun, C. Xu, S. L. Hill, and A. J. Ricco, "The Characterization of Organic Monolayers by FTIR-ERS", *Spectroscopy*, *8*, 28 (1993).

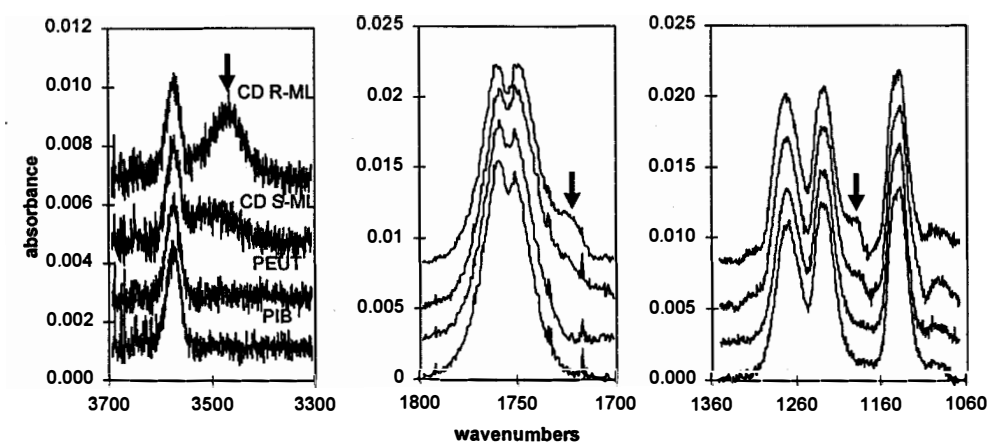

Figure 4. *IR reflectance spectra of both enantiomers of methyl lactate (R-ML and S-ML) on CD and the polymers PIB and PEUT.*

SOLVENT SENSOR ARRAYS FOR BINARY MIXTURES USING POLYMER-BASED CHEMIRESISTORS

S. V. Patel, M. W. Jenkins, R. C. Hughes, W. G. Yelton, A. J. Ricco, and S. A. Casalnuovo*
Microsensor R & D Department and *Advanced Semiconductor Technology Department
Sandia National Laboratories, Albuquerque, NM 87185

ABSTRACT

Low power, carbon-loaded polymer chemiresistors have been used to sense solvents over a wide range of solubility parameters. Polyethylene-vinylacetate (PEVA) and polyvinyl-alcohol (PVA) are two such polymers that have been used to sense binary mixtures of diisopropylmethylphosphonate (DIMP) and other solvents with water vapor at various temperatures. The VERI (Visual Empirical Region of Influence) technique is used as a method of pattern recognition to classify the solvents and distinguish them from water vapor. A method for the determination of solvent concentrations in a binary mixture of the solvent and relative humidity is presented.

INTRODUCTION

The development of a low-cost, low-power, "universal" solvent vapor sensing array requires several sensing elements that can sense a wide range of solvents. Analysis of the component elements is important to determine the best possible sensor or sensors for the classification and quantification of solvent vapor mixtures. Polymer-based chemiresistors have been used recently in the development of solvent sensor arrays.**[1,2]** Such an array would contain a minimum number of sensors capable of responding to the largest number of analytes possible. Therefore the array must contain chemically different sensor elements capable of responding to different analytes.

Such arrays have been used with surface acoustic wave (SAW) sensors**[3]**, where the solubility parameter (δ) is used to identify polymers best suited for sensing the solvents of interest. The polymer and solvent combination with similar solubility parameters result in the strongest interaction and, in turn, the largest response. Unfortunately, SAW devices require expensive and high frequency AC modulated electronics for operation. Arrays of this type also require a method of pattern recognition to analyze the responses of several devices to various solvents.

The VERI (Visual Empirical Region of Influence) pattern recognition method for solvent classification has been used to determine the best sensors for quantification of solvent mixture composition.**[4]** Once the minimum number of required devices are determined, the training set data are analyzed to determine the concentrations of solvent and relative humidity.

EXPERIMENTAL DETAILS

The polymer films used as chemiresistors were deposited on several different platforms. Detailed descriptions of the substrates are presented in reference **[1]**. The first type was the interdigitated electrodes on quartz substrates. These were fabricated at Sandia National Labs using photolithography to pattern gold electrodes with a chrome adhesion layer. The electrode spacing was 8 microns and the resistance was measured in a two-point probe configuration. On the same device a set of widely spaced electrodes was deposited to measure resistance of films that might have an uncharacteristically low resistance across the 8 micron spacing. A second type of platform consisted of platinum electrodes with a titanium adhesion layer, on an oxidized silicon wafer. The platinum electrodes were arranged in a four-point probe configuration, with two inner and two outer electrodes. The inner electrodes had either a 100 or 50 micron spacing. All the electrodes made contact to large pads for external electrical contact. These data are the first reported four-terminal measurements on this type of chemiresistor in which the bulk resistance can be separated from the contact resistance.

The carbon-loaded polymers were made by dissolution of both the polymer and a particular weight percent (e.g., 40 wt. % is designated by "-40-C") of carbon particles (20-30 nm diameter) in a solvent such as water or chlorobenzene. The polymers used were polyisobutylene (PIB), polydiphenoxyphosphazine (PDPP), polyethylene-vinylacetate (PEVA), polyvinylalcohol in two forms, 88% (PVA) and 75% (PVA75) hydroxylated. The carbon loading typically ranged from 25 to 40 wt. %.

Films were deposited on substrates by either spin casting or pipetting the dissolved material directly onto the substrate. The pipette method usually led to films that were thicker than the spin cast films. In some cases a 5 micron filter was used to enhance the dispersion of the carbon particles, which tended agglomerate and form shorts between the narrowly spaced electrodes.

The devices were placed in a specially designed test fixture, which had spring-loaded Pogo® pins to contact the pads on the substrates. The fixture was attached to a gas manifold that had the capability of mixing several gases as well as two solvent vapor streams using nitrogen as the carrier gas through bubblers. Eleven solvent vapors were tested with varying solubility parameters. A constant total flow rate of 1000 sccm was used for all experiments. The test fixture was placed in a constant temperature chamber which could be controlled to ± 0.1°C and heated to 60°C. For the carbon-loaded polymers, a digital multimeter (7.5 digit resolution) was used to measure the film resistance.

RESULTS AND DISCUSSION

The sensor films were exposed several times to solvent vapors individually as well as simultaneously with water vapor to challenge the array for the most common binary mixture encountered in the field. Fig. 1 shows the percent resistance change response of five polymer composites normalized to the largest response for each device. At least one of the five chosen films responds to each analyte over the entire range of solvents from isooctane (δ=15.6) to water (δ=48). Using the VERI method of pattern recognition, the responses are plotted on the surface of a unit sphere. Fig. 2 contains the normalized and equalized **[4]** responses of three films to several pure solvents and binary mixtures of these solvents and water vapor. Each point is a different set of concentrations (water, solvent vapor). Using just three polymer composite films, several different solvent vapors and binary mixtures with water vapor can be distinguished visually. The sensor responses to an unknown vapor are compared

0-9640024-2-6/hh1998/$20©1998TRF
DOI 10.31438/trf.hh1998A.22

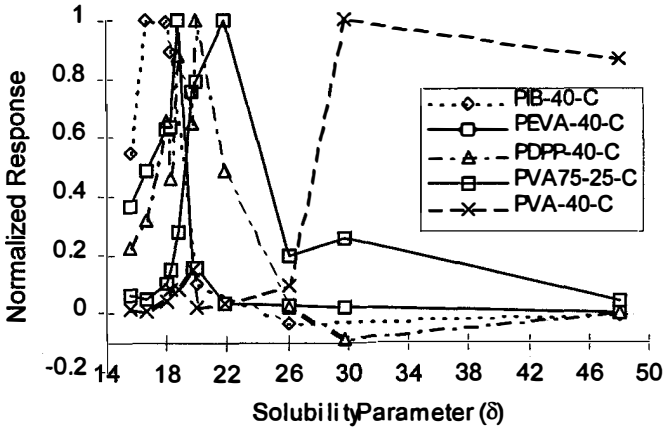

Fig. 1 Normalized response of carbon-loaded polymer films to 11 solvents spanning the range of solubility parameters from isooctane to water. The solvent vapor for each exposure was at 23°C and P/P_{sat} = 0.10.

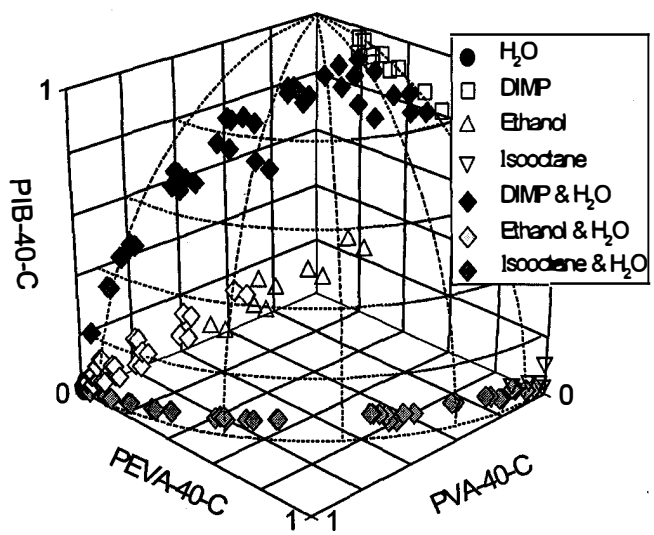

Fig. 2 Pattern recognition for distinguishing classes of solvents. Using three polymer composite films, several different solvent vapors can be distinguished visually. The sensors and vapors were at 23°C.

with patterns, such as in Fig. 2, and once classification is achieved the concentrations of the water vapor and solvent can be determined from the training set data.

An example of such a binary training set is shown in Fig. 3 where the PVA-40-C and PEVA-40-C sensor data for a DIMP (diisopropylmethylphosphonate)/water vapor binary mixture are plotted. In this case, the DIMP concentration was varied with constant relative humidity in the background gas stream. Any new data point, representing an unknown mixture, will be surrounded by four points in the training set and the concentrations of both species can be estimated by interpolation. For a real sensor array, more data could be collected to fill in the gaps in the data set, and to determine the error or confidence level in each value.

The curvature of the isochemical lines in Fig. 3 shows that the responses of binaries are not simply superpositions of the response of the individual concentrations. The curvature means that the presence of one analyte can have a measurable effect on the sensor's response to the other analyte.

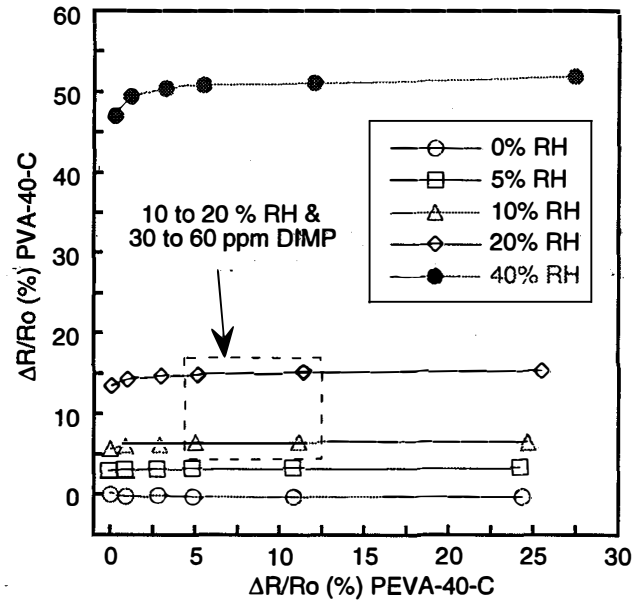

Fig. 3 The relative response of two sensors to binary mixtures of water and DIMP vapors. Water concentration is given as % relative humidity (RH). The DIMP concentration (P/P_{sat} = 0, 1, 3, 5, 10, 20%) was varied with constant relative humidity in the background gas stream. P/P_{sat} for 100% DIMP at 23°C, the temperature of the bubblers and sensors, is equal to 600 ppm.

CONCLUSIONS

Several carbon-loaded polymer films have been used as solvent sensors in an array. The array is capable of responding to a wide range of solvent vapors with widely varying solubility parameters. A method for the classification and quantification of binary mixtures of solvents is presented. This method relies on training data sets, which map out the regions of interest for water-solvent vapor pairs. This simplified version of the VERI method can be applied to any system of sensors, as well as for more than three sensor responses.

REFERENCES

1. R. C. Hughes, M. P. Eastman, W. G. Yelton, A. J. Ricco, S. V. Patel, and M. W. Jenkins, "Application of the Solubility Parameter Concept to the Design of Chemiresistor Arrays", *Technical Digest of the 1998 Solid-State Sensor and Actuator Workshop*, Hilton Head Isl., SC, 6/7-11/98.

2. M. C. Lonergan, E. J. Severin, B. J. Doleman, S. A. Beaber, R. H. Grubbs, and N. S. Lewis, "Array-Based Vapor Sensing Using Chemically Sensitive, Carbon Black-Polymer Resistors", *Chem. Mater.*, *8*, 2298 (1996).

3. R. A. McGill, M. H. Abraham, and J. W. Grate, "Choosing Polymer Coatings for Chemical Sensors", *Chemtech*, *24*, 27 (1994).

4. G. C. Osbourn, J. W. Bartholemew, A. J. Ricco and G. C. Frye, "VERI Pattern Recognition Applied to Chemical Microsensor Array Selection and Chemical Analysis", *Accts. Chem. Res.*, *31*, xxxx (1998).

Ackler, H. 37
Adrian, R.J. 29
Aksyuk, V. 11
Allen, M.G. 19
Allen, P.B. 5
Aluru, N.R. 3
Ayon, A.A. 25
Beebe, D.J. 29
Bishop, D.J. 11
Bodenhöfer, K. 41
Boyd, J. 33
Casalnuovo, S.A. 43
Chang, S.-P. 19
Chen, D.-Z. 25
Chung, C. 11
Cowen, A. 27
Crary, S.B. 1
Culbertson, C.T. 35
Dhuler, V. 27
Doering, R.W. 31
Doerr, C. 11
Edwards, R.L. 17
Fan, L. 7
Ford, J.E. 11, 13
Ghodssi, R. 25
Goossen, K.W. 13
Göpel, W. 41
Hesketh, P.J. 33
Hierleman, A. 41
Hill, E. 27
Howard, J.T. 5
Hughes, R.C. 43
Ilic, B. 33
Jacobson, S.C. 35
Jenkins, M.W. 43
Kolesar, E.S. 5
Krulevitch, P. 37
Lau, K.Y. 9
Lee, J.-B. 19
Lin, C.-C. 25
Mahadevan, R. 27
Mamin, H.J. 23
Meinhart, C.D. 29
Muller, R.S. 9
Nee, J.T. 9
Nguyen, C. T.-C. 15
Nguyen, N.T. 31
Noworolski, J.M. 21
Pang, S.W. 15
Patel, S.V. 43
Phan, K.N. 1
Ramsey, J.M. 35
Ricco, A.J. 39, 41, 43
Ried, R.P. 23
Rugar, D. 23
Sanders, S.R. 21
Santiago, J.G. 29
Schmidt, M.A. 25
Sharpe, W.N. 17
Stanczyk, T. 33
Staton, A.W. 39
Su, G.D. 7
Swierkowski, S. 37
Turner, K. 17
Vykoukal, J. 37
Walker, J.A. 11, 13
Walters, M. 27
Wang, X. 37
Weigold, J.W. 15
Wereley, S.T. 29
White, R.M. 31
Wilken, J.M. 5
Wong, A.-C. 15
Wood, R. 27
Wu, M.C. 7
Yelton, W.G. 39, 43